TEM of Biologically Induced Reactions: Kidney Stone Mineralization and E. coli-Fiber Interactions

By
DAVID J. BANNER
B.A., Southern Illinois University at Carbondale, 2013

THESIS

Submitted as a partial fulfillment of the requirements
for the degree of Doctor of Philosophy in Bioengineering
in the Graduate College of the
University of Illinois at Chicago, 2020

Chicago, Illinois

Defense Committee:

Tolou Shokuhfar, Department of Bioengineering, Chair and Advisor
Constantine Megaridis, Department of Mechanical and Industrial Engineering
Reza Shahbazian Yassar, Department of Mechanical and Industrial Engineering
Michael Stroscio, Department of Bioengineering
Michael J. Young, Department of Medicine

This dissertation is dedicated to my loved ones

ACKNOWLEDGEMENTS

It is with sincere gratitude that I thank and acknowledge everyone who helped me throughout my PhD studies and production of this dissertation. I thank my advisor Prof. Tolou Shokuhfar, and my co-advisors, Prof. Constantine Megaridis and Prof. Reza Shahbazian Yassar. I also thank my thesis committee, Prof. Michael Stroscio, Dr. Michael J. Young, Prof. Constantine Megardis, Prof. Reza Shahbazian Yassar, chaired by Prof. Tolou Shokuhfar. I also extend my thanks and gratitude to our collaborators, Prof. Peter Kral and Pavel Rehak, for their assistance in modeling our experimental results, in preparation of our manuscript, and for the insight their work provided.

I also thank my lab mates from In Situ Nanomedicine Laboratory: Dr. Surya Narayanan, Jodi K. Osborn, Justas Jacobunis, Dr. Emre Firlar, Dr. Seyed Mohammadreza Ghodsi, Abhijit Phakatkar, Sai Bhosle, Laura Alzate, Nasim Farajpour, Shayan Shafiee, Dr. Kun He, Dr. Yifei Yuan, Dr. Seyyad Soroosh Sharifi, Tara Foroozan, Md Rasul Golam, Zhennan Huang, Boao Song, Ram Deivanayagam, and Ramin Rojaee. You have given me feedback, taught me many techniques, and helped me with experiments as my coauthors.

I would also like to acknowledge Dr. Alan Nicolls, Fengyan Shu, Olivia Thompson, and Figen Seiler from the electron microscopy service at UIC for providing technical expertise and resources needed to complete this dissertation. This dissertation would not have been possible without your training, mentorship, and continued assistance.

This work made use of the EPIC Facility of Northwestern University's NUANCE Center, which has received support from the Soft and Hybrid Nanotechnology Experimental (SYyNE Resource) (NSF ECCS-1542205); the MRSEC program (NSF DMR-1720139), the International Institute of

Technology (IIN); the Keck Foundation, and the State of Illinois, through IIN. This work made use of instruments in the Electron Microscopy Service of the Research Resources Center at UIC. This work was funded by the National Science Foundation (DMR-17100139) and the Nonwovens Institute grant 16-195.

DJB

AUTHOR CONTRIBUTIONS

David J. Banner wrote the manuscripts from Chapter 1 through Chapter 3. Tolou Shokuhfar, Constantine Megaridis, and Reza Shahbazian Yassar edited and contributed to the manuscripts. Tolou Shokuhfar is the primary advisor of these works.

David J. Banner and Pavel Rehak prepared the manuscript in Chapter 4. Tolou Shokuhfar, Reza Shahbazian Yassar, and Petr Kral edited and contributed to the manuscript. Tolou Shokuhfar is the primary advisor of this work

David J. Banner wrote Chapter 5 and Chapter 6 with editing by Prof. Reza Shahbazian Yassar, Constantine Megaridis, and Tolou Shokuhfar. Tolou Shokuhfar is the primary advisor of this work.

David J. Banner prepared figures 1.1-1.13, 2.1-2.3, 3.1-3.3. 3.5-3.8, 4.2, 4.3, 4.5, 6.1-6.3, B1-B4, D1-D5. Shayan Shafiee prepared figure 1.4. Shayan Shafiee and David J. Banner prepared figure 3.4 and 4.1. David J. Banner and Pavel Rehak prepared figure 4.4. Pavel Rehak prepared figures D6-D7. Talia Tasheen assisted with data processing and preparation of figures 4.2 and 4.3.

David J. Banner collected data for figures 2.1, 2.2, 3.1-3.3, 3.5-3.7, 4.4 a-j, 4.5 a-f, h, i, B1-B4, D3-D5. Emre Firlar collected data for figures 4.2, 4.3, 4.5 h and j, and D1-D2. Pavel Rehak collected data for figures 4.4 k-n, and D6-D7. Tara Foroozon collected data for figure 4.5 g. David J. Banner prepared most of the samples. Justas Jakubonis, Agata Bogdanowicz, and Yusuf Baggia assisted with bacterial culturing. Jodi Finlay repeated *ex situ* calcium oxalate experiments and data analysis.

TABLE OF CONTENTS

TABLE OF CONTENTS (continued)

LIST OF TABLES

LIST OF FIGURES

LIST OF FIGURES (continued)

LIST OF ABBREVIATIONS

ACC	Amorphous calcium carbonate
ACO	Amorphous calcium oxalate
AFM	Atomic force microscopy
AgNPs	Silver nanoparticles
AuNPs	Gold nanoparticles
BSE	Backscattered electron
CaOx	Calcium oxalate
COD	Calcium oxalate dihydrate
COM	Calcium oxalate monohydrate
COT	Calcium oxalate trihydrate
COS7	African Green Monkey kidney fibroblast cells
COVID 19	Coronavirus disease 2019
CVD	Chemical vapor deposition
DLPs	Double layered virus particles
DLPC	1,2-dilauryl-phosphotidylcholine
dsDNA	Double stranded DNA
E	Envelope protein
EELS	Electron energy loss spectroscopu
EDS	Energy dispersive x-ray spectroscopy
EGF	Epidermal growth factor
FSE	Forward scattered electron
GFP	Green fluorescent protein

GLC	Graphene liquid cell
GSCs	Glioblastoma stem cells
HEKs	Human embryonic kidney cells
HHF	Human heart ferritin
HHS	Human spleen ferritin
IE	Incident electron
IPTG	Isopropyl β-D-1-thiogalactopyranoside
LB	Lysogeny broth
LC-TEM	Liquid cell transmission electron microscopy
M	Membrane Protein
MD	Molecular dynamics
MIC	Mean inhibitory concentration
MPs	Microparticles
N	Nucleoprotein
NaOx	Sodium oxalate
NLPs	Nanolipoproteins
PBS	Phsophate buffered saline
PEG	Polyethylene glycol
PFG	Protein functionalized graphene
PLGA	Poly(lactic-co-glycolic acid)
PME	Particle-mesh Ewald method
PVP	Polyvinylpyridine
QDs	Quantum dots

ROS	Reactive oxygen species
S	Glycoprotein spikes
SAED	Select area electron diffraction
SE	Secondary electron
SEM	Scanning electron microscopy
ssDNA	Single stranded DNA
STEM	Scanning transmission electron microscopy
TE	Transmitted electron
TEM	Transmission electron microscopy
TNTs	Tunneling nanotubes
UA	Uranyl acetate
XRD	X-ray diffraction

SUMMARY

Conventional transmission electron microscopy (TEM) of biological samples depended on preservation of the sample *via* glutaraldehyde fixation or cryogenic freezing of the samples. Recent developments in TEM techniques have enabled the nanoscale observation of biological samples in their native states. Further, it is now possible to observe real-time, nanoscale behavior of biological and biomaterial species. Here, liquid TEM provides fundamental mechanistic insight into prevention of kidney stones by: 1) prevention of bacterial infections by understanding the mechanism of rough nanotextures with antibacterial properties, and 2) understanding the crystallization pathways and inhibition of calcium oxalate (CaOx), the primary component of the majority of kidney stones.

The antibacterial properties of rough surface topologies were first observed in nature. Cicada and dragonfly wings have rough surface topologies which prevent bacterial binding and kills bacteria[1–4]. The industrial implementation of antibacterial surface topologies offers unique advantages as compared to conventional antibiotics or chemical treatments. In contrast to other approaches such as penicillin, bleach, or alternative treatments such as silver, antibacterial nanopatterns do not require the introduction of any toxic material. The nanopatterns are instead formed on a biocompatible surface, such as a suture[5]. Mathematical modeling provided additional insight into the mechanism by which the rough surface topologies kill bacteria[3,6]. However, the inability to observe nanoscale interactions without liquid TEM prevented direct insight into the antibacterial mechanism[3,6].

Here, liquid TEM in combination with conventional TEM and benchtop antibacterial testing provides direct evidence that nanoscale surface topology kills *E. coli via* a penetrative mechanism. Rough surface topologies are plasma etched onto poly(lactic-co-glycolic acid) (PLGA) microparticles (MPs). The nanopatterned PLGA MPs were compared with smooth, unetched PLGA MPs, amorphous PLGA, as well as with silver nanoparticle positive controls. Benchtop testing showed that only rough PLGA MPs kill bacteria. Smooth PLGA MPs and etched amorphous PLGA indicate that the amorphous etched PLGA do not kill bacteria. Conventional TEM shows a nanopillar within dead bacteria and does not observe stretching of the bacteria between multiple nanopillars as previously predicted[3,6]. Liquid TEM shows that nanopillars penetrate the bacteria and initially damage the cell wall at the site of the nanopillar. This suggests that the *E. coli* was directly killed by the localized deformation, breakage of the membrane, and leakage of the cytosol, rather than by apoptosis or through stretching of the membrane.

In addition to liquid TEM of antibacterial surface topologies, here the crystallization of calcium oxalate (CaOx) is observed *via* liquid TEM and molecular dynamics (MD). CaOx is a biologically synthesized material essential to plant life[7]. However, CaOx forms kidney stones in humans[7]. Here, CaOx is formed *via* chemical synthesis to study the fundamental behavior of the biomaterial. Liquid TEM combined with conventional TEM and benchtop studies show that CaOx forms CaOx monohydrate (COM) *via* both classical nucleation and by multiphase nonclassical nucleation. The classical nucleation pathway forms rhombohedral COM, while the multiphase non-classical pathway forms square COM. Citrate, a kidney stone inhibitor, plays a dual role by 1) preventing the nucleation of CaOx at low concentrations by forming soluble calcium:citrate ion interactions,

and 2) increasing the local water molecule concentration. At high concentrations of CaOx, the increases the hydration state and forms polycrystalline COD.

CHAPTER 1: INTRODUCTION TO LIQUID ELECTRON MICROSCOPY TECHNIQUES AND APPLICATIONS

1.1 Conventional, Cryogenic, and Liquid Transmission Electron Microscopy

Many events necessary to human, animal, and plant life occur at the nanoscale[7,8]. Changes as small as the misfolding of a single nanoscale protein may produce the untreatable and fatal Huntington's disease[8]. Further, the nanoscale crystallization of calcium oxalate produces structural changes essential in plant life, but may produce kidney stones in humans[7]. Conventional and cryo transmission electron microscopy (TEM) were essential in determining the nanoscale structure of many nanoscale biological samples[9,10]. However, conventional and cryo EM require fixation of biological or other wet materials[9,10]. In conventional TEM of biological materials the sample is preserved in a resin, typically glutaraldehyde, and microtomed to create a thin cross-sectional image. Cryo TEM flash freezes the sample instead of preserving it in resin. However, it still provides a static cross-sectional image of a preserved sample. The dynamic interaction of nanoscales species that are essential to biological organisms, or that produce medical disorders, may at best be inferred rather than observed in conventional or cryo EM.

These limitations have recently been eliminated by the development of liquid cell TEM (LC-TEM) [11–13]. LC-TEM removes the need for preservation of the sample and prevents the introduction of artifacts from the fixation processes used in conventional or cryo TEM[9–13]. More importantly, it is now possible to directly visualize dynamic events between nanoscale species[11–13]. Previous works have shown that the LC-TEM technique is a powerful tool in studying the real-time

dynamics of bacteria, proteins, viruses, eukaryotic cells, nucleic acids, as well as biologically relevant materials such as calcium carbonate and calcium sulfate (fig. 1.1).

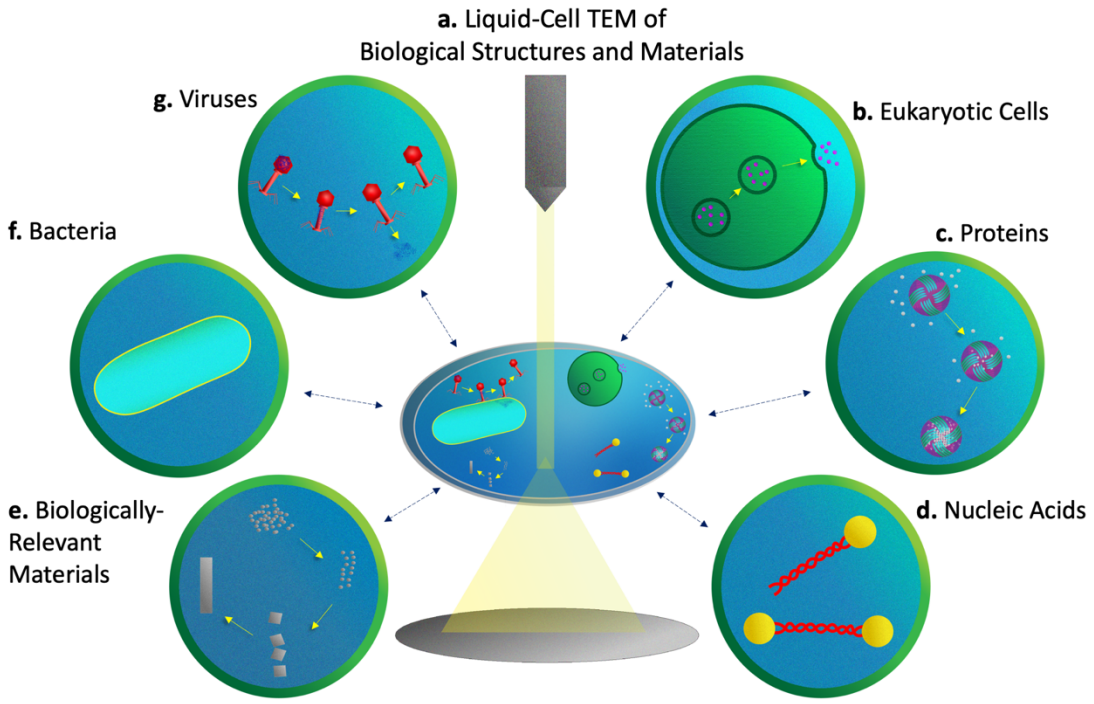

Figure 1.1. Illustrates liquid encapsulation in LC-TEM **(a)**, including eukaryotic cells (**b**), proteins (**c**), nucleic acids (**d**), biologically relevant materials **(e)**, bacteria (**f**), and viruses **(g)**. In **a**, a TEM electron beam gun passes a low-dose beam through a liquid sample. In **b**, a pancreatic beta cell excretes insulin as observed by Firlar et al.[11] In **c**, a protein, ferritin, absorbs iron ions out of the solution as observed by Narayanan et al.[14] This forms an iron core within the protein. In **d**, nucleic acids are labeled with gold nanoparticles to provide insight into nucleic acid dynamics as described by Chen et al[15]. In **e**, calcium sulfate forms via the oriented attachment pathway as observed by He et al.[16] Calcium sulfate first forms nanoparticles, which then form crystals. These crystals then aggregate to form an elongated nanorod. In **f** and **g**, a bacteria **(f)** is infected by a virus **(g)**, as observed by Kennedy et al.[17]

1.2 Static Imaging of Hydrated Biological Samples and Encapsulation in Liquid

TEM of biological samples was pursued almost immediately upon development of the electron microscope, as far back as 1935[18]. Early attempts had extremely poor resolution and offered little benefit as compared to light microscopy[19]. Many of these early studies focused on creating thin polymer windows around a small gas chamber containing a hydrated sample such as bacteria or eukaryotic cells[19]. Once preservation of the sample and sectioning to produce thin samples was developed the encapsulation of biological samples within a gas chamber was largely abandoned for several decades[20]. The preserved samples allowed much higher resolution and offered insights beyond what light microscopy and what early EM of unpreserved samples was capable of[21].

Improvements in mechanical milling and development of more electron transparent polymers over time allowed for vast improvements to encapsulation of a whole sample in its native, hydrated state[11,22–25]. In 2008, Liu et al. achieved encapsulation of eukaryotic and prokaryotic cells *via* encapsulation between silicone oxide (SiO_2) windows[22]. The sample was placed upon a SiO_2 membrane, covered with another SiO_2 membrane, and sealed by epoxy (fig. 1.2)[22]. This method achieved clear definition of the cell wall of biological samples as well as sub-cellular vesicles, demonstrating high resolution imaging[22]. Future researchers improved the design and altered the EM conditions to minimize the electron damage[17,23,24,26–28]. Many modern devices use a similar encapsulation approach but often utilize silicon nitride (SiN) membranes instead of SiO_2[17,23,24,26–28].

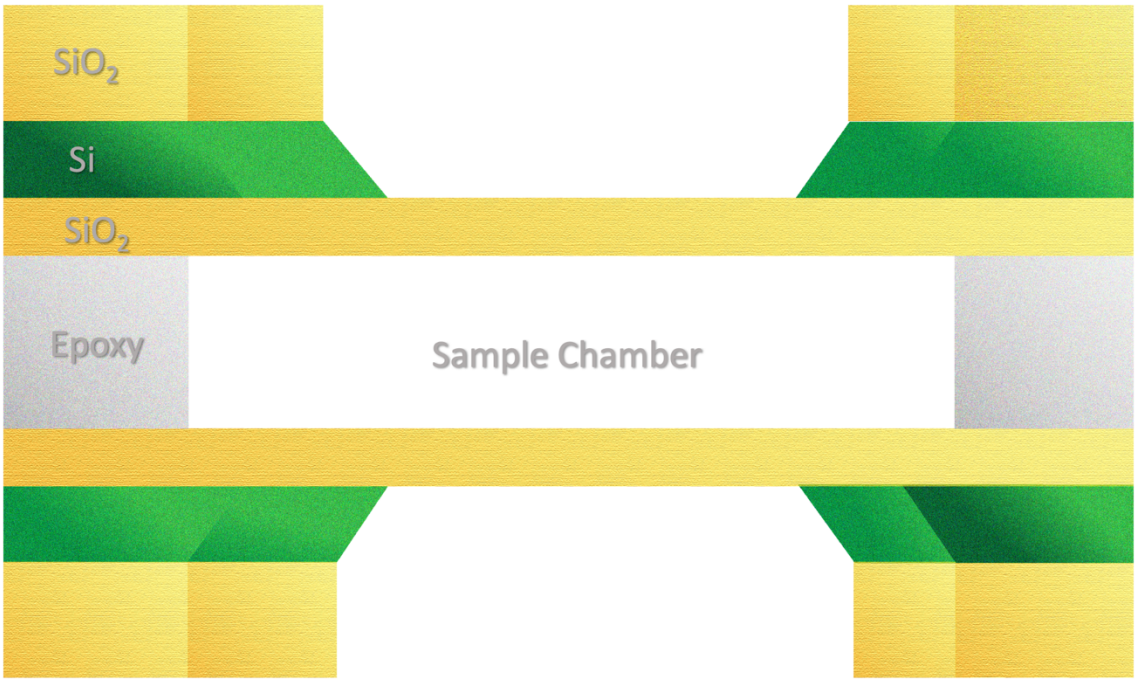

Figure 1.2. An illustration of the SiO_2 encapsulation technique as described by Liu et al.[22] The sample is placed between two SiO_2 membranes and sealed by epoxy.

1.3 Microfluidic Devices

The SiN membrane technique was improved by development of a S/TEM holder with inlet and outlet tubes (fig. 1.3)[23]. This approach is commonly termed LC-TEM. Additional agents may be added to the sample for real time observation of chemical reactions or other interactions[13]. LC-TEM holders may also be used without addition of secondary agents to observe a sample in steady-state and are thus often used instead of the epoxy method described by Liu et al.[22,23]. Another major advantage of LC-TEM is the wide range of chips available. The sample chamber may have as little as 50 nm in distance between the SiN windows or as much as a several micrometers[23].

However, the SiN membrane may stretch within the vacuum, resulting in a greater liquid thickness[29].

The SiN layers that encapsulate the sample are generally on the order of 50 nm in thickness per window[23]. In TEM, this requires the electron beam to travel through one 50 nm thick SiN layer above the sample, through liquid, and then through the 50 nm thick SiN layer below the sample[23]. In STEM, the electron beam travels through the upper window[17]. If the sample is fixed to the upper window, the electron beam may not need to travel through the liquid layer, but must again pass through the upper SiN layer to reach the electron beam detectors[17]. If the sample is not fixed to the upper window, the electron beam is further scattered by the liquid medium[17,23]. The electron beam path through 100 nm of SiN and possibly through several micrometers of liquid significantly lowers the maximum resolution of the images[23]. This decreases the resolution of modern S/TEM from sub-angstrom resolution to several nanometers, depending on the thickness of the liquid layer, the location of the observed sample, and the imaging mode[17,23]. The increased scattering of the electrons within the sample may further increase the electron beam damage and increase production of free radicals within the sample[30]. Yet, the ability to add a secondary agent *via* the inlet or to utilize the large sample chamber available in liquid holders makes this method ideal for researchers in applications where the constraints of the LC-TEM technique are not major obstacles in their application[13]. The increased electron absorption and free radical generation may be alleviated by controlling other parameters, may not significantly affect the sample, or may be utilized by the researchers as a vital part of the experiment[17,24,26–28].

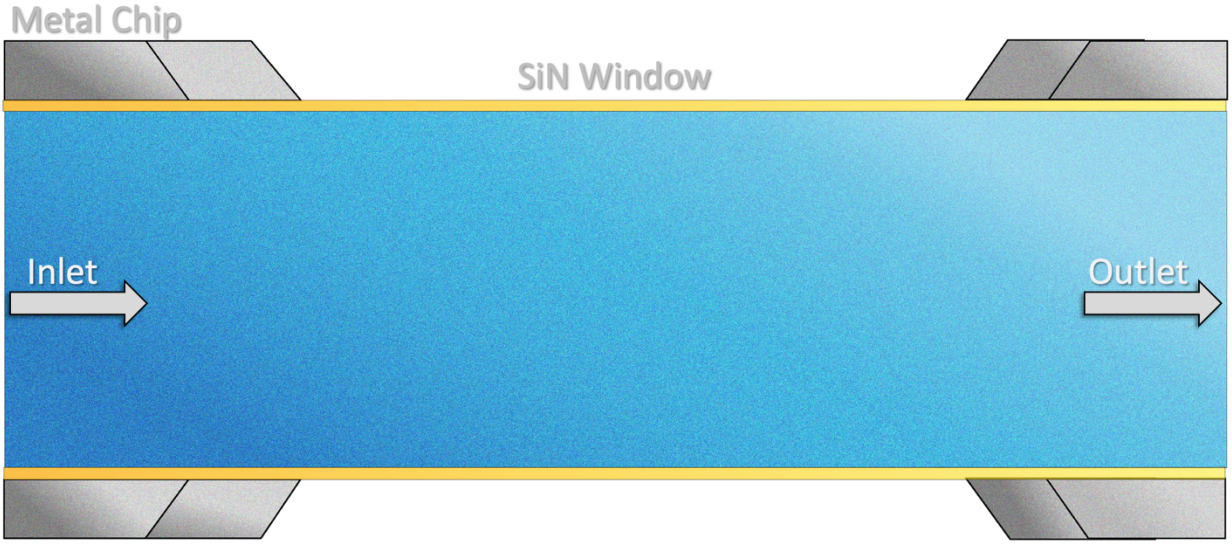

Figure 1.3 An illustration of a LC-TEM chip that allows liquid flow. Metal chips cover thin layers of SiN. Between these layers, liquid flow between the inlet and the outlet as implemented by Woehl et al.[24] among other groups.

1.4 Graphene Liquid Cell

Graphene liquid cell (GLC) S/TEM utilizes a conventional TEM grid sample holder without the need for a specially designed holder[31]. The grid is first coated with graphene, a liquid sample placed upon the grid, and then covered with another layer of graphene (fig. 1.3)[31]. The graphene layers bind together *via* Van der Waals forces, which at the nanoscale are sufficient to adhere the graphene layers even within the vacuum of the electron microscope[32,33]. Several other GLC preparation techniques have been described, but each use the same core concept of creating a graphene bubble containing a liquid sample[34]. Textor et al. provided an excellent review over GLC preparation techniques[34].

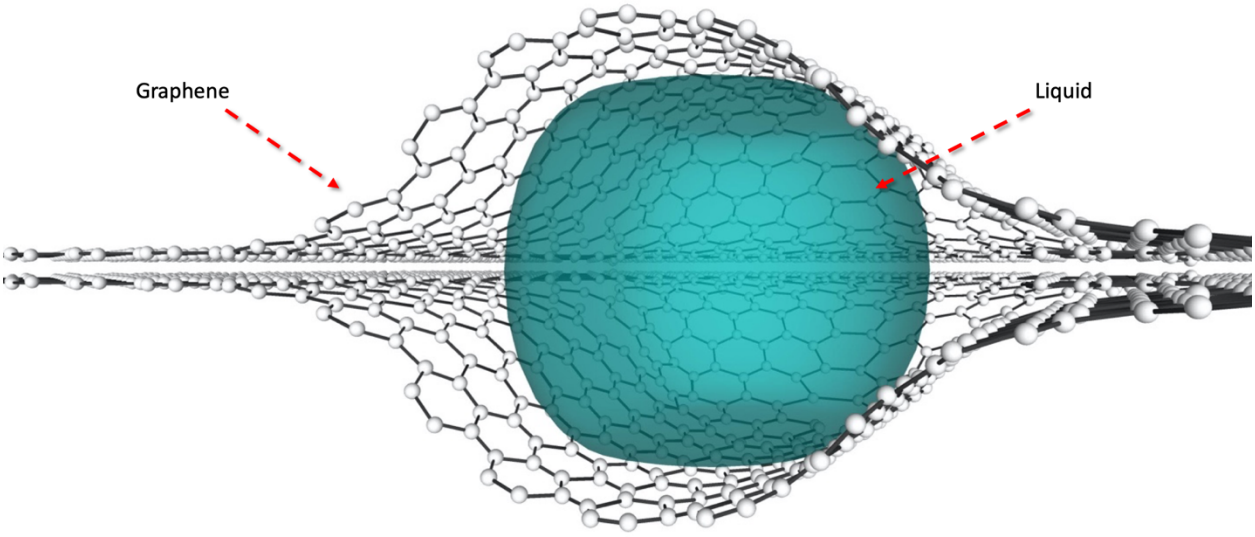

Figure 1.4. An illustration shows a GLC. Small nanoscale or microscale bubbles of liquid (blue) are trapped between two graphene sheets. The single thickness of the graphene allows high-resolution imaging of the sample.

GLC offers a major advantage over SiN: graphene is extremely electron permeable and, ideally, at most several angstroms thick[35,36]. The electron beam then primarily interacts with the liquid layer and the sample, which drastically reduces the electron beam damage due to reduced electron scattering[28]. Since there is less electron beam interaction with the sample the resolution is not lowered as much as is in liquid flow holders[36]. Graphene itself scavenges free radicals, further reducing the influence of the electron beam[37].

GLCs vary in size and may be on the order of several nanometers to several micrometers in diameter[11,32,36]. The nanoscale encapsulation of a sample has created concern over the effect of increased entropy and pressure. These encapsulation effects may indeed be significant for GLC bubbles on the order of several nanometers[32]. However, the change in entropy and pressure decrease exponentially as the GLC bubble approaches hundreds of nanometers to a micrometer[32].

Thus, biological samples such as bacteria or eukaryotic cells, which are on the order of hundreds of nanometers to micrometers in thickness, are not influenced by the encapsulation effects due to the large bubble size required for encapsulation. Further, while some researchers have proposed exposure to the electron beam may raise the temperature of the solution this effect is at most several degrees C[38]. This small increase in temperature is not sufficient to harm the majority of biological samples. If anything, raising the temperature by several degrees C would make the environment more hospitable to the majority of biological organisms[39]. Ghodsi et al. provided a thorough review of GLC S/TEM which discusses these concerns in additional detail[40].

The graphene bubble must be sealed prior to imaging within the electron microscope[34]. This prevents addition of secondary agents during imaging[34]. However, the electron beam may be used to initiate chemical reactions without addition of such materials[28]. GLC bubble size is effectively random[40]. However, as the grids often contain hundreds or thousands of GLCs finding a bubble of ideal size is not often a pragmatic issue[40]. Thus, if a researcher is not significantly concerned about the encapsulation effects, direct control of the sample chamber size, and does not require addition of secondary agents, GLC offers significant increases in resolution and minimizes potentially negative effects of the electron beam[12,36]. In a biological context the encapsulation effects are minimal for large samples such as bacteria or eukaryotic cells, but should be considered in the context of the study[32,33].

1.5 Chemical and Structural Characterization Techniques

The electron beam interacts with the sample to generate both secondary electrons and release x-rays due to the change in energy of the incident electron and the ejected electron[41]. Electron

energy loss spectroscopy (EELS) measures the change in energy of the incident electron as compared to the ejected electron[41]. This energy is specific to both the element and to the ionization state of the element[41]. Energy dispersive x-ray spectroscopy (EDS) measures the energy of the emitted x-rays, and can thus be used to determine the chemical content of the sample[41]. Select area electron diffraction (SAED) may be used to characterize the crystal structure[41]. The electron beam is narrowed to a single point, which is then diffracted by the sample[41]. These techniques have been applied to Fe, Au, and Pd within biological samples and to biologically relevant materials[12,26,36,42].

1.6 Encapsulation and Viability of Bacteria within Liquid EM

In addition to computational models, extensive studies discussed here experimentally verified that bacteria survive electron microscopy under appropriate imaging conditions[17,24,26,27,43]. The viability of bacteria within liquid S/TEM was shown by measurement of the integrity of the cell wall, the integrity of the cytoskeleton, observation of continued protein production, gene expression, and reproduction of bacteria within liquid S/TEM[17,24,26,27,43].

Bacteria were first imaged by encapsulation between SiO_2 windows as described by Liu et al[22]. The authors separately encapsulated the prokaryotic bacteria *Escherichia coli* and *Klebsiella pneumoniae* as well as the eukaryotic yeast *Saccharomyces cerevisiae*[22]. The authors determined the live dead/state of the bacteria by measuring the permeability of the cell wall *via* fluorescent dyes both before and after imaging[22]. A dye that crosses all cell walls is typically used to detect all bacteria, while a second dye that only crosses damage cell walls is used to indicate dead cell bacteria[44]. This assumption is grounded in the reality that if the cell wall is damaged, the bacteria

die[45]. Alternatively, if the bacteria die, the metabolic maintenance of the cell wall ceases and the cell wall degrades[45]. The fraction of live and dead bacteria can then be determined by comparing the number of dead bacteria to the total bacteria. Liu et al. observed that *K. pneumoniae* survived for 14 seconds while *S. cerevisiae* survived for 42 seconds[22]. Huang et al. encapsulated *Deinococcus radiodurans* between SiN membranes, and observed the initial stages of cytokinesis followed by cessation of all motion and bubbling of the liquid[46]. This indicates the bacteria were initially alive but were quickly killed by the electron beam[46]. While these durations were quite short, adjustments to the S/TEM conditions and encapsulation methods in future studies significantly reduced electron beam damage and enabled longer imaging times[24,26,27,43].

In contrast to LC-TEM or GLC, Mohanty et al. implemented a unique method[43]. The authors chemically coated graphene oxide with a protein, caveolin A, to create protein functionalized graphene (PFG)[43]. Next, the authors coated the bacteria with the PFG[43]. The approach sealed the bacteria within graphene which allowed imaging of hydrated bacteria within EM[43]. Mohanty et al. then considered the live/dead state of bacteria by measuring the loss of cytosol as a decrease in cell volume[43]. The key assumption was that the degradation of the cell wall would result in leakage of the cytosol of the bacteria and a reduction of volume[43]. This approach would thus measure the same criteria as defined by conventional fluorescent light microscopy[43]. The authors defined the change in volume (V) as:

Equation 1: $$\mathbf{V} = \frac{\mathbf{V_{B0}+\alpha_1 e^{-\beta t}}}{\mathbf{1+\alpha_2 e^{-\beta t}}}$$

where V_{B0} is the volume fraction of the completely dehydrated bacterium[43]. The constants and α_1, α_2, and β inversely related to the volume[43]. Under low electron doses, the authors observed no change in volume[43]. The bacteria shrank significantly under high electron doses, indicating the electron beam has the potential to kill bacteria if the electron beam is not properly controlled[43]. This suggests that under low electron doses the electron beam and free radicals generated by the electron beam were insufficient to damage the bacteria[28,43]. Mohanty et al. however did not measure additional factors such as protein expression but relied purely on the volume of the bacteria and leakage of cytosol to infer the integrity of the cell wall[43].

The nanoscale nature of bacteria coupled with the low atomic mass of the majority of the elements within bacteria initially presented a pragmatic issue in LC-TEM: The SiN membranes and thick liquid layer obscured the bacteria due to little contrast between the bacteria and the background. This lack of contrast occurs since bacteria primarily consist of low-atomic mass elements, similar to water[24]. Peckys et al. approached this issue by using N-succinimidyl 3-(2-pyridyldithio)-propionate as an intermediate to bind gold nanoparticles to exposed amino acids on the surface of *E. coli*[47]. The *E. coli* were then encapsulated in LC-TEM, and the gold nanoparticles allowed easy identification of the bacteria[47]. Another approach to this issue was explored by Woehl et al.[24]. While many textbooks claim that bacteria do not contain a cytoskeleton, in 1991 Bi et al. showed that some bacteria do contain a rudimentary cytoskeleton[48,49]. One such strain, *Magnetospirillum magneticum* AMB-1 (AMB-1), contains such a cytoskeleton and forms iron nanoparticles along this cytoskeleton[24,50]. The iron nanoparticles produce high contrast within the S/TEM and are easily detectable[24]. Upon cell death, maintenance of the cytoskeleton ceases[51]. This lack of cell maintenance leads to deformation of the cytoskeleton, which may be accelerated by apoptosis and

active breakdown of the cytoskeleton during bacterial death[24,51]. This is reflected by visible disorder of the iron nanoparticles in AMB-1[24]. Woehl et al. used the iron nanoparticles to detect AMB-1 in LC-TEM[24]. This approach was complemented with fluorescent live/dead testing to measure the integrity of the cell wall, similar to Liu et al.[22,24] The authors showed that the cell wall and cytoskeleton of bacteria are intact and that the bacteria are alive according to both the morphology of the cytoskeleton and the conventional standard of cell wall integrity. Wang et al. later encapsulated *E. coli* in LC-TEM, and used the same fluorescent dye approach used by Whoel et al. and Liu et al. to show the live state of *E. coli*[22,24,52]. Wang et al. achieved approximately 10 nm maximum resolution and observed *E. coli* with and without pili[52].

Kennedy et al. utilized a novel approach to increase the resolution of LC-TEM of bacteria[17]. The authors stained *E. coli* with micromolar concentrations of uranyl acetate (UA)[17]. These micromolar concentrations are highly effective in S/TEM due to the high molar mass of UA[17]. While UA is often considered toxic to *E. coli*, the authors showed that in the extremely low concentrations in Kennedy et al. the bacteria were not affected[17]. The authors coated the upper window of the SiN membrane of the LC-TEM holder with poly-L-lysine, an amino acid that caused the bacteria to adhere to the SiN window[17]. This minimized the interaction of the electron beam with the liquid, increased the contrast, and increased the resolution to 5 nm[17]. Thus, Liu et al., Mohanty et al., Woehl et al., Wang et al., and Kennedy et al. confirmed the viability of bacteria within electron microscopy as determined by the structural integrity of the bacteria[17,22,24,43,52]. However, Moser et al.[53] and Moser et al.[54] were unable to image *Cupriavidus metallidurans* in LC-TEM in a live state as defined by observation of structural damage. This bacterial death may

be due to increased electron beam absorbance by the multiple windows of the novel LC-TEM technique in Moser et al.[53] and Moser et al.[54] or due to other confounds[41].

Kennedy et al.[27] further explored the viability of bacteria in LC-TEM in a paper subsequent to Kennedy et al.[17] The authors showed that bacteria were viable as defined by 1) conventional live/dead fluorescent testing, 2) gene expression and continued protein synthesis, 3) observation of cell division and bacterial reproduction, and 4) movement of bacteria under low electron doses that ceased under high electron doses[27]. *E. coli (DH5a)* was genetically engineered with plasmid pFNK-113[27]. These bacteria contain an inducible LuxI-LVA gene, which was co-repressed by a specialized degradable green fluorescent protein (GFP-LVA)[27]. Isopropyl β-D-1-thiogalactopyranoside (IPTG) caused expression of the LuxI-LVA gene, removing the GFP and causing the cell to fluoresce green[27]. Imaging and florescence *via* this gene expression method thus demonstrated that it is possible to image fully viable bacteria within electron microscopy *via* several independently definitive methods and by independent research groups[27]. Thus, bacteria are structurally, metabolically, and reproductively viable under appropriate EM conditions[17,22,24,27,43,52].

1.7 Chemical and Structural Analyses of Bacteria

Firlar et al.[55] and Firlar et al.[26] studied AMB-1, the magentotactic bacteria previously studied by Woehl et al.[24,26,55]. Firlar et al.[55] identified the crystal structure and showed that particles less than 1 nm in diameter were amorphous ferric oxide, particles between 10 nm to 15nm in diameter showed a mixture of amorphous and crystalline phases, before fully crystallizing at diameters greater than 15 nm *via* SAED and EELS in conventional STEM[55]. In a subsequent paper Firlar et

al.[26] encapsulated AMB-1 in GLC. Firlar et al.[26] achieved higher resolution due to the transparency of graphene as compared to the SiN membranes in LC-TEM previously utilized by Woehl et al.[24,26]. Further, the authors observed the real-time formation of iron nanoparticles along the cytoskeleton[26]. The authors used EELS and SAED to show the nanoparticles contained multiple phases, including ferrihydrite, magnetite, maghemite, and/or hematite[26]. Firlar et al.[26] showed that iron converts from magnetite, to maghemite, and then to hematite during mineralization[26]. The authors added live-dead stain to the GLC prior to encapsulation and later observed that the bacteria were alive after TEM *via* fluorescent imaging[26].

The outer metal container of typical LC-TEM holders typically prevents EDS chemical analysis by blocking the x-rays emitted by the sample from interacting with EDS detectors[42]. Lewis et al. however altered the design of an LC-TEM holder to minimize the metal components to achieve EDS of gold nanoparticles, silver nanowires, and carbon nanotubes[42]. In a subsequent publication, Lewis et al. used this novel holder to perform EDS chemical analysis of *Geobacter sulfurreducens*[42]. *G. sulfurredecens* is a proteobacteria that reduces metals to form metallic nanoparticles[42]. *G. sulfurredecens* was cultured in Au and Pd, which allowed the bacteria to form Au, Pd, and AuPd composite nanoparticles[42]. In contrast to AMB-1, which forms iron nanoparticles along a cytoskeleton, the metallic nanoparticles formed on the cell wall of the *G. sulfurredecens*[42]. The authors showed observed the *G. sulfurredecens* contained primarily two types of particles: small, less than 3 nm in diameter nanocrystals and larger Pd coated particles with an Au core[42]. This finding contrasts with previous mathematical models that hypothesized the formation of Au particles with a Pd core[42].

1.8 Tomography of Bacteria

TEM offers a 2D image representing the 3D structure of specimens. This creates some uncertainty as to whether the interactions observed between objects are in fact real or if the objects are at different heights and appear to interact when they are in fact simply above or below each other. Dearnaley et al. implemented a novel imaging technique to address this issue. The authors used half of a SiN liquid flow chip, placed a liquid sample containing the flagellotropic phage (7-7-1) virus and the bacteria *Agrobacterium* sp. H13-3 on it, and then covered the sample with a TEM grid coated in plastic formed from amyl acetate[56]. The authors then tilted the sample between -45° to 45° and collected images at every three to five degrees[56]. The images were then reconstructed to create images with some 3D aspects[56]. However, since the tilt was limited the depth of the images were incomplete, preventing true 3D images[56]. This additional depth confirmed the interaction between the virus flagellotropic phage (7-7-1) and the bacteria *Agrobacterium* sp. H13-3[56].

1.9 Holography of Bacteria

Holography is a technique that allows for the measurement of magnetic fields in TEM. This method measures the interference of a reference electron wave with an electron wave that has passed through the sample[57,58]. Prozorov et al.[57] encapsulated AMB-1 in LC-TEM, the same bacteria studied by Woehl et al.[24], Firlar et al.[55], and Firlar et al.[59] The authors passed the reference wave through the SiN chip and the specimen wave through the SiN chip and the specimen[57]. Prozorov et al. thus mapped the magnetic induction of the iron nanoparticles of AMB-1 and showed a value of $0.58 \pm 0.1\mathrm{T}$ per magnetite nanoparticle with a magnetic saturation of $0.63 \pm 0.1\mathrm{T}$[57].

1.10 Liquid TEM of Proteins

Ferritin is an iron storage protein that is essential for transport of iron and prevention of iron toxicity[60]. Ferritin may contain an iron core[60]. In the absence of an iron core the protein is known as apoferritin[60]. Evans et al. showed that liquid EM has the potential to study proteins such as ferritin *via* LC-TEM[61]. They compared iron-loaded horse spleen ferritin to horse spleen apoferritin, which is ferritin without the iron core[61]. Evans et al. observed high contrast from the iron-loaded ferritin[61]. While apoferritin was visible, there was little contrast[61]. The LC-TEM approach also lowered the resolution, limiting imaging of the approximately 8 nm protein core[61].

Wang et al. characterized horse spleen ferritin *via* GLC[36]. The GLC method significantly increased the resolution of ferritin over LC-TEM. The authors observed that formation of bubbles did not occur at emission conditions less than 6 $e^-/Å^2s$[36]. The lack of bubbles implies minimal generation of free radicals as the bubbles are formed *via* radiolysis of the solvent to form H^+ and O_2 gases[36]. The presence of water and the oxygen contained in the protein shell prevented direct determination of the iron oxides present[36]. The authors measured the energy of the iron atomic L orbitals *via* EELS to determine the Fe^{2+} and Fe^{3+} ratios. In the absence of water, ferritin contained Fe^{3+} [36]. In the presence of water ferritin contained 81% Fe^{2+} and 19% Fe^{3+}[36]. This difference in the oxidation state of iron in dry as compared to hydrated samples indicates the importance of imaging and spectroscopy of samples in their native states as compared to preserved samples[36]. Additionally, Wang et al. imaged ferritin encapsulated between two graphene layers in the absence of water, which allowed atomic resolution imaging and FFT analysis of the crystal structure[36].

Narayanan et al. compared human heart ferritin (HHF) and human spleen ferritin (HSF) *via* the GLC method[12]. The authors observed unique morphologies of the ferritin iron cores[12]. HSF contained spherical, crescent, trigonal pyramidal, and doughnut shapes. In contrast, HHF contained spherical, bow-tie, small spherical, and crescent shaped iron cores[12]. The authors determined the Fe^{2+} and Fe^{3+} ratios *via* EELS, similar to the work by Wang et al. on horse spleen ferritin[12]. Narayanan et al. showed that ferrihydrite was the primary iron oxide present in both HHF and HSF[12]. Both HHF and HSF contained some hematite and magnetite phases[12]. However, the authors also showed that HHF has a higher Fe^{3+}/Fe^{2+} ratio as compared to HSF, suggesting a higher concentration of maghemite in HHF[12]. These results were confirmed *via* SAED[12].

The iron nanoparticles on the AMB-1 bacteria studied by Woehl et al. and Firlar et al. form due to the Mms6 protein, in which the iron mineralizes[62]. Mms6 self-assembles in solution to form micelles that are 25 nm to 150 nm in diameter [62]. Kashyap et al. encapsulated Mms6 in LC-TEM and used the inlet to add iron chloride[62]. The contrast of the micelles increased, indicating uptake of the high-element iron[62]. The outer edges of the Mms6 protein micelles appeared to contain iron nanoparticles, which is consistent with previous studies that proposed iron binds to the C-terminus of Mms6[62]. In the Mms6 micelles the C-terminus is within the protein corona[62]. The authors then added NaOH and observed the removal of iron from the surface of the nanoparticle[62]. Kashyap et al. proposed this mechanism is likely the first step in the demineralization of the Mms6 protein[62].

Nanolipoprotein discs (NLPs) consist of a phospholipidbilayer with an outer protein shell[61]. The interior of the nanodisc may be used to stabilize membrane proteins and may be used to deliver vaccines[61]. Evans et al. imaged NLPs using LC-TEM and observed that the majority of the NLPs stack to form chains, while only 20% of NLPs remained monomers[61].

Lysozymes are antimicrobial proteins that primarily break down the cell wall of bacteria[63]. Yamazaki et al. used LC-TEM to observe that lysozyme crystals formed by first forming an amorphous core, which then induced heterogenous nucleation to form a larger crystal[64]. While Yamazaki et al. observed the formation of both tetragonal and orthorhombic crystals, the tetragonal crystals quickly degraded into amorphous lysozyme particles and dissolved while the orthodromic crystals remained stable[64].

Interferons are signaling proteins that primarily target viruses to stimulate a host response[65]. DiMemmo et al. studied an interferon-based drug, PEGylated Interferon α_{2a} (Pegasys®) in LC-TEM[66]. This drug consists of an interferon protein bound to polyethylene glycol (PEG)[66]. Aggregation of PEGylated Interferon α_{2a} can lead cause reduced drug release and negatively affect the pharmacodynamics. The authors attempted to observe the aggregation of Pegasys® in LC-TEM[66]. The authors incubated Pegasys® with human anti-PEG polyclonal IgG, rabbit anti-PEG monoclonal IgG, and human monoclonal IgM antibodies[66]. The authors further altered the temperature and pH to induce aggregation[66]. DiMemmo et al. observed that acid treated interferon as well as interferon repeatedly thawed and frozen exhibited minor degradation[66]. Interferon heated to 50C for one hour formed large aggregations without any degradation[66]. In the presence of antibodies, there was no significant difference in the Pegasys® samples[66]. The authors further

explored the interaction between the antibodies with biotin bound to PEGylated chains, which did not show aggregations[66].

Kelsin et al. encapsulated microtubules in GLC[67]. These microtubules have uniform crystal structure composed of tubulin dimers, which form a helical structure around a hollow core[68]. The tubulin dimers are composed of alpha and beta tubulin units[68]. Previous works reported that electron doses greater than 10^2 $e^-/Å^2$ damaged microtubules in cryo TEM[69]. Previous works also indicated that the graphene layers in GLC minimizes electron beam scattering and absorbs free radicals[28,37]. The authors thus hypothesized that the graphene component of the GLC would provide a protective effect against the electron damage[67]. Fourier transforms of images collected from microtubules in GLC show spatial frequencies of 0.06 nm^{-1}, 0.10 nm^{-1}, 0.15 nm^{-1}, and 0.20 nm^{-1} [67]. These spacings are reflective of the repetitive structure of microtubules[67]. Kelsin et al. observed that the spatial frequencies, and thus the microtubule structure, stayed intact up to an electron dose of approximately $7.4 \cdot 10^2$ $e^-/Å^2$ [67]. The authors however did not discuss the effect of the electron dose rate

1.11 Liquid TEM of Viruses

Rotavirus is a spherical virus which may consists of two or three layers[70]. The tripled layered virus is pathogenic. The outer layer contains VP4 and VP7 proteins essential for infection[70]. Removal of the outer layer yields non-infectious double layered virus particles (DLPs)[70]. Varano et al. encapsulated DLPs in LC-TEM[71]. The authors bound Ni-NTA and 1,2-dilauryl-phosphotidylcholine (DLPC) to the SiN window, to which they attached His-tagged protein A and IgG antibodies, which targeted the rotavirus DLPs[71]. This adhered the DLPs to the SiN

window[71]. Varano et al. observed viral transcription by DLPs, while in the absence of nucleotides there was no transcription[71]. This result indicates that the DLPs were metabolically active within LC-TEM[71].

Kennedy et al. explored the infection of *E. coli* with a virus, bacteriophage lambda, as discussed in section *3.2*[17]. The authors stained bacteriophage lambda with UA, which provided a significant in increase in the resolution[17]. Bacteriophage lambda attached to the surface of the bacteria, injected the RNA virus into the cytosol of the *E. coli*, and then detached within two seconds[17]. The viral infection process is metabolically mediated which suggests that the virus was functionally intact, the cell wall of the bacterium was intact, and the bacterial proteins necessary for viral infection were functional[17].

Dearnaley et al. studied the infection of *Agrobacterium* sp. H13-3 bacteria by the flagellotropic phage (7-7-1) virus *via* encapsulation in LC-TEM[56]. Flagellotropic phage (7-7-1) consists of a viral head containing viral DNA attached to a tail, which is typically thought to be involved in the attachment of the virus to bacteria[56]. The authors observed that when viruses lost their tails, the DNA was also absent[56]. On the basis of this observation the Dearnaley et al. proposed that the tail may be integral to the preservation of the DNA within the head[56]. The phage was primarily localized to the bacterial flagella which suggested that phage/flagella interactions are instrumental in bacterial infection[56]. In contrast to previous studies, the authors observed that flagellotropic phage (7-7-1) first interacts with the cell wall of the bacteria via the head rather than with the tail[56].

1.12 Liquid TEM of Eukaryotic Cells

The viability of eukaryotic cells in LC-TEM has been debated in SiN flow holder LC-TEM [11,72,73]. Several hypotheses for the death of eukaryotic cells as compared to the live bacteria have been described, including increased electron beam absorbance due to the higher volume of eukaryotic cells as compared to bacteria, the localization of nucleic acids in eukaryotes as opposed to disperse nucleic acid in prokaryotes, or the generally more complex organelles present in eukaryotes[27]. However, the LC-TEM technique does allow the imaging of unpreserved samples with high resolution regardless of the live/dead state. These insights can describe the global morphology of the cells instead of only examining effectively 2D cross-sections. In contrast, Firlar et al. reported eukaryotic cells in a live state in GLC[11]. This may be due to the reduced beam damage and free radical damage in GLC as compared to LC-TEM[11].

Peckys et al. achieved LC-TEM imaging of *Schizosaccharomyces pombe* with a resolution of approximately 32 nm[74]. De Jonge et al. later studied the viability of *S. pombe*, in LC-TEM[72]. De Jonge et al. stained *S. pombe* with FUN-1 live/dead staining[72]. The authors used an electron dose of 0.2 $e^-/°Å$[72]. This was less than the electron dose utilized by Kennedy et al. in their studies of *E. coli*[17]. De Jonge et al. observed shrinkage and breakdown of the plasma membrane[72]. This breakdown resulted in leakage of fluorescent dye and verified the death of *S. pombe*[72].

Epidermal growth factor is a common signaling molecule that binds a tyrosine kinase receptor on cell walls. De Jonge et al. bound epidermal growth factor to 10 nm gold nanoparticles (EGF-Au)[23]. COS7 (African Green Monkey kidney) fibroblast cells were then labeled with the EGF-Au[23]. The high-elemental mass gold nanoparticles provided sharp contrast from the low elemental

mass of the liquid solution and eukaryotic cell[23]. The authors coated the inside of a SiN LC-TEM chip with poly-L-lysine. This poly-L-lysine allowed the COS7 cells to bind to the SiN windows, which minimized electron beam interference from the medium in STEM[23]. The authors obtained a 4 nm spatial resolution and observed circular clusters of EGF receptors as identified by the high-contrast gold[23]. However, this resolution required a high electron dose of 740 e/°Å^2. Peckys et al. used a similar approach by binding 30 nm gold nanoparticles to EGF using N-succinimidyl 3-(2-pyridyldithio) propionate as a linker[47]. The EGF-Au complexes were then bound to the EGF receptors on the COS7 outer membrane[47]. Peckys et al. also coated the inside of a SiN LC-TEM chip with poly-L-lysine to enhance cell binding[47]. The authors achieved a slightly higher resolution of 3 nm [47]. In a subsequent publication, Peckys et al. included unbound gold nanoparticles (AuNPs) in the LC-TEM[73]. The authors observed the vesicular uptake of the AuNPs. Peckys et al. did not observe beam-induced structural damage and reported the viability of the COS7 cells *via* live/dead fluoresce microscopy[73].

Glioblastoma stem cells (GSCs) have increased expression of the protein NOTCH1 receptor[75]. Some next-generation therapeutics thus focus on targeting the NOTCH1 receptor[75]. Previous works showed that nanoparticle-based treatments may be effective against GSCs[75]. Pohlmann et al. explored the interaction between glioblastoma stem cells (GSCs) with polyvinalpyridine-(PVP)-encapsulated gold nanorods[75]. The authors coated a SiN LC-TEM chip with protein A, and then attached NOTCH1 receptor antibodies to the protein A surface[75]. The NOTCH1 receptors then bound to the receptor antibodies and adhered the GSCs to the SiN microwell[75]. Pohlmann et al. observed that the gold nanorods penetrated the cell[75]. The authors also observed significant regression of the cell membrane, which may have occurred due to electron beam

damage or fluid leakage from the SiN chamber as well as cytotoxic substances[75]. Pohlmann et al. used a low incident electron dose of 0.5 $e^-/Å^2$ [75]. However, the SiN chamber contained multiple microwells, which required additional silicone[75]. This may have increased electron scattering.

HER2 receptors are upregulated in both breast cancer and gastric cancer[76]. These HER2 receptors regulate cell signaling including processes which influence cell proliferation[76]. The activation of the HER2 pathway depends on the homodimerization of HER2 subunits, which occurs at the nanoscale. Current fluorescent microscopy techniques can measure the HER2 subunits present, but not the degree of HER2 homodimerization. Peckys et al. reported multiple studies of HER2 receptors *via* LC-TEM.[76] Dahmke et al. examined SKBR3 cells. SNRB3 cells form tunneling nanotubes (TNTs) between cells[76]. These TNTs allow intercellular signaling by allowing movement of small signaling molecules between cells[76]. The formation of TNTs is influenced by HER2 receptors, which are over-expressed in SKBR3 cells[76]. The authors grew SNRB3 cells on SiN microchips, which were then incubated with anti-HER2 Affibodies labeled with quantum dots (QDs)[76]. Dahmke et al. observed increased dimerization of HER2 at the connecting sites of tunneling nanotubes[76].

Peckys et al. compared the effect of trastuzmab, an anti-HER2 antibody cancer therapy, in SKBR3 breast cancer cells to drug resistant HCC1954 cells using LC-TEM[77]. Peckys et al. labeled HER2 receptors with quantum dot bound Affibody peptide and imaged the cells within LC-TEM[9]. The authors observed that trastuzumab cross-linked and decreased the concentration of HER2 homodimers[9]. Peckys et al. did not observe these effects in the drug resistant HCC1954 cells[9].

In a subsequent publication, Peckys et al. examined cancerous HER2 biopsies and HER2 negative control biopsies *via* LC-TEM[78]. The authors labeled the HER2 receptors with the previously described QD dot bound Affibody peptides[78]. Although HER2 dimerization was not immediately apparent from STEM imaging, the authors utilized statistical analysis based on the pair correlation function as previously described by Stoyan et al.[78,79] The results showed increased dimerization of HER2 in cancerous cells[78].

Firlar et al. encapsulated pancreatic beta cells in GLC[11]. The authors first verified the viability of the cells *via* live/dead staining[11]. After 2 hours of GLC TEM imaging the authors observed that 73% of the cells remained viable[11]. Firlar et al. then confirmed the presence of liquid, as well as calcium and zinc, using EELS[11]. Exocytosis may occur *via* four pathways, such as spanning full fusion or kiss-and-run[11]. Alternatively, exocytosis may occur through the sequential or multivesicular pathways[11]. Firlar et al. observed the spanning full fusion pathway, in which an insulin granule fused with the plasma membrane[11]. The authors further observed the sequential pathway, in which a granule fuses with the membrane followed by sequential exocytosis from this location[11]. Additional insulin granules attached to the granules previously bound to the plasma membrane[11]. The granules then exit the cell in a sequential manner[11].

ORAI1 proteins are a type of calcium channel contained in the plasma membrane[80]. Previous optical microscopy suggested that ORAI1 proteins form dimers at rest[81]. In contrast, crystallographic approaches suggested that ORAI1 proteins formed as hexametric channels at rest[82]. Alansary et al. encapsulated human embryonic kidney 293 (HEK) cells in LC-TEM[83].

These HEK cells express few ORAI proteins. The authors deleted the ORAI1 and ORAI3 genes *via* CRISPR/Cas9. These deletions caused a sharp reduction in calcium influx[83].

Alansary et al. used a 9 amino acid HA tag on the extracellular domain of ORAI1 as a labeling site[83]. The authors labeled the ORAI1 with anti-HA Fab antibodies bound to QDs[83]. LC-TEM imaging showed the presence of ORA1 dimers as well as single QSs and larger aggregations of QDs[83]. Alansary et al. analyzed the STEM images *via* the paired correlation function as previously described by Stoyan et al[83]. The statistical analysis did not support the dimer-at-rest model but was consistent with the hexameric morphology previously described by crystallographic studies[83].

1.13 Liquid TEM of Nucleic Acids

Small and low elemental mass species such as nucleic acids may not produce significant contrast in LC-TEM. Chen et al. thus bound to AuNPs to DNA for encapsulation in LC-TEM[15]. The authors examined Au-ssDNA as well as Au-dsDNA-Au[15]. The Au-dsDNA-Au was either short (42 base pairs in length) or long (84 base pairs in length) [15]. Chen et al. identified gold dimers and trimers[15]. The gold dimers consisted of a pair of AuNPs, bound by a strand of dsDNA, while the trimers consisted of three gold nanoparticles connected by two dsDNA strands in series[15]. The authors observed that free AuNPs and dsDNA AuNP dimers both exhibited a diffusivity constant of approximately 1.7 nm^2/s [15].

Keskin et al. encapsulated single stranded DNA (ssDNA) in LC-TEM[84]. The ssDNA was bound to AuNPs of either 17.5 nm (DNA1-AuNPs) or 61.2 nm (DNA2-AuNPs) in diameter[84]. The

authors synthesized a DNA strand (Hyb-DNA) complementary to DNA1 and DNA2[84]. The Hyb-DNA spontaneously binds to DNA1 and DNA2[84]. Keskin et al. then examined four different types of samples in LC-TEM: 1) bare AuNP stabilized with citrate, 2) DNA1-AuNPs and DNA2-AuNPs, 3) DNA1-AuNPs, DNA2-AuNPs, and control DNA, and 4) DNA1-AuNPs, DNA2-AuNPs, and hybrid DNA[84]. Samples 1 through 3 exhibited minimal aggregation due to negative charges on the citrate or on the phosphate DNA backbones[84]. The presence of Hyb-DNA in sample 4 greatly increased the aggregation of DNA-AuNP, thus demonstrating the formation of hybrid DNA in LC-TEM[84]. The authors further observed that the higher electron dose rates increased the diffusion rate of the nanoparticles[84].

1.14 Liquid EM of Biologically Relevant Materials

The morphology and crystal structure of materials may be determined by their nucleation pathway[13,85]. Crystal nucleation may occur at the nanoscale, which necessitates the use of liquid TEM[13,85]. These nucleation pathways may include 1) classical nucleation, in which a central nucleus forms. Ions then bind in series along specific crystal facets. 2), crystallization of amorphous precursors, or 3) aggregation of nanoscale crystals, which then form a larger crystal[13,85].

Calcium carbonate ($CaCO_3$) is a ubiquitous material that composes limestone, chalk, and marble[86]. Eggshells and seashells contain $CaCO_3$[87]. Further, the exoskeletons of many invertebrates contain $CaCO_3$ as part of their exoskeletons[88]. $CaCO_3$ forms different crystal structures with distinct morphologies[13]. Among these are amorphous $CaCO_3$ (ACC), aragonite, vaterite, and calcite. Aragonite exhibits a “sheaf of wheat” morphology, while vaterite exhibits a

spherical morphology, and calcite exhibits a rhombohedral morphology[13]. Nielsen et al. encapsulated $CaCO_3$ in liquid TEM *via* LC-TEM[13]. The authors formed $CaCO_3$ *via* a simple chemical reaction between calcium chloride ($CaCl_2$) and sodium carbonate ($NaHCO_3$):

$$CaCl_2 + NaHCO_3 \rightarrow CaCO_3 + NaCl$$

The authors observed that aragonite formed *via* crystallization of an amorphous precursor[13]. Vaterite also formed *via* initial formation of an amorphous precursor, which then crystallized to form the sheaf of wheat morphology[13]. In contrast, the authors observed that calcite formed *via* two pathways: 1) calcite formed *via* the classical crystallization model, and 2) calcite formed *via* heterogenous nucleation on the surface of previously formed aragonite crystals[13].

Calcium sulfate ($CaSO_4$) is used in a variety of applications, including food preservation, fertilizer, industrial applications such as drywall[89,90]. Further, it is geologically and environmentally present[91]. $CaSO_4$ may be anhydrous, basanite ($CaSO_4 \bullet \frac{1}{2} H_20$), or gypsum ($CaSO_4 \bullet 2H_20$). He et al. encapsulated $CaSO_4$ within LC-TEM[16]. The authors observed that gypsum first formed nanoparticles[16]. These nanoparticles then aggregated, followed by oriented attachment of the aggregated crystals[16]. These aggregated crystals formed gypsum nanoneedles, which then formed single crystalline gypsum microneedles[16]. The gypsum microneedles then formed bulk gypsum[16].

1.15 Control and Minimization of the Electron Beam within Liquid EM

The electron beam experienced by the sample in LC-TEM is reflective of both the incident electron (IE) beam and the stopping power of the sample[28,92]. High energy electrons may pass through the sample as transmitted electrons (TE) inflicting minimal damage[28]. Coulomb interactions may produce elastic scattering, in which the electron trajectory is altered without changing the electron energy or damaging the sample. These electrons may be forward scattered (FSE) or backscattered electrons (BSE). The IE may however knock off secondary electrons (SE) from the sample, producing a change of energy emitted as an x-ray. Sufficiently high electron dose rates may also produce knock-on damage and remove atoms from the sample. However, repeated reflection of SE within the sample may inflict greater damage than the initial high energy electron beam[28]. The electron dose (Ψ) actually experienced by the sample in liquid TEM may be modeled by equation 2:

Equation 2: $$\Psi = \frac{10^5 \mathrm{SI}}{\pi a^2}$$

Where 10^5 is a constant in units of $\frac{\mathrm{m^2\ e^-\ Gy\ g}}{\mathrm{cm^2\ MeV\ C}}$ that converts units SI units to Grays/s, S is the stopping power, I is the electron beam current, and a the radius of the electron beam[28].

The electron beam may also generate free radicals within the sample (e_{aq}^-, OH*, H*, H_3O^+, HO_2*, OH^-, H_2, H_2O_2) [28]. Schneider et al. modeled the free radical generation according to:

Equation 3: $$\frac{\partial C_i}{\partial t} = D_i \Delta^2 C_i - \sum_i k_{ij} C_i C_j + \sum_{j,k \neq i} k_{jk} C_i C_j + R_i,$$

Where k is representative of the reaction rate constants of species i, j, and k. R represents the production of species i due to the electron beam, as described by equation 4[28]:

Equation 4: $$R_i = \frac{\rho \psi G_i}{F} (\frac{M}{S}),$$

Where ρ represents the liquid density, ψ is the stopping power, G_i represents the molecules created by the electron beam as a function of the eV, and F is Faraday's constant. In GLC, graphene mitigates the electron beam damage and absorbs many of the free radicals[37].

1.16 Consideration of Nanoscale Encapsulation Effects

The Van der Waals forces between graphene layers may increase the pressure within GLC[32]. Previous work by Khestanova et al. considered the pressure to be a function of equation 5:

Equation 5: $$P = \frac{4\pi\gamma}{5C_v h_{max}}$$

Where P is the pressure, γ the adhesion strength, C_v is a shape dependent constant, and h_{max} the maximum height[32]. The height may be estimated by equation 6:

Equation 6: $$h_{max}=0.11*R,$$

Where R is the radius[32]. These values suggest pressures on the order of 10 atm to 15 atm for samples on the order of 500 nm to 1 μm[32]. Further, the fixed height to radius ratio suggests that by imaging the 2D radius of the GLCs the height of the sample can be inferred[32].

The confinement of the sample within the nanoscale GLC or LC-TEM also reduces the entropy of the solution[93,94]. This decrease in entropy effectively lowers the effective supersaturation of the solution Kröger et al modeled the change in the saturation of the solution by equation 7:

Equation 7: $$\Omega = \frac{C_i}{C_{eq}} - 1,$$

Where Ω is the relative supersaturation, c_i the concentration of the ionic species and c_{eq} the concentration at equilibrium[95].

1.17 Summary

Chapter 1 provides an introduction into liquid TEM techniques and TEM characterization techniques used throughout this dissertation. Existing studies that utilize the liquid EM technique are reviewed, which indicate that liquid EM can be used to study prokaryotic organisms, proteins, viruses, eukaryotic cells, as well as biomineral crystallization pathways. Significant attention is given to the viability of bacteria within LC-TEM. Further, the encapsulation effects and the electron beam are considered and shown to be minimal if the electron beam dose rate is appropriate. Relevant equations and considerations of decreased pH and increased temperature are also discussed. These equations are revisited in later chapters when experimentally relevant.

CHAPTER 2: PREPERATION OF GRAPHENE LIQUID CELLS FOR LIQUID TEM

2.1 Graphene Synthesis

Here, chemical vapor deposition (CVD) was used to synthesize graphene.. Copper sheets were first cut into 2 cm by 3 cm pieces to fit into the CVD sample chamber. The copper foil is then chemical cleaned. The sample is placed into the CVD sample chamber. The CVD is then brought to vacuum with trace argon, and heated to 1000°C. Trace amounts of methane then flow into the vacuum and are deposited on the copper surface to form a graphene coating. The precise step by step procedure is detailed in Appendix A1.

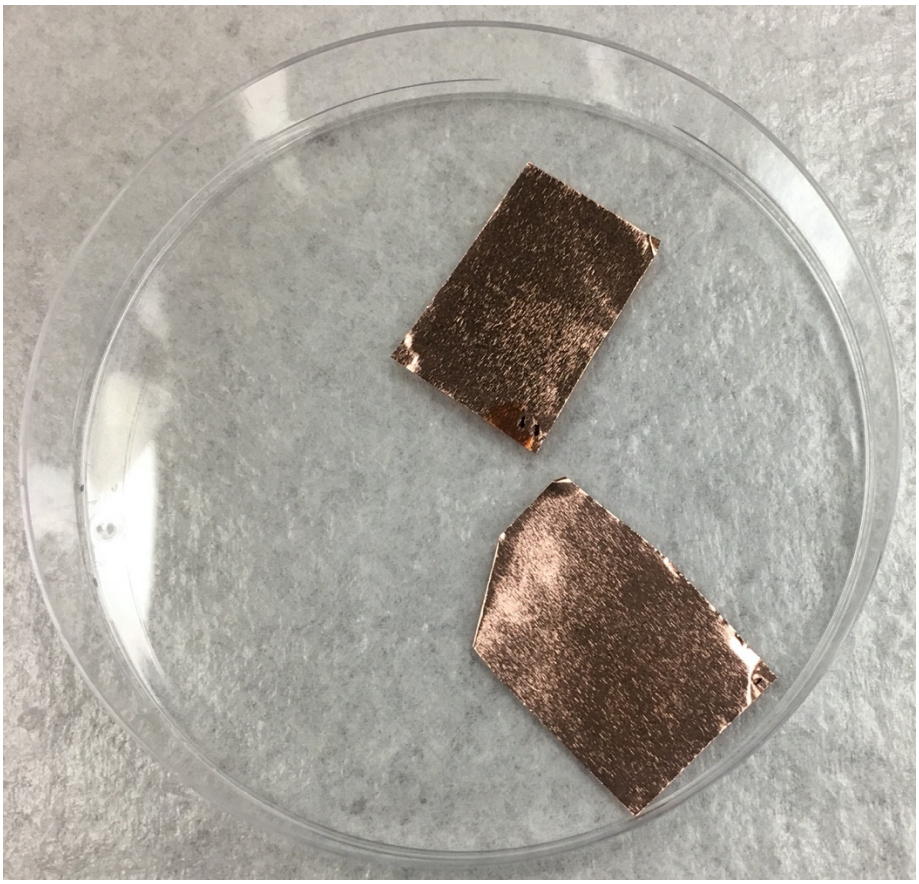

Figure 2.1. Shows copper strips coated with graphene prepared by CVD. The graphene is not directly visible.

2.2 Graphene Coating of TEM Grids

Graphene and graphene coated TEM grids, which hold the sample within the electron microscope, were synthesized in-house. In contrast to other nanoscale samples often used within GLC, the relatively large 500nm to 1000nm in diameter *E. coli* requires relatively large and intact graphene sheets. Smaller samples on the order of 100 nm or less may still be viable with less continuous graphene. To prevent damage and ensure graphene/grid adhesion, a new graphene transfer technique was developed as illustrated in figure 1.2. First, the copper was placed upon a copper etchant surface. The copper was then dissolved leaving the graphene floating on the surface of the etchant solution. The graphene was next lifted out of the solution using a plastic loop. The loop is then touched sequentially to ultrapure water solutions to remove the etchant and any remaining copper. A copper grid is then placed on the surface of the graphene. The graphene grid was then drawn through the other side of the loop by a pair of tweezers, drawing the graphene sheet onto the TEM grid. A drop of IPA was then added to the loop and allowed to evaporate, adhering the graphene to the copper grid. This approach ensures maximal graphene transfer without allowing damage often due to the manipulation of the copper coated with graphene or difficulty adhering the grid to the graphene while it is still on the copper, as are often used in alternative protocols. Here, phase contrast TEM was used to observe the graphene coating of the TEM grid as shown in figure 1.2**f**. This phase contrast technique drastically improves contrast, making the atom layer thick graphene readily visible, but reduces resolution used in conventional TEM imaging. The precise step by step procedure is detailed in Appendix A2.

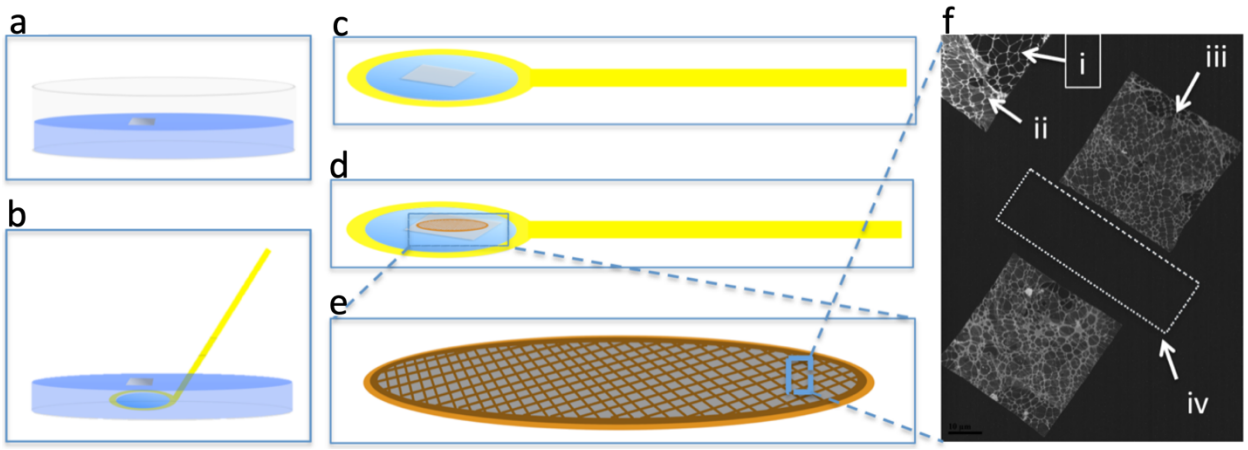

Figure 2.2. TEM grid graphene coating process. The copper is removed from a graphene coated copper sheet by copper etchant, leaching behind graphene floating on the surface of the solution **(a)**. The graphene sheet is removed *via* a plastic loop in **(b)** and **(c)**. The graphene is then cleaned, and a grid placed upon the graphene sheet **(d)**. After adhesion, the grid **(e)** was then imaged in phase-contrast TEM **(f)**. Here, in **(f)**, a lacy carbon coated copper TEM grid coated with the in-house synthesized graphene. The uncoated lacy carbon webbing is indicated as **i**. In **ii**, graphene is indicated by the clear change in contrast. An entire window is coated with graphene is indicated in **iii**, usable for encapsulation of relatively large samples such as bacteria. Finally, the copper grid of the graphene and lacey carbon coated grid is indicated by **iv**.

2.3 Graphene Liquid Cell Assembly

Several GLC assembly methods have been documented[34]. Here, a carbon rod is attached to TEM grid *via* a miniscule amount of glue as shown in figure 2.3 **(a)** and **(b)**. The grid is then inverted, and a miniscule amount of a liquid sample is placed on the grid **(c)**. The volume of liquid is typically reported as approximately 0.5 µL[34]. However, here the smallest amount of liquid possible, on the order of 0.1 µL was used. The small volume allows the GLC to better seal and more fully encapsulate the sample.

Separately, a graphene coated sheet is added to the surface of a copper etchant in a petri dish as shown in figure 2.3 **(d)**. The copper then dissolves, leaving behind a sheet of graphene floating on the etchant surface. The grid containing the sample is then inverted, and lightly touched to the graphene sheet. The carbon rod is then detached. The GLC is then imaged in an EM.

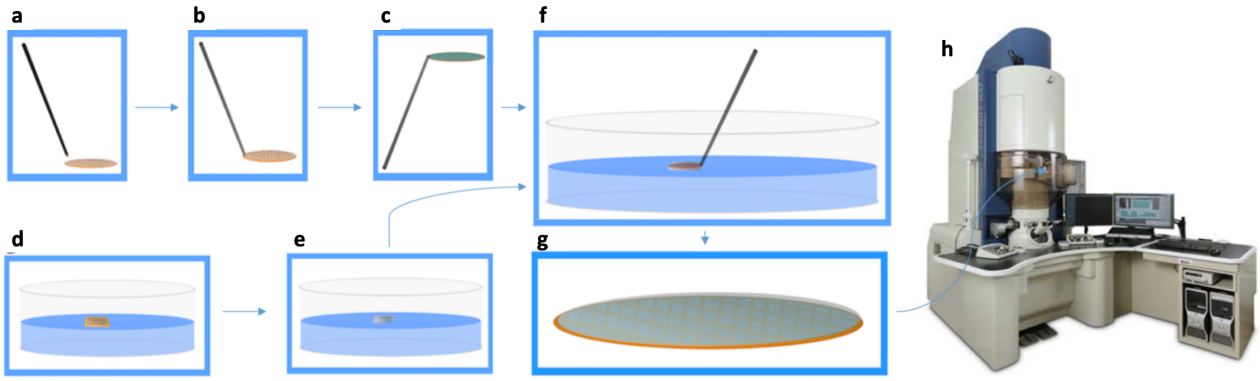

Figure 2.3. Shows graphene liquid cell (GLC) synthesis. In **(a)** and **(b)**, a carbon rod is gently adhered to a copper sample grid. **(c)**, the grid is then inverted and a liquid sample placed on the surface of the grid. Separately, in **(d)** a graphene-coated cooper sheet is placed graphene side up onto a solution of copper etchant. In **(e)**, the copper then dissolves, leaving a graphene layer behind. The TEM grid is then inverted onto the graphene layer **(f)**, forming a graphene encapsulation of a liquid sample **(g)**. The sample is them imaged in a low-voltage electron microscope such as the JEOL 200CF shown in **(h)**.

An alternative method is to hold one graphene coated TEM grid with one pair of inverted tweezers, place a small amount of liquid onto the grid, and then cover the sample with a second graphene-coated grid. The double graphene coated grid sandwich may then be imaged in an EM[34].

2.4 Summary

Chapter 2 describes GLC preparation techniques. Each step is described, including initial graphene synthesis, graphene coating of TEM grids, and assembly of the GLC. Graphene synthesis was achieved *via* chemical vapor deposition. A new method of graphene grid coating was designed and described which achieved greater area coverage that previous approaches. The large coverage areas are essential to encapsulate large samples such as bacteria. Finally, in section 2.3 two GLC assembly approaches are reviewed.

CHAPTER 3: MECHANISTIC INSIGHT INTO ANTIBACTERIAL SURFACE TOPOLOGIES

Portions of this chapter have been reprinted with permission from Banner, D. Firlar, E. Jakobonis, J. Baggia, Y. Finlay, J. Shahbazian-Yassar, R. Megaridis, C. and Shokuhfar, T. Correlative ex situ and Liquid-Cell TEM Observation of Bacterial Cell Membrane Damage Induced by Rough Surface Topology. *Journal of International Medicine.* Originally published by Dove Medical Press Limited.

Portions of this chapter have been reprinted with permission from Banner, DJ, Jakubonis, J. Firlar, E. Final, JK. Bogdanowicz, A. Shahbazian Yassar, R. Megaridis, C. Shokuhfar, T. (2018) In situ Encapsulation of E. coli in GLC and Prediction of Beam Induced Death. *Microscopy and Microanalysis*, 24 (S1). 312-313. Originally published by Cambridge University Press.

3.1 Introduction to Antibacterial Treatments

Antibacterial treatments are implemented in modern medicine, agriculture, and antimicrobial textiles[96,97]. Bacteria are however capable of developing resistance to many antibacterial treatments[98,99]. Conventional antibiotics typically act by preventing upkeep of the cell wall, interfering with the bacterial metabolism, or by inhibiting the synthesis of nucleic acids or proteins[100]. Antibiotics may also depolarize the cell membrane, allowing ion influx[101]. This change in ion concentration can kill bacteria[102]. Antibiotic resistance occurs through limiting uptake of the antibiotic, removal of the antibiotic from within the bacteria, inactivation of the antibiotic through chemical modification or hydrolysis, or modification of the antibiotic's target[103,104]. In gram negative bacteria, the outer plasma membrane provides intrinsic protection against uptake of many antibiotics[105]. Antibiotics primarily depend on the presence of porin

proteins in the plasma membrane[106]. These porin proteins facilitate transport of hydrophilic antibiotics across the cell envelope[106]. Mutations in the porin proteins may prevent transportation of antibiotics[106]. Alternatively, bacteria may reduce the number of porins[106]. In contrast, gram positive bacteria lack the outer plasma membrane and are less likely to limit the uptake of antibiotics[107]. Gram positive bacteria thus depend primarily on inactivation of the antibiotic, modification of the antibiotic's target, or removal of the antibiotic from the bacteria[100].

Three general approaches to battle antibiotic-resistant bacteria exist: 1) continued development of conventional antibiotics, to which bacteria continue to adapt, 2) sterilization techniques using chemical agents, such as bleach, other harsh chemicals, or heating and cleaning of surfaces; such approaches have limited medical applications, require continuous reapplication, and may have detrimental environmental costs. 3) Novel fundamentally different antibacterial treatments that rely on silver or specific surface topologies[108–114]. To this end, bacteria were shown to develop resistance to silver treatments[115,116]. Silver may also present an ecological hazard similar to that posed by chemical or antibiotic treatments[117]. Regardless of whether an antibacterial treatment features an antibiotic drug, strong chemical, or silver, introduction of substances toxic to bacteria may be inherently caustic and induce environmental damage[111,118].

3.2 Introduction to Antibacterial Surface Topologies

Antibacterial surface topologies were first observed in nature. Cicada wings and dragonfly wings exhibit nanotextures which induce bacterial death to reduce bacterial fouling[1–4]. These antibacterial nanotextures may be synthesized on a variety of biodegradable, non-toxic, and non-pathogenic materials without the presence of any bactericidal chemical or elemental agent[5]. In

previous works, Serrano et al explored nanotexturing of biomedical sutures[5], which showed reduced bacterial attachment, suggesting the sutures would be less likely to transmit infections prior to implantation[5]. However, nanostructured cicada wings were previously shown to kill bacteria with a physical mechanism rather than by preventing bacterial adhesion[3].

The bactericidal property of nanopillar surface topologies has been proposed to occur through several mechanisms: Pogodin et al proposed that bacteria bind to the top of nanopillars[3]. The bacteria then attempt to bind below the surface and are consequently stretched between the nanopillars[3]. This stretching of the cell membrane supposedly causes rupture of the cell wall and induces bacterial death[3]. In both gram negative and gram positive bacteria, the cell wall includes a layer of peptidoglycan, which provides mechanical support[119]. In gram positive bacteria, the cell envelope includes the outer cell wall, an intermediate periplasmic space, and an interior plasma membrane[119]. In gram negative bacteria, the cell envelope includes an outer lipopolysaccharide and protein layer, an intermediate periplasmic space, a middle cell wall, a second periplasmic space, and an interior plasma membrane[119]. Linklater el al. proposed another mechanism, in which the bacteria induce mechanical forces on the surface of nanopillars upon binding[6]. These forces then deflect the nanopillars, which then induce strain on the bacteria upon relaxation of the pillars[6]. This strain damages the cell wall and induces the observed cell death[6]. While nanopillar surfaces were experimentally shown to induce bacterial death *via* traditional fluorescent light microscopy and scanning electron microcopy (SEM), the mechanism of bactericidal activity was mathematically inferred in both Linklater et al and Pogodin et al rather than demonstrated experimentally[3,6]. In another mechanism, Michalska et al proposed that black silicon nanopillars

directly penetrate the cell wall of the bacterium.[120] However, Linklater et al later suggested that the bacterial death observed in Michalska et al occurred *via* the strain mechanism.[6,120]

Additional studies have focused on mathematical modeling of bacteria/nanotexture interaction[121–123]. By necessity, these mathematical models included assumptions such that the stiffness of the bacteria may be modeled as a single-layer of peptidoglycan, that deformation of the bacterial cell wall does not induce other metabolic processes (e.g. apoptosis) through programmed cell death, and that the bacteria binding to the material occurs through purely physics-based methods, such as hydrophobic interactions and Van der Waals forces. The initial bacteria/surface contact is indeed dependent on physical factors, such as surface charge and wettability (hydrophilicity/hydrophobicity)[124–128]. However, bacteria/surface binding occurs in a second stage, wherein adhesion forces far exceed the forces in the initial contact period and are dominated by multiple adhesion proteins and attachment pili[124–128]. Bacterial binding of nanotextures is an active process and depends on the metabolic rate, which confirms the active role of protein adhesion in bacteria/nanotexture binding[129]. Thus, while mathematical models are insightful and may prove useful for offering predictions, experimental verification of these mathematical models is also essential. Further, multiple bactericidal mechanisms are possible and may not be mutually exclusive.

3.3 Encapsulation of *E. coli* in Graphene Liquid Cell: Background and Motivation

E. coli were encapsulated within GLC to observe the effect of the GLC encapsulation and electron beam exposure on the bacteria. Safe electron dose rates were determined by observations in the morphology of the bacteria in response to increasing electron dose rates. As in both live/dead

testing and ex situ TEM studies, the integrity of the cell wall was measured to determine the live/dead state of the bacterium. In live *E. coli*, the cell wall is maintained in a smooth, consistent fashion by intracellular processes. Upon bacterial death, the cell wall degrades and thus indicates the death of the bacterium. Alternativity, damage to the cell wall itself kills the bacteria, but in each case cell wall damage is indicative of bacterial death and is directly measured. In conventional live/dead fluorescent testing, this cell wall damage allows internalization of the red dye, which causes the dye to fluoresce and become visible. Intact cell walls, however, prevent internalization of the red dye and prevent fluoresce. Unlike the relatively low-resolution light microscopy, which has a theoretical resolution limit of 200 nm under the most ideal and technically impractical conditions, these nanoscale changes in the cell wall morphology are easily visible in both *ex situ* and *in situ* electron microscopy,

3.4 Encapsulation of *E. coli* in Graphene Liquid Cell: Materials and Methods

3.4.1 Bacterial Culturing

E. coli K12 were commercially purchased (*Escherichia coli* (Migula) Castellani and Chalmers, ATCC® 29425™). Starter cultures were preserved in 50% glyceraldehyde and 50% phosphate buffered saline (PBS) and frozen at -80°C as previously described[130]. Glyceraldehyde and PBS solutions were autoclaved for 30 minutes at 250°C to sterilize the solution prior to innocluation with *E. coli*. *E. coli* was cultured in 50ml lysogeny broth (LB) broth at 37.5°C on an orbital shaker at 100RPM as previously described[131]. The precise step by step procedures are detailed in Appendix B1 and B2. The morphology and live/dead ratio of the bacteria was determined *via* fluorescent live/dead testing as detailed in Appendix B3.

3.4.2 Encapsulation in Graphene Liquid Cell and In Situ Imaging

The LB broth was then removed from the *E. coli* culture *via* centrifugation. The *E. coli* was rehydrated in PBS. Approximately 0.1 µl of the suspension was placed on a graphene-coated TEM grid and then covered with another graphene-coated grid to produce a graphene sandwich, as detailed in section 2.4. The incident electron dose varied between 3×10^{9} Gy/s to 6×10^{10} Gy/s throughout the experiment. A JEOL 1220 TEM was used for image collection.

3.5 Encapsulation of *E. coli* in Graphene Liquid Cell: Results and Discussion

Upon imaging, the *E. coli* bacteria exhibited smooth, undamaged walls, indicating the bacteria was undamaged and alive (fig. 3.1**a**). To determine the effect of the electron beam, the apertures were then removed to allow a high electron dose rate. Removal of the aperture showed immediate changes as the bacteria cell wall became irregular and the volume decreased due to the loss of cytosol (the fluid within the cell) through the damaged cell wall. In figure 3.1 **(b)**, an image after 5 minutes of electron beam exposure is shown. The bacterium is smaller and the cell wall irregular, indicating the death of the bacterium as observed in real-time. In figure 3.1 **(c)**, the decrease in volume was modeled by equation 1 (page) as detailed by Mohanty et al[43].

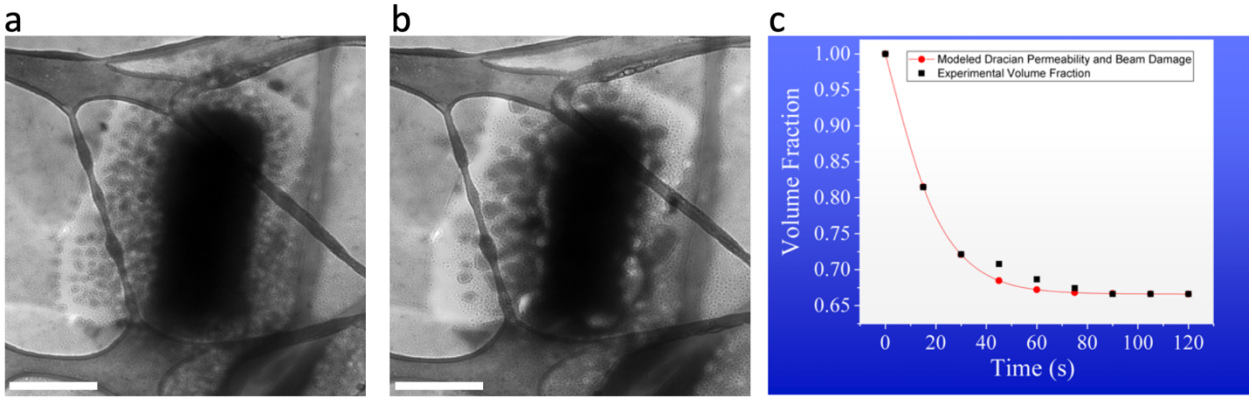

Figure 3.1. *E. coli* is encapsulated in GLC. In **(a)**, the bacterium is imaged at a low electron dose rate. In **(b)**, the bacterium has been exposed to high electron dose rates for ten minutes. The surrounding cell wall became irregular and the volume of the bacterium decreased, both indicating the death of the bacterium. The decrease in cytosol and cell volume is modeled in **(c)**. The majority of beam damage occurred during the first minute of a high electron dose. Reductions in the cell volume and the cell membrane were not witnessed at low dose rates. The scale bars in **(a)** and **(b)** are 500 nm.

3.6 Encapsulation of *E. coli* in Graphene Liquid Cell: Conclusions

Here, *E. coli* was encapsulated in GLC and imaged in TEM. The initial lack of morphological changes and the presence of a smooth, even cell wall indicates that the bacterium survived the GLC encapsulation. Increased electron dose rates however did induce death of the bacterium. *E. coli* die when exposed to a high electron dose on the order of 6×10^{10} Gy/s, while lower values did not kill *E. coli*. Morphological changes during death of the bacterium are directly visible. These morphological changes are essential in the determining the live/dead state of the bacteria.

3.7 TEM Imaging of Silver-Induced Death of *E. coli*: Background and Motivation

Previous works have documented the death of *E. coli* due to the presence of silver ions. Here, silver is used to observe the morphological changes due to bacterial death. The results of this experiment serve as a positive control for future studies which focus on killing bacteria *via* antibacterial surface roughness.

3.8 TEM Imaging of Silver-Induced Death of *E. coli*: Materials and Methods

3.8.1. E. coli culturing

E. coli was cultured in 50ml lysogeny broth (LB) broth at 37.5°C on an orbital shaker at 100RPM as previously described[131]. The precise step by step procedures are detailed in Appendix B1 and B2.

3.8.2 Silver Nanoparticle Solution Preparation

Silver NPs (AgNPs) were commercially purchased and added to sterile PBS. The suspensions were then sonicated to facilitate suspension of the AgNPs and exposed to UV light to sterilize the sample. The precise step-by step procedure is detailed in Appendix B4.

3.8.3 Silver Induced death of *E. coli*

AgNP suspensions were added to the LB broth *E. coli* cultures. The LB broth *E. coli* cultures were then returned to the incubator and cultures for an additional 8 hours. The samples were then removed from the incubator and conventional TEM samples were prepared.

3.8.4 Conventional TEM Imaging of E. coli

E. coli samples were fixed for imaging in conventional TEM. The stationary phase refers to the phase of bacterial population growth at which the total population is constant[132]. Bacteria and the antibacterial agent were centrifuged to isolate the sample as a pellet, with the LB broth removed. The samples were then preserved in resin *via* glutaraldehyde and osmium fixing and staining, as Feng et al previously described .[133] This conventional TEM method includes microtoming the samples to produce cross-sectional 2D slices for imaging[134]. Some of the rod-shaped, bacilli *E. coli* may thus appear circular due to the orientation of these bacteria within the 2D slice[135]. The

precise step-by step procedure is detailed in Appendix B5. A JEOL 1220 TEM was used for image acquisition.

3.8.5 Drop casting for chemical spectroscopy in TEM

LB broth *E. coli* cultured with AgNPs as mentioned in section samples were poured into centrifuge tubes. The centrifuged tubes were centrifuged for 10 minutes at 3000 RPM to form a solid bacterial pellet. The LB broth was then removed from the centrifuge tube *via* pipette without disturbing the bacteria pellet. Sterile PBS was then added to the centrifuge tube. The centrifuge tube was then vortexed to resuspend the pellet. 1 µl of the *E. coli* PBS solution was then placed upon a TEM grid. The sample was then allowed to dry overnight.

3.9 TEM Imaging of Silver-Induced Death of *E. coli*: Results and Discussion

TEM imaging showed dark, high contrast spots indicating the high-contrast silver against the low elemental mass bacterial components. The AgNPs were within the *E. coli*, showing that AgNPs cross the cell membrane. Ruffling and irregular cell envelopes show that the morphology is indicative of bacterial death.

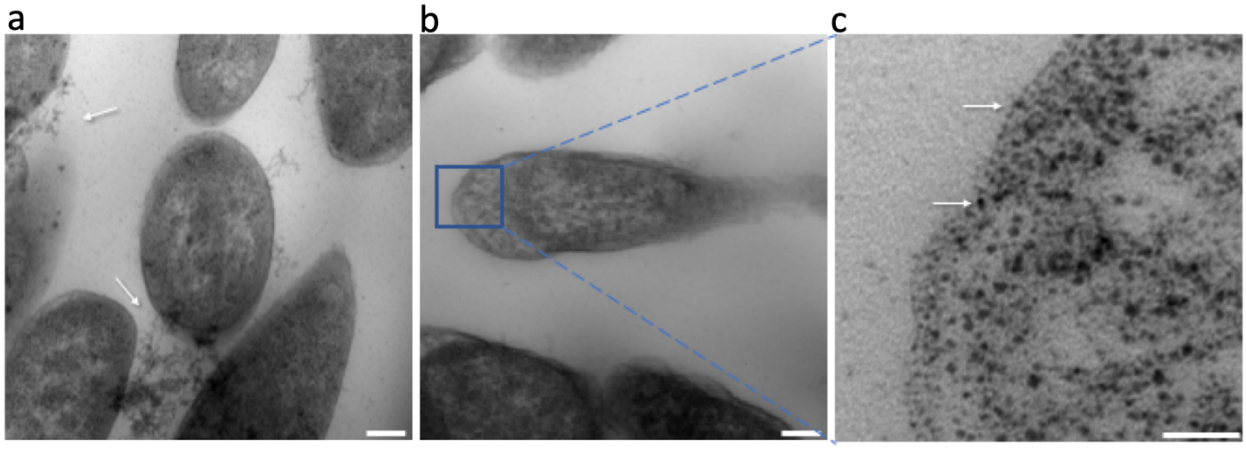

Figure 3.2. TEM imaging of *E. coli* embedded in epoxy resin and microtomed to 100nm thickness.

White arrows in **(a)** and **(c)** indicate the AgNPs. In **(a)**, an image of several *E. coli* shows AgNPs interspersed in the resin near the *E. coli*. In contrast, in **(b)** and **(c)**, AgNP are in the cell wall and cytosol of the bacterium. A higher magnification of image **(b)** is shown in **(c)**. Scale bars are 200nm in **(a)** and **(b)**, and 50nm in **(c)**.

EDS chemical mapping identified the presence of silver within *E. coli.* High contrast particles indicated the presence of the high elemental mass of silver. EDS chemical mapping confirmed the presence of silver within the *E. coli*, confirming that the high contrast images in figure 3.2 are AgNPs

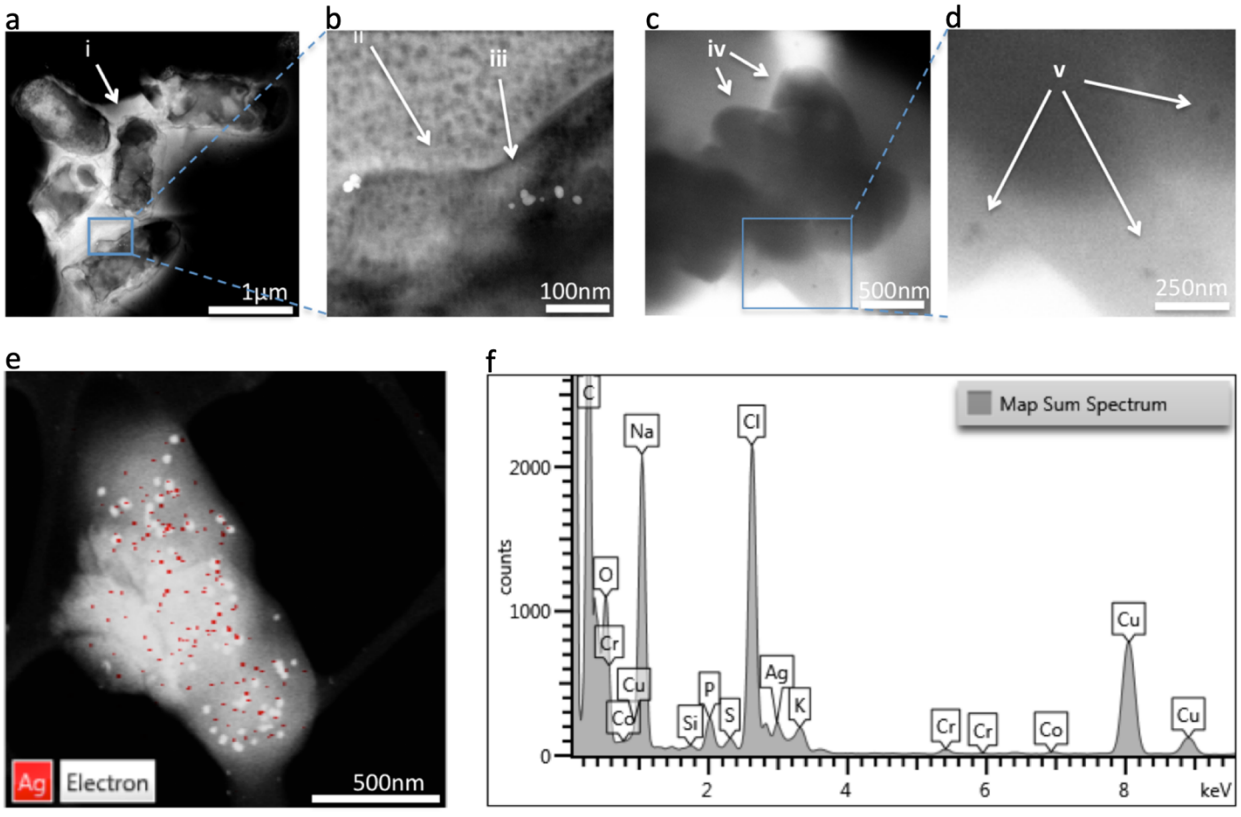

Figure 3.3. STEM imaging and spectroscopy of *E. coli* with silver nanoparticles. In **(a)**, an overview of the damaged bacteria is shown. The damaged and irregular cell is indicated in **(a)** (i) and in **(b)** (ii). In **(b)**, a close up image of the area indicated in **(a)** shows the presence of nanoscale

silver nanoparticles (iii). In **(c)**, *E. coli* are encapsulated with silver nanoparticles in GLC. These bacteria are unstained with uranyl actetate and thus present low contrast. In **(d)**, a close up of the silver nanoparticles. In **(e)**, EDS mapping of an *ex situ* bacterium covered with nanoparticles confirms the particles are silver. In **(f)**, EDS spectra of the mapping shown in **(e)** identifies silver as well as the expected sodium, chloride, phosphorous, and oxygen expected in the bacterium and LB medium. Carbon peaks are from both the bacterium and the carbon coated grid. Other elements such as copper are artifacts of the STEM imaging system. The scale bar in **(a)** is 1 μm, **(b)** is 100 nm, **(c)** 500 nm, **(d)** 250 nm, and **(e)** is 500 nm.

3.10 TEM Imaging of Silver-Induced Death of *E. coli*: Conclusions

Here, TEM confirms previous studies that indicate silver has an antibacterial effect. More importantly, rough cell envelopes provide direct insight into the live/dead state of the bacterium. This damage may occur through 1) production of reactive oxygen species, 2) damage to the cell wall, 3) damage to the nucleic acids or enzymatic proteins[136]. AgNPs may also leech silver ions or induce structural damage[136].

3.11 Correlative *Ex Situ* and GLC TEM Observation of Bacterial Cell Membrane Damage Induced by Rough Surface Topology: Background and Motivation

Observational non-mechanistic studies provide direct evidence of the efficacy of a treatment on a particular bacterial strain. However, bacterial strains vary in size, stiffness, and metabolic processes[137]. Due to these bacterial differences, observational studies require testing antibacterial treatments iteratively against multiple strains to produce a generalized inference of the real-world

applications of any antibacterial approach[120]. Experimental studies of the *E.coli*/nanotexture interaction mechanisms are thus needed to complement existing observational studies and mathematical models. Here, both conventional transmission electron microscopy (TEM) and liquid-phase TEM are implemented to observe the mechanism of bacterial death. Liquid-phase TEM allows for high-resolution nanoscale observations of the *E. coli*/nanotexture interactions without requiring preservation of the sample. *E. coli* K12 is well-characterized in literature as a model organism and was thus chosen for this investigation[138,139]. In contrast to previous works on films or larger fibers, here poly(lactic-co-glycolic acid) (PLGA) microparticles (MPs) are nanotextured and are shown to have an antibacterial effect on *E. coli* in liquid media[3,5,6,120]. PLGA is biocompatible, biodegradable, low-cost, FDA-approved, and may be functionalized with other antibacterial treatments to produce a combined antibacterial effect, if desired[140,141]. Suspensions containing *E. coli* and nanotextured PLGA MPs were imaged in TEM *via* both conventional TEM and liquid-phase TEM *via* graphene liquid cells (GLCs) to observe bacterial death and structural changes in *E. coli* (fig. 3.4). Benchtop antibacterial testing compared the effect of rough PLGA MPs, smooth PLGA MPs, positive controls containing silver, and negative controls without antibacterial agents.

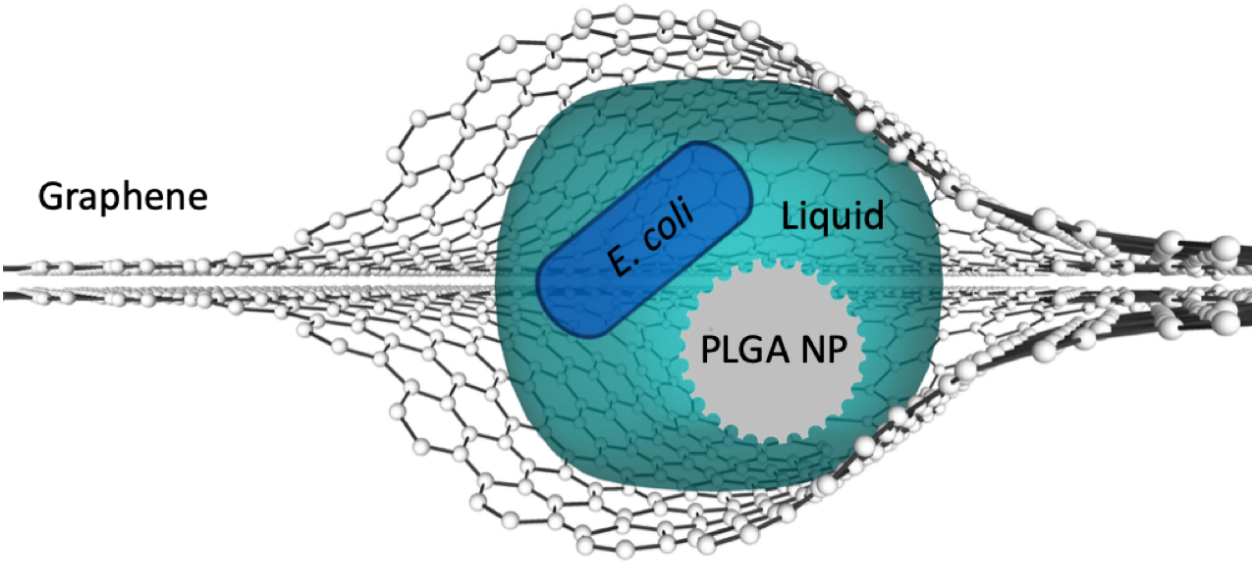

Figure 3.4. Illustration of a GLC containing an *E. coli* bacterium and a PLGA MP. The graphene layers create a liquid sandwich. Full encasement of the liquid sample prevents the escape of all elements.

3.12 Correlative *Ex Situ* and GLC TEM Observation of Bacterial Cell Membrane Damage Induced by Rough Surface Topology: Materials and Methods

3.12.1 Bacterial Culturing

E. coli K12 were commercially purchased (*Escherichia coli* (Migula) Castellani and Chalmers, ATCC® 29425™). Starter cultures were preserved in 50% glyceraldehyde and 50% phosphate buffered saline (PBS) and frozen at -80°C as previously described[130]. Glyceraldehyde and PBS solutions were autoclaved for 30 minutes at 250°C to sterilize the solution prior to inoculation with *E. coli*. *E. coli* was cultured in 50ml lysogeny broth (LB) broth at 37.5°C on an orbital shaker at 100RPM as previously described[131]. The step by step procedure is detailed in Appendix B1 and B2.

3.12.2 PLGA Microparticle Etching

PLGA microparticles (MPs) were commercially purchased (Degrdex® PLGA microspheres, LG500). The particles varied between several nanometers to several micrometers in diameter. The PLGA MPs were then dispersed in DI water and sonicated for 5 minutes. The PLGA MP suspension was then dropcast in 10 µl quantities onto approximately 5x5cm copper sheets and allowed to dry completely for at least 12 hours. The PLGA-covered copper sheets were then plasma etched *via* the method Serrano et al previously documented.[5] The particles were etched using a South Bay PC150 plasma etcher under 200 ppm oxygen at 100 W in 1-minute increments, with 2 minutes between each increment to prevent heating of the sample. After etching, the copper sheets were cut into strips and placed in microcentrifuge tubes containing 1 ml sterile PBS and sonicated for 5 minutes to remove the PLGA MPs from the copper sheets. The step by step procedure is detailed in Appendix B6.

3.12.3 SEM of PLGA MPs

PLGA MPs on copper after plasma etching were gold sputter coated for 1 minute and imaged in SEM *via* a RAITH100 eLine EBL at 2kV to 3kV with working distances of 13 mm to 20 mm.

3.12.4 Silver Nanoparticle Solution Preparation

Silver NPs (AgNPs) were commercially purchased and added to sterile PBS. The suspensions were then sonicated to facilitate suspension of the AgNPs and exposed to UV light to sterilize the sample. The step by step procedure is detailed in Appendix B4.

3.12.5 Colony Counting

E. coli were cultured in LB broth to the stationary phase of *E. coli* growth. 10 µl was then extracted from each *E. coli* culture to determine the viability prior to the addition of antibacterial materials. PLGA MPs and AgNPs were then added to the appropriate *E. coli* samples, which were then immediately returned to the incubator. The extracted samples were diluted to 10^{-2}, 10^{-4}, and 10^{-6}, and plated on LB agar plates as described previously[142]. The colony counting procedure was repeated at 4 hours and 8 hours after addition of the antibacterial or control samples to the *E. coli* culture to observe bacterial death over time. This procedure was repeated six times to produce statistically valid data. The results were analyzed *via* student t-test.[143] The step by step procedures are detailed in Appendices B7 and B8.

3.12.6 Conventional TEM Imaging of *E. coli*

E. coli were cultured to the stationary phase at which point PLGA MPs etched for 2 minutes were added, incubated an additional 20 minutes, and then fixed for imaging in conventional TEM. The stationary phase refers to the phase of bacterial population growth at which the total population is constant[132]. Bacteria and the antibacterial agent were centrifuged to isolate the sample as a pellet, with the LB broth removed. The samples were then preserved in resin *via* glutaraldehyde and osmium fixing and staining, as Feng et al previously described .[133] This conventional TEM method includes microtoming the samples to produce cross-sectional 2D slices for imaging[134]. Some of the rod-shaped, bacilli *E. coli* may thus appear circular due to the orientation of these bacteria within the 2D slice[135]. A JEOL 1220 TEM was used for image acquisition. TEM images were false-colored for clarification. The step by step procedures are detailed in Appendices B5 and B9. The original, unaltered images are included in Appendix B9

3.12.7 In Situ TEM Imaging

E. coli was cultured to stationary phase in LB broth. PLGA MPs etched for 2 minutes were added to the solution and incubated for an additional 20 minutes. The LB broth was then removed *via* centrifugation and the sample rehydrated in PBS. Approximately 1 μl of the solution was placed on a graphene-coated TEM grid and then covered with another graphene-coated grid to produce a graphene sandwich, as detailed in section 2.4. The incident electron dose varied between 3×10^{9} Gy/s to 6×10^{10} Gy/s throughout the experiment. A JEOL 1220 TEM was used for image collection. TEM images were false colorized for clarification. The original, unaltered images are included in Appendix B9.

3.13 Correlative Ex Situ and GLC TEM Observation of Bacterial Cell Membrane Damage Induced by Rough Surface Topology: Results and Discussion

In the first step, the PLGA MP were plasma treated to produce nanotextures on their surface (fig. 3.5**a-c**). The MPs were plasma etched for 1, 2, and 5 minutes to induce different surface roughness. The PLGA MPs were imaged via SEM to observe the surface topology (fig. 3.5**d-g**). The PLGA MPs show minimal nanotexturing in particles etched for 1 minute, while at 2 minutes these nanotextures are deeper and more pronounced. At 5 minutes of plasma etching the sample is highly damaged leaving behind damaged, disordered PLGA. Particles etched for 2 minutes, with the roughest surface morphology, were selected for antibacterial testing.

In the next step, the bacterial activities of treated and untreated PLGA MPs were studied and compared with AgNPs. Unetched smooth PLGA MPs, PLGA MPs etched for 2 minutes, and

PLGA MPs etched for 5 minutes were added in concentrations of 6 μg/ml to separate *E. coli* cultures at the stationary growth phase (fig. 3.5**h**). Additionally, AgNPs, known to have bactericidal effects, were added to separate LB broth solutions in concentrations of 3 μg/ml AgNPs and 100 μg/L NPs to create positive controls[116]. The results show the PLGA MPs etched for 2 minutes lowered the viability of *E. coli* by approximately 64% ($p<0.05$) as compared to controls, while the 100 μg/ml AgNPs exhibited bactericidal effects which lowered the viability of *E. coli* by approximately 57% ($p<0.10$) (fig. 3.5**h**). The *E. coli* sample containing 3 μg/ml AgNP may not have shown a statistically significant antibacterial effect due to the large size of the AgNPs, which may reduce the bactericidal efficiency of AgNPs as compared to smaller AgNPs (fig. 3.5**h**)[144]. The control, smooth PLGA MPs did not kill *E. coli*, in agreement with previous findings that PLGA is non-toxic[140]. The highly damaged amorphous PLGA MPs likewise do not exhibit any bactericidal effect, suggesting that the plasma etching process does not alter the chemistry or surface properties of the PLGA MPs to produce bactericidal effects. Further, the increased surface area on the highly damaged PLGA etched for 5 minutes would be expected to increase the bactericidal effect if bacterial death was due to a chemical effect rather than the rough surface topology. Only the PLGA MaPs etched for 2 minutes with the rough nanotextured surface kill bacteria, to which only the nanotextures are unique, thus indicating that it is the nanotextures that kill *E. coli*.

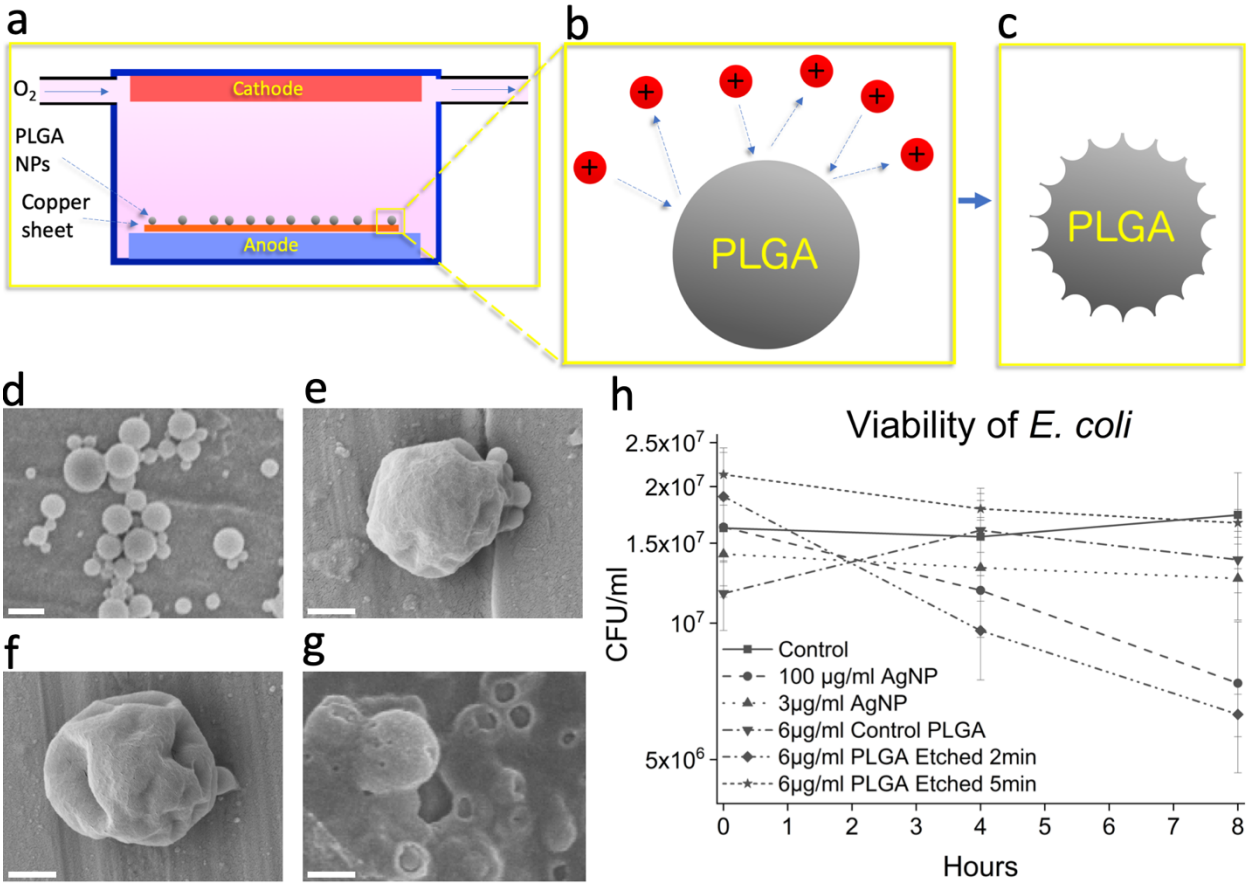

Figure 3.5. Schematic of plasma etching of PLGA MPs (**a-c**), SEM imaging of the control PLGA MPs and the plasma-etched PLGA MPs (**d-g**) and viability graph of *E. coli* control and in the presence of antibacterial agents (**h**). In **a**, oxygen flows in low concentration of (200 ppm) through a charged environment to create free radicals (**b**), which etch the surface, leaving behind rough MPs (**c**). In **(d)**, unetched particles show smooth morphology. In **(e)**, the PLGA MPs show mild dimpling of the surface after 1 minute of plasma etching. In **(f),** the PLGA MPs etched for 2 minutes show more pronounced, sharp patterns as opposed to the PLGA shown in **(d)** and **(e)**. Finally, in **(g)**, 5 minutes of etching severely damaged the MPs, reducing the PLGA to primarily amorphous PLGA aggregations. The bactericidal efficacy of PLGA MPs and AgNPs are compared in **(h)**, where control and bacteria treated with 3 µg/ml AgNPs do not show decreased CFU/ml, while the 100 µg/ml AgNPs samples showed decreased viability. The error bars in **(h)** represent

the standard error. The unetched PLGA does not exhibit a statistically significant bactericidal effect, nor does the PLGA etched for 5 minutes. However, the PLGA etched for 2 minutes, which features rough MP surfaces, does exhibit a statistically significant bactericidal effect. The scale bar is 1 μm in **(d)**, and 500 nm in **(e)**, **(f)**, and **(g).**

Nanotextured PLGA MP/bacteria surface interactions were examined *via* conventional TEM as shown in figure 3.6. In this figure, a PLGA MP has rough nanotexture and uneven edges as observed with SEM (fig. 3.5). As shown in figure 3.5**a-b** (progressive magnification), the MP has a surface protrusion inside an adjacent bacterium. The location of the surface protrusion suggests that the MP pierced the cell envelope of the bacterium, including the outer membrane, peptidoglycan layer, and inner membrane. Piercing the cell envelope would produce local cell damage and lysis of the bacterium[3,6,120,145]. The total absence of the bacterial cell envelope indicates that this damage was sufficient to stop the metabolic maintenance of the cell envelope or produce apoptosis[145]. In contrast to mathematical modeling in previous works, in figure 3.6 the *E. coli* is not stretched between nanopillars but rather is in contact with a single sharp protrusion, which appears to have been directly penetrated the cell surface[3,6,121–123].

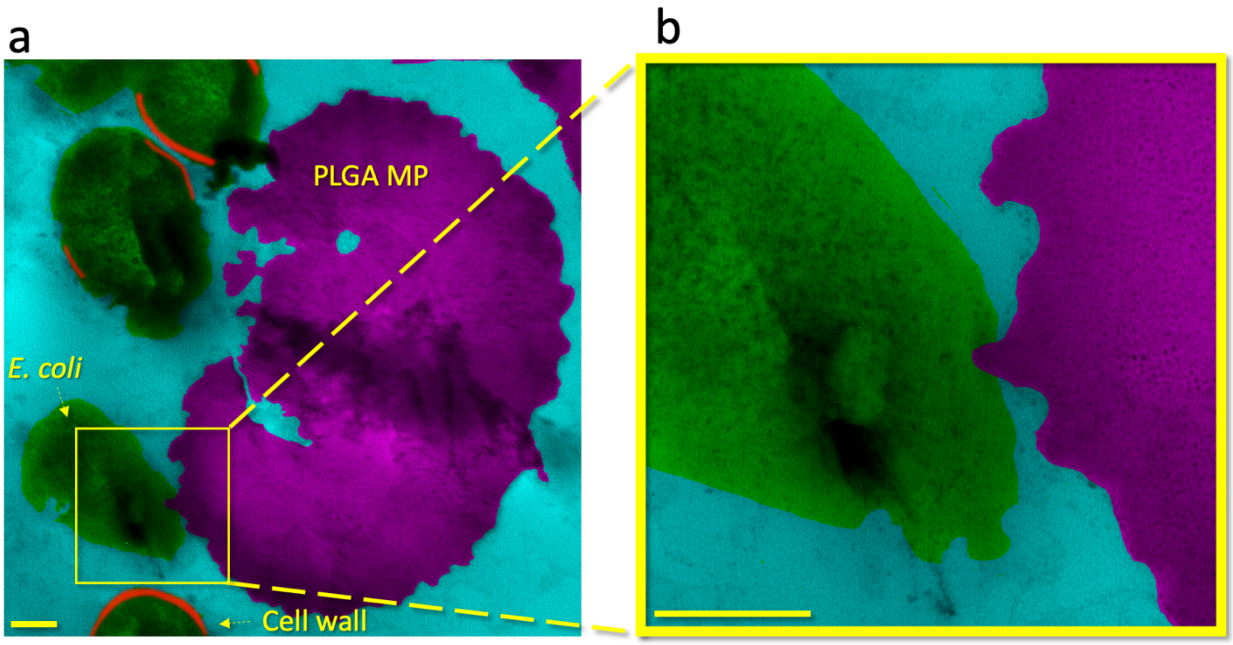

Figure 3.6. Bacterial death is induced by rough MP topography as observed in a cross-sectional image obtained *via* conventional TEM. In **(a)** and **(b)**, low to high magnifications of surface interaction between an *E. coli* and a rough PLGA particle etched for 2 minutes is shown. A sharp peak on the PLGA particle appears to have penetrated the *E. coli* bacterium cell envelope. The area bracketed in **(a)** is shown at higher magnification in **(b)**. The scale bars in **(a)** and **(b)** are 200nm.

E. coli and PLGA MPs etched for two minutes were then encapsulated together in GLCs (fig. 3.7). The GLC images provides further evidence of the penetration of nanoprotrusions in *E.coli*, as also observed forensically with conventional TEM (fig. 3.6). The cell envelope of the bacterium immediately adjacent to a rough PLGA MP is highly damaged and shows escape of the bacterium's cytosol. In contrast, areas distal to the PLGA MP surface protrusion show smooth, undamaged cell envelopes. The localization of cell damage to the site of bacterium/PLGA MP interaction indicates that the bacterium was not killed by general metabolic factors, which would cause diffuse damage

throughout the bacterium cell envelope. Bacterial death thus must have occurred due to the localized damage produced by the *E.coli*/surface interaction.

Gram negative bacteria, including *E. coli*, contain peptidoglycan cell walls approximately 2nm to 8 nm in thickness. In contrast, gram positive bacteria have cell wall thicknesses from approximately 20 nm to 35 nm[137,146]. Peptidoglycan has been considered to provide the structural support and is a primary contributor to the mechanical properties of bacteria[147]. The thickness of the peptidoglycan layer might be intuitively expected to reflect the stiffness of bacteria. In contrast to this expectation, initial experimental studies reported that gram negative bacteria exhibit an average Young's modulus of approximately 30 Mpa while gram positive bacteria exhibit a lower Young's modulus of 20 MPa[137]. However, further studies showed that the Young's modulus varies significantly depending on the bacterial species, growth medium, preparation method, dry or wet state, and measurement method, with previously reported Young's modulus values between 0.05 MPa and 769 MPa[137,148]. This variation in mechanical properties reflects cell wall variations in proteins, phospholipids, teichoic acids, lipoteichoic acids, and differences in peptidoglycan-peptidoglycan binding or interactions[149]. Peptidoglycans consist of alternating sugar moieties, β-(1,4) linked N-acetylglucosamine and N-acetylmuramic acid, which are then attached to a peptide chain[150,151]. While the sugar moieties are highly conserved between bacterial species, the attached peptide chains are bacterial strain-specific and vary significantly in peptide chain length and amino acid composition[137]. Peptidoglycans may be monomers or cross-linked as dimers or trimers, with linkages between a variety of amino acid residues[152,153]. The variation in peptide chains and the activity of crosslinking proteins produces unique chain crosslinking[154,155]. The degree and type of peptidoglycan cross linking is thus highly positively correlated with the stiffness of the

bacteria[149]. Some bacteria may also contain actin-like filaments which form a rudimentary cytoskeleton[50]. These actin-like filaments may influence the mechanical properties of bacteria, including their stiffness[50]. In short, the thickness the peptidoglycan layer and the gram positive/gram negative classification are not sufficient to establish the mechanical properties of bacteria[137]. This suggests that the bactericidal nature of nanoscale surface topologies may also be effective in gram positive bacteria, since the cell wall of such bacteria may be comparable to *E. coli*. [137]

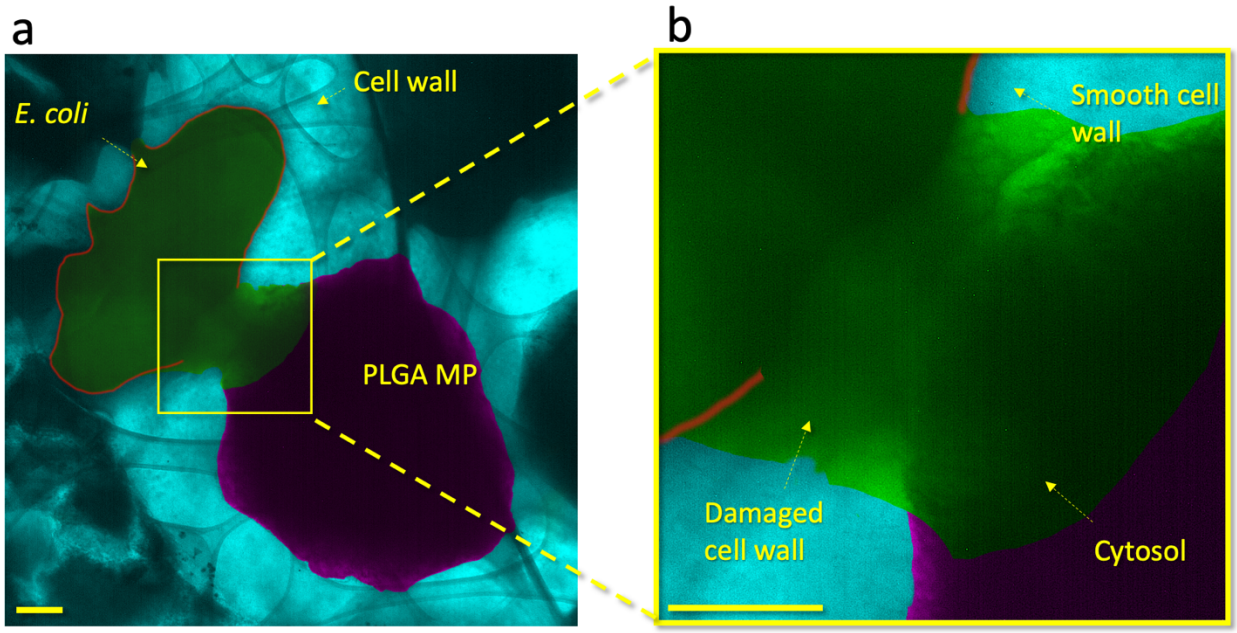

Figure 3.7. GLC encapsulation of *E. coli* and PLGA MPs shows localized damage to the cell envelope of the bacterium. In **(a)**, a lower magnification image shows an overview of the *E. coli* and PLGA MP. In **(b)**, a higher magnification image shows the PLGA MP and bacterium in close proximity. The cell wall proximal to the PLGA MP shows damage with a shape similar to the adjacent MP. A high contrast liquid indicates the cytosol of the bacterium which clearly identifies death of the bacterium. The cytosol has a distinct contrast from the PBS medium due to the

proteins, glycans, and other bacterial components within it. Other areas of the *E. coli* cell wall are smooth and show no damage or degradation. The scale bars in **(a)** and **(b)** are 200 nm.

The deformation of the bacterial cell wall thus depends not on simple physical forces and the thickness of the peptidoglycan layer, but on the Young's modulus of the bacterial cell wall and the attachment forces of the bacterial adhesion proteins. *E. coli* was previously shown to exhibit a Young's modulus of 22 MPa[156]. This suggests the attachment pressure of *E. coli* exceeds this value to produce strain within the cell wall to produce the damage shown in figures 3.6 and 3.7. The bactericidal mechanism of antibacterial nanotextures observed here and supported by literature is illustrated schematically in figure 3.8. First, simple physical forces, e.g. hydrophobic/hydrophilic interactions, bring the *E. coli* into contact with PLGA surface[127,128]. The adhesion proteins then attach and contract to bind the *E. coli* to the PLGA surface[127,128]. However, the protruding fixture on the PLGA surface exerts a local force opposing the adhesion proteins bound to the non-protruding surface (fig. 3.6-3.7). This causes stretching in the *E. coli* cell membrane over the PLGA nanopillar, as experimentally observed here in figures 3.6 and 3.7 and illustrated in figure 3.8**a-d**, which damages the cell envelope. This damage causes death of the *E. coli* and leakage of the cytosol localized to the nanotexture projection as experimentally observed in fig. 3.7. This cell death later results in total degradation of the cell envelope due to reduced metabolic cell envelope maintenance or production of autolysis as experimentally observed in figure 3.6 and illustrated in figure 3.8**e-h**[45]. Here, a mechanism by which nanoscale surface roughness kills *E. coli* K12 has been shown.

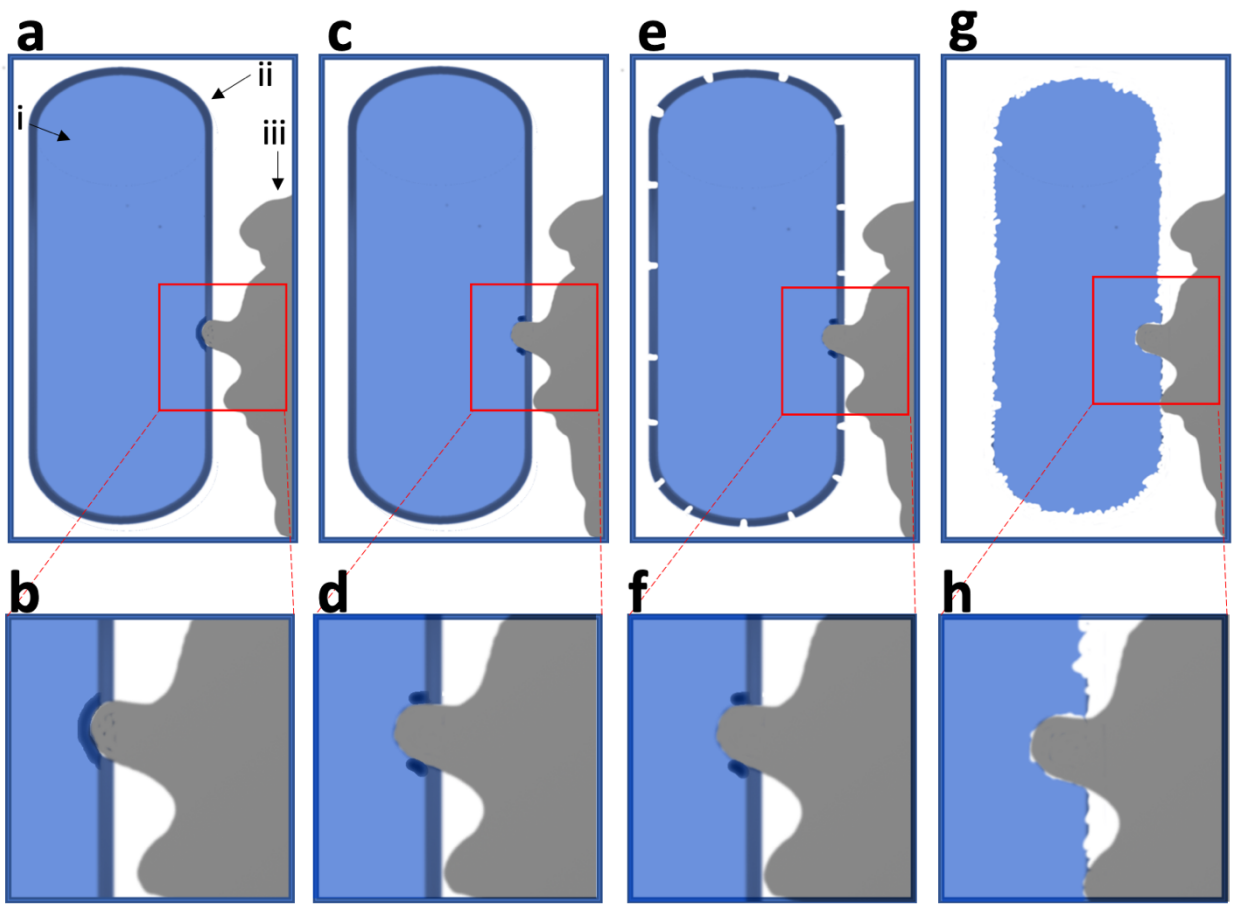

Figure 3.8. Schematic illustration of bacterial death mechanism. The bacterium is shown in blue on the left side of the image **(a) (i)**, whereas the cell envelope is indicated as a dark blue layer on the outer edge of the bacterium **(a) (ii)**. The PLGA particle is shown in grey on the right-hand side **(a) (iii)**. In **(a)** and (**b)**, the particle has come into contact and deforms the cell envelope, before breaking it in **(c)** and **(d)**. This damage then causes degradation of the cell envelope in **(e)** and **(f)**, before the cell wall disintegrates in **(g)** and **(h)**.

3.14 Correlative *Ex Situ* and GLC TEM Observation of Bacterial Cell Membrane Damage Induced by Rough Surface Topology: Conclusions

We report rough nanotextured polymer MPs that exhibit antibacterial action. Such MPs have applications distinct from previously designed media, such as antibacterial gels, liquid

suspensions, or powders. The nanotextured surface topology of the MPs was shown to be bactericidal *via* a localized *E. coli*/surface interaction. The surface protrusions deform bacterial cell walls to induce bacterial death rather than act by damaging bacterial cell walls *via* stretching between nanopillars. This cell-wall damage suggests that the attachment pressure exceeded the force required for deformation of the cell wall of the bacterium. The deformation of the cell envelope appears to cause cell lysis and death of the *E. coli* bacterium. Future studies are required to explore the nanoscale interaction of rough surface topology with other types of bacteria, and to further exploit the antibacterial mechanism shown here.

3.15 Summary

In chapter 3, *E. coli* was first encapsulated in GLC. Experimental studies confirmed that the GLC technique as implemented here did not kill *E. coli* under low electron dose rates. The morphological changes observed in *E. coli* were seen when exposed to the known antibacterial AgNPs and under high electron dose rates. Rough surface topologies were synthesized on PLGA MPs. These rough PLGA MPs were shown to exhibit antibacterial properties *via* benchtop antibacterial testing. Correlative conventional TEM and liquid TEM then revealed the mechanism of the rough surface topology. Rather than the nanopillars stretching the membrane, the bacteria bound to the nanopillars. This binding deformed the cell envelope, which caused localized damage to the cell wall and leakage of the cytosol. Following this antibacterial mechanism, the cell envelope degrades throughout the bacterium, which may occur *via* programmed cell death or through ceased maintenance of the cell envelope.

CHAPTER 4: MECHANISTIC INSIGHT INTO THE CRYSTALLIZATION OF CALCIUM OXALATE

4.1 Introduction to Calcium Oxalate and the Role of Citrate

Calcium oxalate ($CaC_2O_4 \cdot H_2O$, or CaOx) is an important crystal positively affecting plants and fungi and may be involved in environmental CO_2 capture [157–159]. Oxalate sequesters calcium within sub-cellular vacuoles to regulate calcium and in effect stores excess CO_2 in plants, since oxalate is a downstream metabolite of CO_2 [157–159]. This oxalate-mediated calcium storage is essential to ensure adequate calcium is available for critical metabolic processes without causing excess free-calcium toxicity [160–163]. CaOx also provides structural support to plants [160–163]. Bacteria and some fungi are capable of catabolizing oxalate to convert the oxalate to energy *via* metabolic catabolism, such as *via* the glyoxylate pathway [164]. CaOx may be deposited into soil from plants and fungi where it stores ecological calcium [165]. As a biomineral, the presence of oxalates has been hypothesized to be indicative of non-terrestrial life in astrobiology [166–168]. In human and animal life, however, CaOx is pathogenic. CaOx is the major phase in 80% of kidney stones [7,169–171]. Thus, understanding the formation, crystallization, and dissolution of CaOx is essential to the biomedical field, plant biology, soil science, microbiology, and perhaps the search for extraterrestrial life.

CaOx primarily exists as CaOx monohydrate (COM), but may also be CaOx dihydrate (COD), CaOx trihydrate (COT), or rarely amorphous CaOx (ACO), where the thermodynamic stability of COM is the highest and ACO the lowest [172]. COM is the most common CaOx phase in kidney stones, while COD is less common, and COT exceedingly rare [173,174]. Plants primarily contain

COM and COD, which may be specific to the plant species [161]. ACO is highly unstable and quickly crystallizes environmentally but has been observed *via* chemical stabilization of CaOx in the laboratory setting [175–177]. Many studies have focused on characterization of the structure, morphology, and chemical content of CaOx minerals in plants [161], humans [167], and *in vitro* chemical studies [178–180]. Transmission electron microscopy (TEM) studies of CaOx have primarily focused on the *ex situ* interaction of CaOx with biological species or CaOx crystals formed within biological tissues[181,182], such as the interaction between renal epithelial cells and CaOx [183], or on TEM as a characterization technique for benchtop experiments [184,185]. However, few studies documented the real-time CaOx formation.

The importance of understanding the nanoscale nucleation processes of CaOx in real-time is indicated by the dependence of the crystal structure and morphology of other calcium salts on their nanoscale mineralization processes [13]. Previous works showed that the formation pathway of calcium carbonate may determine the morphology of larger, formed calcium carbonate crystals[13]. Molecular modifiers such as citrate were previously thought to increase the solubility of CaOx to prevent the initial nucleation of CaOx [186]. However, citrate may modify CaOx formation by alternative methods such as altering the crystallization and facet-growth of CaOx rather than simply preventing the nucleation of the material [187]. In the Cabrera-Vermilyea (C-V) model, the citrate molecule binds to the surface of a crystal growing *via* edge growth, and inhibits or alters the continued addition of monomers, oligomers, or polymers in the effected plane [188–190]. Alternatively, Chung *et al.* showed that citrate may bind to the surface of the crystal and induce lattice strain, leading to removal of ions and dissolution of the crystal at concentrations otherwise predicted to form CaOx [189]. A well-known phenomenon in other materials, stress of the crystal

by molecular modifiers may directly induce morphological changes [191]. In contrast, Ruiz-Agudo *et al* [184] observed that citrate initially prevented crystallization of amorphous precursors by coating the surface of the precursors to prevent growth, which resulted in formation of COT rather than COM [184].

4.2 Background and Motivation

Considering that the crystallization pathways of CaOx may initiate at the nanoscale, spatially and temporally resolved real-time characterization techniques are required to monitor the transient stages of mineral nucleation and growth. Previously, the *in situ* atomic force microscopy (AFM) technique was used to study the real-time growth of CaOx from seed crystals formed prior to AFM [187,192–196]. While AFM allows analysis of the surface topology of a material, AFM is unable to determine the crystal structure and local chemical changes during growth or nucleation. Here, graphene liquid cell (GLC) within a TEM is utilized to observe CaOx nucleation and mineral growth in real-time. GLC encapsulation of a liquid sample has been previously utilized to achieve nanoscale *in situ* imaging of samples such as colloid nanocrystals, ferritin, or bacteria [12,26,31,40]. In GLC, a liquid solution containing supersaturated calcium and oxalate ($C_2O_4H_2^{2-}$) ions was encapsulated between graphene sheets, thus enabling high resolution imaging of specimens within the high-vacuum chamber of TEM (fig. 4.1) [15,26,31,36,197,198]. The effect of citrate during mineralization of CaOx was then studied in GLC to understand its role in modifying the nucleation and crystal growth of CaOx. Select area electron diffraction (SAED) was used to characterize the crystal structure of the particles formed in the GLC. Molecular dynamics (MD) simulations of CaOx formation in the absence of citrate and CaOx formation in the presence of citrate reveals that as cluster sizes increase, the ratio of water molecules to number of calcium ions in the cluster

reach different limiting values. The end-stage products of the GLC TEM and MD simulations were then validated by *ex situ* benchtop studies. The *ex situ* products were visualized *via* scanning electron microscopy (SEM), structurally analyzed *via* x-ray diffraction (XRD) and were chemically analyzed by electron energy loss spectroscopy (EELS) and energy dispersive x-ray spectroscopy (EDS) within scanning TEM (STEM).

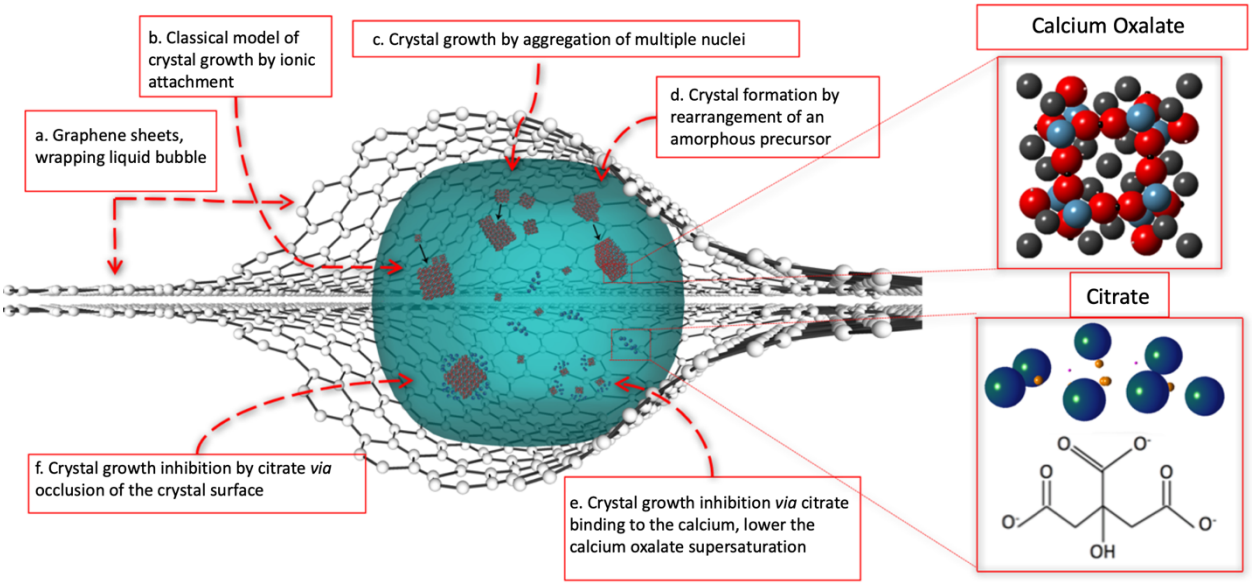

Figure 4.1 Shows multiple pathways by which CaOx could form and multiple mechanisms by which citrate might alter or impede CaOx crystallization. In **(a)**, the graphene layers that encase the CaOx solution are indicated. In **(b)**, CaOx crystallizes via the classical nucleation pathway. In **(c)**, CaOx crystallizes *via* aggregation of multiple crystal nuclei. In **(d)**, CaOx first forms an amorphous particle, which crystallizes upon reaching a density and volume at which the crystalline state is more energetically favorable. In **(e)**, citrate provides alternative calcium:citrate interactions which increases the solubility of CaOx. In **(f)**, citrate binds to the surface of the CaOx crystal. This prevents additional CaOx crystal growth.

4.3 Materials and Methods

4.3.1 Calcium Oxalate Sample Preparation

CaOx was synthesized by a one-step ionic reaction. Sodium oxalate (NaOx) (Sigma-Aldrich) and calcium chloride ($CaCl_2$) (Fisher Chemical) were mixed to form CaOx and NaCl: $Na_2C_2O_4 + CaCl_2 \rightarrow CaC_2O_4 + 2NaCl$. 0.1 M NaOx and 0.1 M $CaCl_2$ were mixed to observe formation of CaOx (Sigma-Aldrich) in picopure water (WaterOmniTrace® Ultra, EMD Millipore Corporation).The initial ionic strength was calculated by equation 8:

Equation 8: $$I = \frac{1}{2}\sum_i z_i^2 C_i,$$

Where *I* is the ionic strength, *z* the charge of the ion, C the molar concentration, and *i* the ions present, assuming complete ionic dissolution [199]. The saturation index was calculated to be 8.5 *via* Visual MINTEQ chemical modeling software. Sodium citrate was added to some solutions to achieve a final concentration of 0.1 M NaOx, 0.1M $CaCl_2$, and 0.1 M sodium citrate concentrations. In *ex situ* samples, CaOx was centrifuged to separate the solid sample from the supernatant which contained NaCl. The supernatant was removed. The CaOx particles were then rehydrated in DI water. This process prevented formation of NaCl during dehydration of the sample for *ex situ* analysis. In *in situ* samples, the CaOx samples were not rinsed since the *in situ* samples remain in liquid which prevented the formation of NaCl. The precise procedure is detailed in Appendix C.

4.3.2 In Situ TEM Imaging

In situ TEM imaging was achieved *via* encapsulation of CaOx samples and samples containing CaOx and citrate in between two layers of graphene. NaOx, $CaCl_2$, and sodium citrate solutions were added to microcentrifuge tubes and then combined as discussed in section 2.1. Approximately 0.5 µl of the solution was added to a graphene coated grid. A second graphene coated grid was placed graphene side down on the liquid sample. Textor et al provided an extensive review of this GLC synthesis process[34]. The grid was then placed into a TEM sample holder. The TEM holder was placed into a vacuum pump to remove any liquid that was not encapsulated in GLC from the TEM holder. The sample was then imaged in TEM at 80kV. The precise procedure is detailed in Appendix A.

The absorbed electron dose rate was calculated by equation 2 as detailed in section 1.7[28]. The absorbed electron dose rate was between $3*10^9$ Gy/s to $2.24*10^{12}$ Gy/s. pH and radiolysis species analyses were based on previous works [28]. Time scales reported in figures 4.2, 4.3, and 4.4 consider the start of the video to be t=0, which occurs after preparing the sample-containing GLC, loading the GLC into the microscope, focusing the microscope, and locating a particle or area of interest. GLC samples containing CaOx or CaOx and citrate were observed *via* a JEOL 1220 TEM (fig. 4.2, 4.3, and 4.4), and *via* a JEOL ARM 200CF scanning TEM (STEM) operated in TEM (figure 4, S6-S8). SAED of GLCs was collected *via* the JEOL ARM 200CF STEM. False-colorized images are included in the published manuscript to better illustrate CaOx formation in GLC. The unaltered images are included Appendix D for further reference.

4.3.3 MD Modeling of Calcium Oxalate Formation

MD simulations were performed with NAMD2.12[200]. Water molecules were described using TIP3P model[201]. Monoatomic ions were modelled using previously determine Lennard-Jones parameters and integral charges[202]. Parameters for citrate and oxalate ions were determined using MP2/6-31G*// MP2/6-31G* level of theory, in implicit water solvent through Gaussian program[203], using VMD force field toolkit[204]. The long-range Coulomb interactions were calculated *via* the particle-mesh Ewald (PME) method in all simulations[205]. Long-range interactions were evaluated every 1 (van der Waals) and 2 (Coulombic) time steps. The NpT ensemble was used to perform simulations at a temperature of 310 K for all simulations, constant pressure (varied for different simulations) and a Langevin constant of γ_{Lang} = 1.00 ps^{-1}. All simulations had the same number of water, calcium, oxalate ions, such that [CaOx]=0.125 M at 1 atm. There were a total of 254 oxalate ions in all simulations. Simulations with citrate ion present had the same number of citrate ions as number of oxalate ions added to the system. Spectator ions were also added into the system in order to replicate experimental conditions. Each system (citrate present or absent) only differed by pressures applied with targets of 1 and 100 atm. Systems were minimized for 5000 steps and then pre-equilibrated for 2.01 ns, with a time step set to 2.0 fs. One carbon atom on each oxalate and citrate (if applicable) molecule was harmonically constrained in order to allow these molecules to rotate, but not diffuse during minimization and pre-equilibration. There were no constraints during the simulations, which ran for 100 ns and with a time step of 1.0 fs.

A cluster was defined whether there was at least 1 calcium ion and at least one oxalate or citrate molecule, which had at least one atom within 2.5Å of that calcium ion. Cluster sizes were

iteratively determined by analyzing a central cluster of oxalate, citrate, or calcium ions and determining whether they different molecules of those same species (neighbors) within 2.5Å of the first central cluster. Iterations ended when no new neighbors were found. After the cluster size was determined, we determined the number of water molecules that were within 2.5Å of any calcium, oxalate, or citrate molecule in the final cluster. In order to eliminate artifacts of having a finite simulation box, we determined whether any molecule in the final cluster was within 4.5Å of the boundary of simulation box. If there was a cluster close to the boundary of the box, we displaced the entire cluster and neighboring water molecules by the dimension of the corresponding boundary, yet opposite in direction. We then repeated the iterations as described earlier. Sizes of clusters were determined by the number of calcium ions in that cluster. Evaluations of cluster sizes were determined for every 1.00 ns, due to memory limitations.

4.3.4 SEM Imaging

CaOx samples formed in the absence of citrate and CaOx samples formed in the presence of citrate were added in 50µl volumes to copper tape upon an SEM stub and air-dried overnight. Samples were gold sputtered for 4 minutes at 20eV. SEM images were collected at 2keV to 3keV at working distances of 13mm to 20mm with a RAITH100 eLine EBL.

4.3.5 X-Ray Diffraction

A Bruker D8 Discover x-ray diffraction system was used to collect XRD data. The diffractometer was operated at 40.0 mA with a voltage of 40.0 kV. Diffraction was collected with a 2θ range of 5° to 60° with a 0.02 step size and exposure time of 1s/step.

4.3.6 Energy Dispersive X-Ray Spectroscopy

STEM-EDS data was collected to determine the elemental composition of the samples. The JEOL ARM 200CF STEM used is equipped with Oxford X-max 100TLE windowless SDD X-Ray detectors capable of detecting oxygen. Calcium and oxygen peaks were expected, while potential contaminants such as sodium and chloride were monitored. The 0-20kV energy range was examined while 0-10kV was used to obtain more precise data collection. EDS mapping of the crystal was implemented to minimize the local electron dose and sample damage, which was observed to damage the sample and to alter the Ca:O ratio in point or line EDS collection. Primary detection of elements was performed with extended collection time with an electron dose rate of 1.8 $e^-/Å^2s$ and a total electron dose of 2.8×10^3 $e^-/Å^2$. Quantitative Ca:O data used to produce the reported Ca:O ratios was collected near the edge of 200nm to 500nm particles. Edge collection and collection from smaller particles reduced scattering within the particle and subsequent production of damaging secondary electrons. EDS mapping was collected from approximately 200 nm by 200 nm areas with electron dose rates between 20 $e^-/Å^2s$ to 40 $e^-/Å^2s$. Total electron doses were between 2×10^2 $e^-/Å^2$ to 8×10^2 $e^-/Å^2$, with an average of 26.2 $e^-/Å^2s$ and an averaged total of 8×10^2 $e^-/Å^2$ per EDS map. These high electron dose rates maximized the EDS signal while minimizing the total damage and incurred elemental loss over the approximately 10 second collection time.

4.3.7 Electron Energy Loss Spectroscopy

STEM-EELS data was acquired using a Hitachi HD2300 STEM microscope operating at 200kV. The energy range of 270-577.2 eV were examined with 0.30eV energy dispersion and EELS aperture of 3mm. Energy windows of 50eV were used to compare the ratio of O:Ca using the O K

edge and Ca L edge. Electron exposure was set to 15 seconds. The EELS data collection electron dose rate was 38$e^-/Å^2s$ while the total dose 573 $e^-/Å^2$.

4.4 Results and Discussion

4.4.1 In Situ TEM Studies of Calcium Oxalate Formation: Classical Nucleation

The free energy of the solution, interfacial energy between the particle, precursor, and the solution, as well as the local saturation of the ionic species may influence the formation pathway or pathways of crystal formation[85]. As such, multiple formation pathways may occur within the same solution if the free energy of the pathways are not significantly different [85]. The nanoscale formation of CaOx, as examined here, may occur through several different pathways, including: (1) classical crystal growth, wherein monomer units nucleate to form a central crystalline core [206]. From this central core individual chemical species attach individually, as monomers, to the surface of the forming crystal. (2) Nucleation of a crystal from oligomeric or polymeric complexes, rather than individual monomers. The particle then grows *via* oligomer or polymer subunit addition [207]. (3) Nucleation from dense liquid droplets, wherein ions aggregate together within a liquid to form an area of high ion density [208]. Upon reaching a sufficiently high local concentration the dense liquid drop crystallizes to form a crystalline nucleus. Formation from amorphous precursors may be induced by a central nanocrystal, which provides a surface for heteronucleation of amorphous particles and further crystal growth [209]. (4) Nucleation and oriented attachment, in which nanocrystalline precursors or amorphous precursors form and then aggregate to form a larger crystal [85]. Monomer, oligomer, or polymer nanocrystals or amorphous particles form separately [210]. These particles then orient and attach to form a larger crystal, which may involve internal reorganization of the nanocrystals to fit together and adhere to the larger growing crystal [85].

Figure 4.2 shows the formation of CaOx in a supersaturated solution within a GLC. Here, CaOx formed a crystalline nucleus and grew upon specific, selected facets sequentially as indicated by red arrows in figure 4.2. Corners with an angle of 120° formed within one second, indicating the initial formation of a rhombohedral CaOx particle[157,211]. Growth in the (100) plane is not directly visible since the (100) plane is orthogonal to the image. This growth in the (100) plane would increase the contrast of the particle in the image due to increased electron absorbance of the thicker crystal as is observed in figure 4.2[26]. In TEM, the contrast may be modelled *via* equation 9:

Equation 9: $$C = \frac{\Delta t \times N_o \times \sigma \times \rho}{A}$$

Where C is the contrast, Δt the change in thickness, N_o is Avogadro's number, σ is the elastic scattering cross section, ρ the density, and A the molecular weight [26]. By rearrangement of equation 9, the increases in contrast observed in figure 4.2 are related to Δt in equation 10, such that:

Equation 10: $$\Delta t = \frac{A \times C}{N_o \times \sigma \times \rho}$$

While changes such as the density (ρ) of materials may alter the contrast, the crystalline nature of the particle in figure 4.2 suggests the density of the particle is constant [26]. Additionally, the constant orientation of the crystalline particle relative to the image suggests that other factors such as rotation and diffraction contrast do not contribute to the particle contrast in figure 4.3. This increase in contrast in figure 4.2 could alternatively be due to movement out of the particle out of

focus of the microscope. However, figure 4.2 does not show an apparent decrease in image resolution, suggesting that the increased contrast is more likely due to growth in the (100) plane. The morphology of the rhombohedral particle formed in figure 4.2 resembles previous reports of CaOx monohydrate (COM) in literature[212]. COM is reported as the most stable crystal structure of CaOx, with the lowest free energy (ΔG), and is therefore preferentially formed [172]. The process in figure 4.2 resembles the classical pathway of crystal formation, where ions, atoms, or molecular species nucleate to form a crystalline core followed by the attachment of individual molecular species to the surface of the forming crystal, but may also reflect formation *via* polymeric addition of CaOx complexes [206].

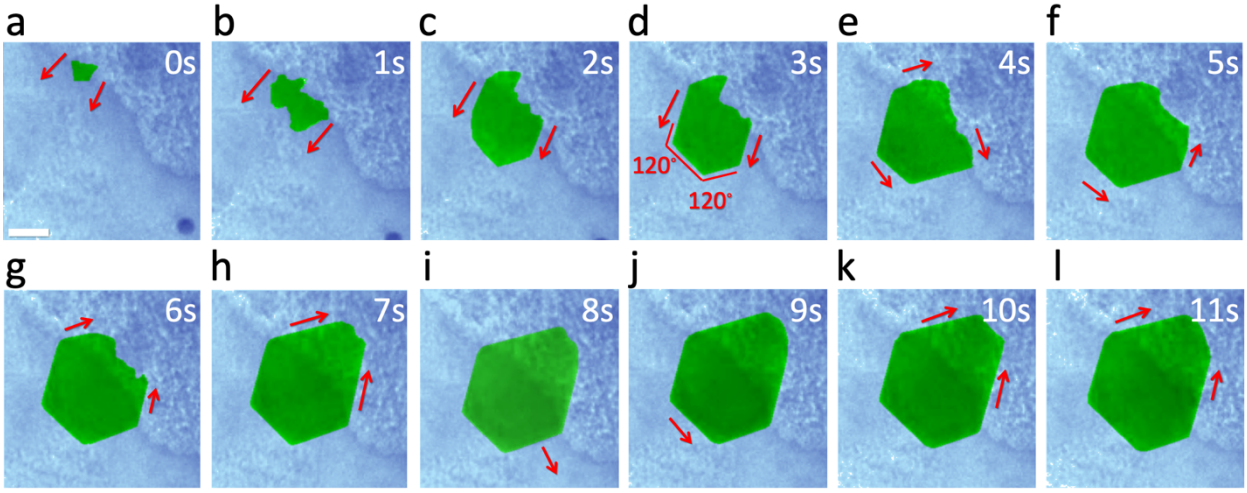

Figure 4.2. The classical nucleation pathway of CaOx crystal formation within GLC-TEM. The process starts *via* formation of a stable nucleus followed by monomer addition to the growing crystal. The particle (green) grows along specific facets as indicated by the red arrows. The time series from the beginning of particle formation is included in the upper right corner of each image. All images were collected from the same magnification. The scale bar in **(a)** is 50 nm.

4.4.2 In Situ TEM Studies of CaOx Formation: Non-Classical Nucleation

Figure 4.3 illustrates a second pathway for the formation of CaOx in the absence of citrate through four distinct stages. First, in an initial growth stage, the CaOx forms a rhombohedral precursor as indicated by 120° corners (fig. 4.3 **a**-**e**)[157,211]. This crystallization appears to be driven by a decrease in volumetric energy due to the relative internal stability of the crystal as compared to the disordered solution [213]. However, the formation of the crystal induces an energy cost due to the interfacial energy between the ordered crystal surface and the disordered solution. This change in energy may be expressed as equation 11:

Equation 11: $$\Delta G = \Delta G_S + \Delta G_V,$$

Where ΔG is the Gibbs free energy, ΔG_V is the decrease in free energy between the volume of the particle as compared to the solution which drives the nucleation, whereas an increase in ΔG_S represents the change in energy between the surface and the disordered solution [213]. The corners in figure 4.3 **(a)** through **(e)** do not appear as sharp as in figure 4.2, suggesting a particle containing both crystalline and amorphous phases. The presence of the amorphous phase and crystalline phase increases the ΔG_V of the particle as compared to a highly crystalline particle[213]. The high ΔG_V is then insufficient to offset the ΔG_s of the particle in figure 4.3 **(e).** Thus, in the second stage, the particle partially dissolves in figure 4.3 **(e)** through **(h)** to relieve this high ΔG.

However, in a third stage, the partially dissolved particles form 90° corners (fig. 4.3**h**-**l**) indicative of rectangular COM, as reported in literature, rather than fully dissolving (fig. 4.3 **m**-**n**)[212]. This increase in crystallinity lowers ΔG_V of the particle as compared to a particle containing both

crystalline and amorphous phases. Then, ΔG_V of the crystalline particle offsets the ΔG_S and causes growth of the particles shown in figure 4.3 **i** through **j**. Finally, in a fourth stage, the particles in figure 4.3 **j** through **l** coalesce to minimize their interfacial energy by reducing the surface area [214]. Comparison of figure 4.2 and figure 4.3 reveals that CaOx may mineralize *via* two energetically feasible pathways. Classical nucleation induces the formation induces that the formation of rhombohedral COM, while multiphase non-classical nucleation induces rectangular COM. The crystal structure and morphology of CaOx thus depends on the nucleation pathway and is driven by the stability of the initial precursor.

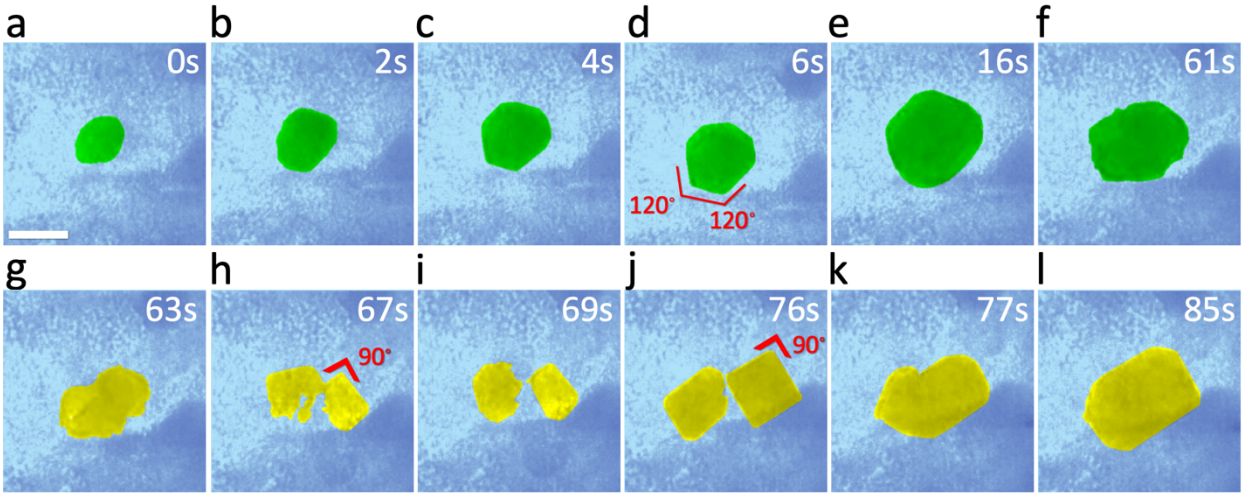

Figure 4.3. The non-classical formation pathway of CaOx within GLC in the absence of citrate. The particle shows initial classical formation *via* formation of a central nanoscale nucleus followed by ionic addition to the growing crystal (**a** through **e**). However, throughout the video the 120° corners are not as sharp as in figure 4.2, indicating the particle is not fully crystalline. Eventually, the sharpness of the corners decreases in **(f)** until the particles nearly, but not entirely, dissolve (**f** through **i**). The particle leaves behind two apparently amorphous particles, which then begin

displaying 90° corners (**j**). The particle corners continue to sharpen throughout growth, until the two particles coalescence. The scale bar in **(a)** is 50 nm.

4.4.3 In Situ TEM Studies of Calcium Oxalate Dissolution in the Presence of Citrate

GLCs containing both CaOx and citrate (fig. 4.4) display markedly different and unique particle formation as compared to CaOx synthesized without citrate. This particle formation pathway of CaOx in the presence of citrate was observed for multiple particles beyond figure 4.4 and was not observed in the absence of citrate. In figure 4.4 **(a)** through **(k)**, a particle first appears at approximately 20 nm in diameter with very low contrast. Since the multiple particles observed are unlikely to grow in the same orientation and do not appear to undergo significant growth in the X and Y coordinates of the image, the thickness in the Z orientation (t) may be considered constant. The changes in contrast thus reflect changes in the density (ρ) of the particle as implied by equations 11 and 12[26]. The particle next decreases in area while increasing in contrast, indicating an increase in density (fig. 4.4**b**-**c**). The particle then undergoes cyclic decreases in contrast and increases in area followed by increases in contrast and decreases in area (fig. 4.4**c**-3**k**). The particle initially appears amorphous but over time develops 90° corners indicative of crystallinity (fig. 4.4**h**). Throughout **(a)** through **(k)** of figure 4.4 the particle goes from taking fractions of a second to fluctuate in density to taking several seconds to cycle in density as the particle grows denser and develops facets. This increased cycle time may reflect either an increase in the stability of the particle due to increased crystallinity and density or changing concentrations of local CaOx, such as migrations of ions to the area surrounding the particle. Overall, comparison between figure 4.4 with figures 4.2 and 4.3 indicates that the presence of citrate resulted in formation of unstable CaOx particles that eventually dissolve instead of growing to a more stable form. It is unclear if

the particles are crystalline or amorphous, but the lack of defined surface facets may indicate that the particles are amorphous or may be polycrystalline. In figure 4.4 **(h),** however, the particle shows crystalline facets temporarily.

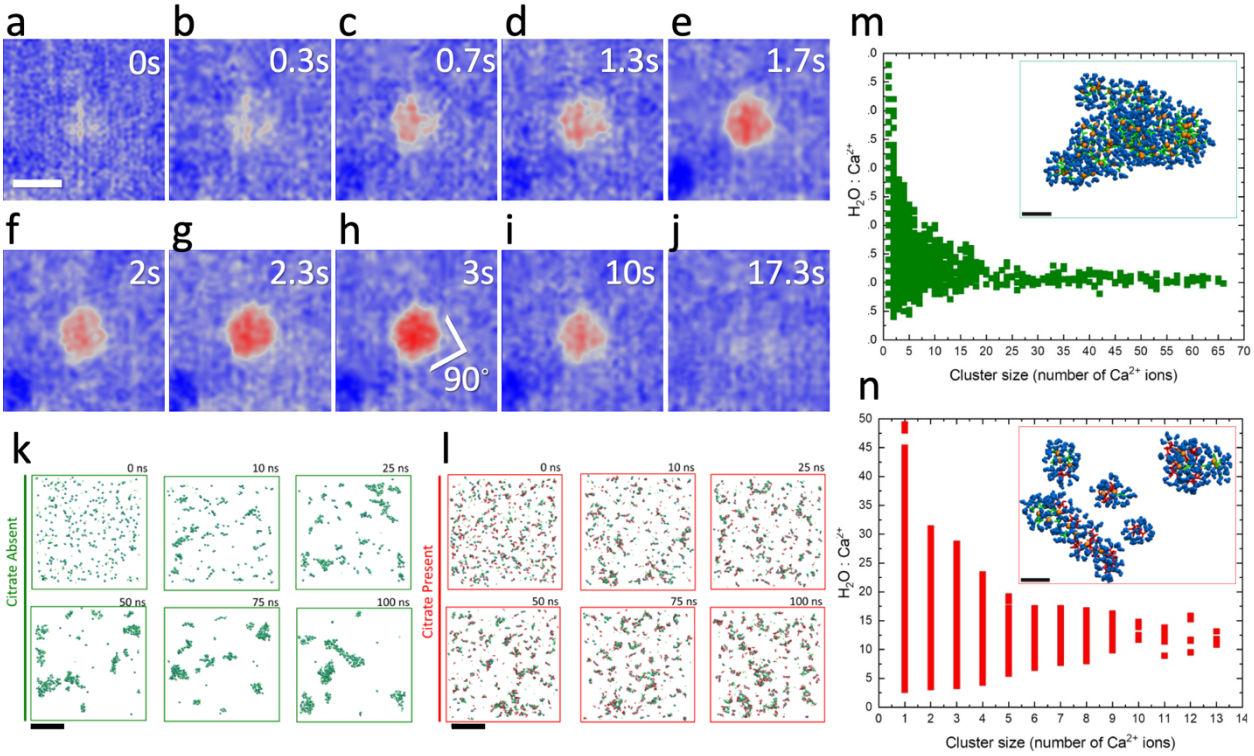

Figure 4.4. Repeated CaOx formation and dissolution in the presence of citrate. The particle forms with a diameter of approximately 20 nm, and increases in contrast throughout **(a)** through **(h)**. In **(h)**, the particle develops 90° corners. This particle fluctuates in diameter, contrast, and corner sharpness before dissolving **(j)**. In **(k)**, MD simulations shows aggregation of calcium and oxalate ions during nucleation. In contrast, in **(l)** MD simulations show that calcium:citrate interactions prevent nucleation of CaOx. All TEM images were collected at the same magnification in the same area. In **(m)** and **(n)**, the local water molecule concentration in the MD simulations in the absence of citrate **(m)** and in the presence of citrate **(n)**. A representative aggregation of CaOx formed without citrate illustrates the presence of water molecules (blue) around a CaOx particle in the inset. Oxalate anions are indicated in green, and calcium cations in orange. In **(n)**, in the presence

of citrate CaOx has a much higher water molecule to calcium ratio along the Y axis, suggesting an increase in the hydration state. Further, there is reduced aggregation along the X axis in **(n)** as compared to **(m)**. In the inset in **(n)**, smaller CaOx clusters formed in the presence of citrate illustrate a higher local water molecule to calcium ratio as compared to **(m)**. Citrate anions are indicated in red. The scale bar in **(a)** is 20 nm, 5 nm in **(k)** and **(l)**, and 1 nm in **(m)** and **(n)**.

Nucleation of CaOx from a supersaturated solution without citrate and, separately, nucleation of CaOx in the presence of 0.1M citrate were then modelled *via* MD (fig. 4.4 **k-l**). CaOx aggregated in the absence of citrate to form prenucleation clusters, which continued increasing in size and could combine with other clusters. (fig. 4.4 **k**). However, when citrate was present, the calcium ions interacted with the citrate and formed unstable complexes before dissolving (fig. 4.4 **l**). The cluster sizes in the presence of citrate were limited. The alternative calcium:citrate interactions prevented stable precipitation of CaOx, similar to the CaOx and citrate solution in figure 4.4. This effect occurs because the tridentate citrate anion, with three carboxylic acids groups capable of accepting calcium cations, exhibits stronger Ca:O bonds than the bidentate oxalate[215,216]. The alternative calcium:citrate interactions thus reduce the free calcium present which prevents stable formation of CaOx (fig. 4.4 **l**). However, calcium citrate does not precipitate since the overall structure of calcium citrate is less stable than CaOx [186]. Thus, in figure 4.4, an equilibrium between the calcium:citrate and calcium:oxalate exists, which prevents stable precipitation of CaOx. Excess calcium ions in the solution temporarily overcome the formation of soluble calcium:citrate complexes, which form CaOx nanoparticles (fig. 4.4). However, the interaction of calcium with citrate then dissolves the CaOx particles (fig. 4.4). This causes the cyclic formation

and dissolution of unstable CaOx experimentally observed in figure 4.4 **a-j** and modelled in figure 4.4 **k-l**.

4.4.4 Formation of Calcium Dihydrate in the Presence of Citrate

Previous research indicated that citrate may increase the solubility of CaOx, as mentioned in section 4.3, but only up to approximately 0.4 mM[186]. Here, much higher concentrations of CaOx were added to the GLC. The confinement effects of GLC may however alter the local ion concentrations which permits the particle dynamics observed in figure 4.3 [95,217]. The nucleation and formation of CaOx or calcium citrate at higher ionic concentrations must also be considered. At sufficiently high ion concentrations the chelating effect of citrate may be overcome and precipitation of CaOx observed as previously documented [186].

In addition to the dissolution of CaOx previously observed at equilibrium in figure 4.4, other GLCs containing CaOx and citrate showed the formation of polycrystalline COD (fig. 4.5). In figure 4.5 **a-d**, CaOx particles formed in the presence of citrate show the formation of irregular particles. Unlike figures 4.2 and figure 4.3, characteristic crystal morphologies are not observed (fig. 4.5). SAED of CaOx particles formed in the presence of citrate (fig. 4.5**e**) however shows the presence of polycrystalline COD overlapped with graphene peaks[218–220]. The individual, distinct spots identify the (100) and (210) crystal structure of graphene in figure 4.5 **(e)**[218,219]. The side by side dots in the SAED pattern indicate the presence of two layers of graphene[219]. This shows that the GLC consists of a lower single layer of graphene under the sample, while another single layer of covers the sample to encapsulate it. Circles rather than individual diffraction spots indicate the

presence of many crystals which make up the overall polycrystalline structure and identify the formation of COD rather than COM (fig. 4.5)[218–220].

In addition to the inhibitory effect of citrate discussed in section 4.3, MD simulations also determined the correlation between the ratio of water molecules around each cluster and the size of that cluster (determined by the number of calcium ions in the respective cluster) (fig. 4.4). In both the absence and presence of citrate the ratio of water molecules around a cluster to the number of calcium ions reached a limiting value for increasing cluster size and fans out for smaller clusters (fig. 4.4). In the absence of citrate, this limiting value is around 5, whereas in the presence of citrate the limiting value increases to 12.5. In the presence of citrate, the fingerlike clusters eventually collapse and capture more water than in the absence of citrate. This increases the hydration state of the CaOx formed, which contributes to the formation of COD in the presence of citrate (fig. 4.4). MD simulations of the same systems at higher pressures (100 atm) displayed little difference in aggregation mechanism or correlations of ratio of water molecules around clusters versus cluster size (Appendix D). The pressure of the system does not affect mechanisms of cluster formation; therefore, the increased pressure of 10 atm to 15 atm in the GLCs in this study is not a factor (see SI, Discussion of electron beam effects and encapsulation in GLC on CaOx formation).

The formation of COS in the presence of citrate observed in GLC was also supported by *ex situ* experiments. SEM imaging showed CaOx morphologies representative of COD, while XRD confirmed the crystal structure of COD (fig. 4**f-g**)[221]. EDS chemical analysis identified the oxygen signal increase from the expected 5:1 O:Ca in COM synthesized in the absence of citrate (fig. 4 **h**-**i**). In the presence of citrate, there was a 6:1 O:Ca ratio indicative of the formation of

COD (fig. 4 **h-i**). EELS showed slightly lower values as compared to EDS, which is likely due to electron beam sample damage (fig. 4 **h, j**). EELS did however confirm the increased oxygen signal (fig. 4 **h, j**).

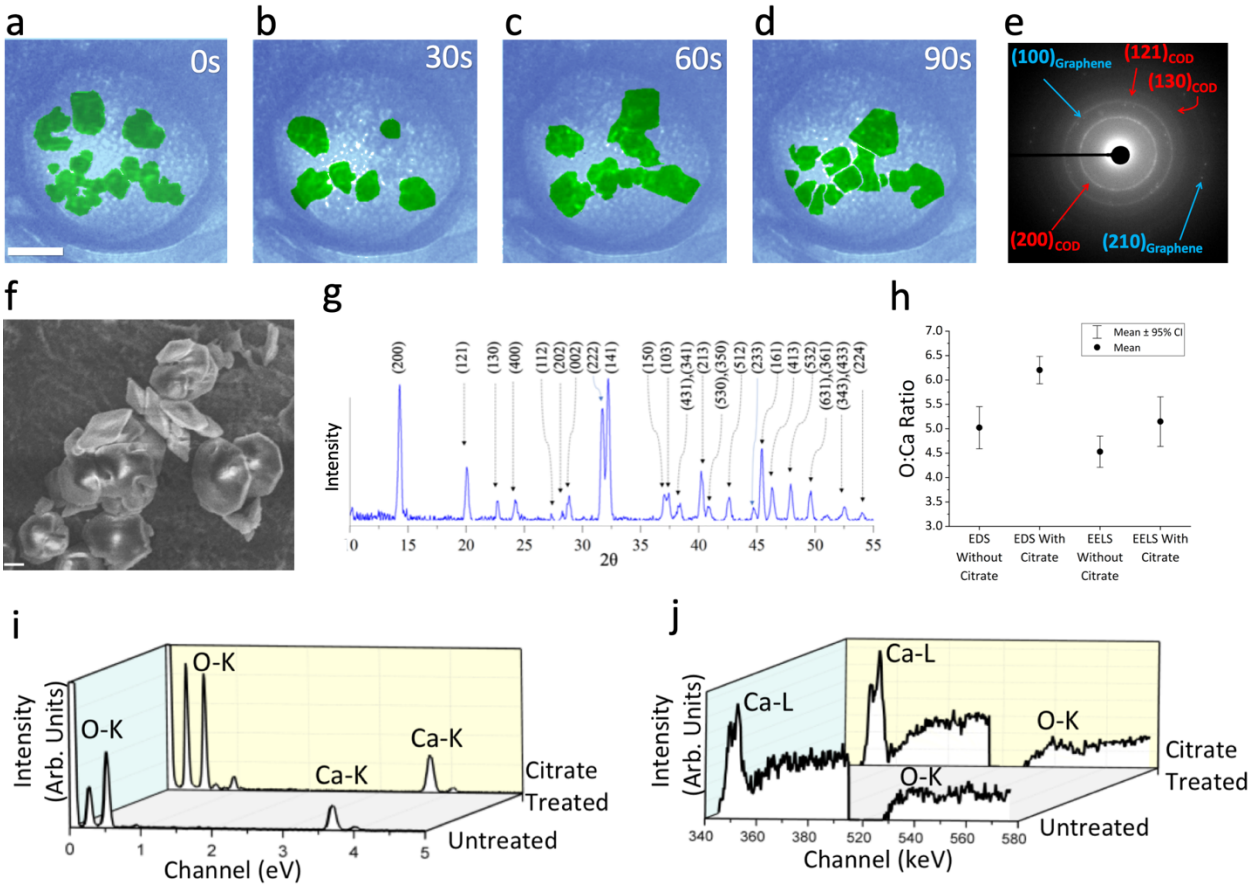

Figure 4.5. Formation of COD observed both *in situ* and *ex situ*. In **(a)** through **(d)**, a time series shows motion of CaOx nanoparticles within GLC. In **(e)**, SAED shows overlapped crystalline graphene and polycrystalline COD diffraction peaks as collected from the GLC sample. In **(f)**, SEM imaging of CaOx synthesized in the presence of citrate shows the bipyramidal morphology indicative of COD. In **(g)**, XRD of bulk CaOx samples synthesized in the presence of citrate shows the formation of COD. In **(h)**, EDS and EELS spectra of O:Ca ratios from ten *ex situ* samples without citrate and with citrate are displayed. The EDS and EELS data show a consistent increase in the O:Ca ratio in the presence of citrate. In **(i)**, a representative EDS spectrum from samples

with and without citrate show an increase in the oxygen signal in the presence of citrate. In **(j)**, comparison between the EELS spectra of *ex situ* CaOx without citrate and with citrate shows an increase in the O:Ca ratio in the presence of citrate. The scale bar in **(a)** is 100 nm. In **(f)** the scale bar is 500 nm.

In contrast to the classical crystallization model, here multiple nucleation pathways and the presence of citrate determine the morphology, crystal structure, and the hydration state of CaOx. These changes in the formation of CaOx were previously predicted to occur by interaction with amorphous precursors [184], polynuclear complexes [184], or by step-pinning of crystal facets as in the C-V model [188]. Ruiz-Agudo *et al* [184] showed that CaOx was inhibited by citrate due to citrate coating growing amorphous particles to prevent further aggregation. Here, it is difficult to find evidence for such coating. This may be due to the complexity of GLCs. However, the formation of crystalline CaOx particles occurs at or below 20 nm in both GLCs with or without citrate. These results suggest that early nanoscale nucleation events largely determine the morphology and crystal structures observed in larger crystals.

In this work, the effects of the electron beam and encapsulation in GLC were considered and shown to have minimal effects on the crystallization pathways of CaOx (Appendix D). Significant differences in CaOx particles were not observed in separate areas of the GLCs, in different GLCs, under different electron dose rates, or within different electron microscopes (Appendix D). Further, the *in situ* TEM results were supported by MD simulations and *ex situ* studies, which indicate that the CaOx crystallization in GLC reflects the crystallization of CaOx in the absence of the electron beam (fig. 4.2, 4.3, and 4.4).

4.5 Conclusions

Here, real-time TEM studies show the nanoscale nucleation of CaOx *via* two pathways. Classical nucleation leads to the formation of rhombohedral COM, the most thermodynamically favorable crystal structure of CaOx, whereas rectangular COM forms *via* non-classical nucleation. The dependence of the final crystal structure on the nanoscale nucleation pathway shown here demonstrates the importance of the initial conditions which control particle nucleation pathways. Real-time TEM studies and MD simulations then show that citrate buffers formation of stable formation of CaOx. This inhibition occurs *via* transient formation of soluble calcium:citrate complexes. At high calcium concentrations, however, the inhibiting effect of citrate is overcome, which causes formation of COD. MD dynamics show that the formation of COD rather than COM is induced during the initial nucleation of the crystal, during which the citrate draws more water into the forming CaOx nucleus. Phenomena such as the mineralization of kidney stones and calcium storage in plants may thus depend not only upon chemical or biological processes but upon kinetic and thermodynamic factors that control the nucleation pathways.

4.6 Summary

Chapter 4 elucidates classical and non-classical nucleation of CaOx *via* GLC. Classical nucleation forms rhombohedral COM, while non-classical multiphase nucleation forms square COM. GLC of CaOx in the presence of citrate then shows that citrate 1) inhibits CaOx formation by forming calcium: citrate complexes, and 2) causes formation of COD rather than COM. The presence of COD was confirmed *via* SAED of the particles formed in GLC. The GLC results were supported by extensive *ex situ* analysis including SEM, XRD, EDS, and EELS. MD modeling provided additional mechanistic insight and showed that citrate forms soluble calcium:citrate complexes to

inhibit nucleation. MD further showed that citrate increases the local water molecule concentration during nucleation, which may increase the hydration state of CaOx.

CHAPTER 5: CONCLUSIONS

Here, *in situ* TEM provides insight into the antibacterial mechanistic function of antimicrobial surface topologies as well as CaOx formation and inhibition. The antibacterial surface topologies do not require the use of any antibiotic or chemical substance. This approach has the potential to mitigate the excess use of antibiotics. Further, exposure to conventional antibiotics may be hazardous to patients who have medical conditions such as allergies or who are pregnant. In this work *in situ* TEM directly shows that antibacterial surface topologies function *via* a penetrative mechanism. Protrusions on the antibacterial surface topologies directly damage the bacteria at the point of protrusion/E. coli contact. This damage induces leakage of the cytosol followed by apoptosis and systemic bacterial death. This suggests that bacterial binding, the stiffness of the cell wall, the possibility of the polarity of the surface vs. the cell membrane, and the morphology of the individual nanopillars may be more important that stretch bacteria between nanopillars. The MPs on which the rough antibacterial surface topologies were synthesized also have unique applications. As opposed to the previously described films or fibers, MPs have the potential to be used within other media such as liquids, gels, or powders.

In situ TEM and MD simulations also directly observed multiple nanoscale nucleation pathways of CaOx. Classical nucleation produced rhombohedral CaOx, while non-classical nucleation produces rectangular CaOx. Citrate is shown to play a dual role in CaOx crystallization. First, at low concentrations of CaOx citrate produces soluble calcium:citrate interactions. This decreases the calcium available for CaOx formation. At higher concentrations of CaOx, CaOx overcomes the inhibitory effect of citrate. Citrate then draws additional water into the forming CaOx crystal. This increases the hydration state of CaOx from the more stable COM to COD.

This work highlights the importance of mechanistic understanding of biological activities at nanoscale. Specifically understanding the mechanism behind the antimicrobial function of novel nanotuxtured surfaces for prevention of pathological biominerals in human body. In agreement with previous studies, the viability of bacteria within liquid EM is further supported. The nanoscale interaction of bacteria with other materials can be directly observed rather than inferred *via* static TEM methods. Additionally, this work shows that biologically relevant minerals may be synthesized in GLC. Comparison of *in situ* TEM and MD simulations provides mechanistic insight into biomineralization of CaOx.

CHAPTER 6: FUTURE DIRECTIONS

6.1 Project 1: TEM Studies of Metallic Nanoparticles with Controlled Rough Surface for Antibacterial Studies

6.1.1 Introduction

Metal nanoparticles, surfaces, and ions have shown antibacterial properties[1–4]. Examples of these metals include silver, titanium, zinc, magnesium, and copper[1–4]. The fundamental antibacterial mechanism has been attributed to the generation of reactive oxygen species by the metals[1]. Other mechanisms may include leeching of metal ions, which then bind to and damage cell wall proteins or induce intracellular damage to lipids, enzymes, or nucleic acids[5]. A number of copper alloys have shown antibacterial activity, including electrolytic tough pitch copper, red brass, yellow brass, phosphor bronze, nickel-aluminum bronze, and nickel silver[6]. This antibacterial activity is positively correlated with the concentration of copper within the alloy[6].

Many studies have indicated that the antibacterial activity of silver occurs through multiple mechanisms: (1) Silver nanoparticles bind to the cell membrane, induce structural damage, and subsequently kill the bacteria[7]. (2) Silver nanoparticles form free radicals which damage the bacteria cell membrane[7]. (3) Silver nanoparticles leech silver ions, which then damage enzymes by interacting with thiol groups[7]. (4) Silver ions generate reactive oxygen species[7]. These reactive oxygen species then inflict diffuse cellular damage[7]. (5) Silver may react with phosphorous[7]. Thus, silver may damage DNA, which contains high concentrations of phosphorous[7]. (6) Silver may induce dephosphorylation of bacterial signaling molecules[7]. This dephosphorylation prevents bacterial growth and replication[7].

Previous works have also examined the effect of silver nanoparticle shapes[4]. Studies by Pal et al., among other groups, have observed that controlling the morphology of AgNPs may drastically increase the antibacterial efficacy beyond ionic silver[4]. The mechanism of this increased antibacterial effect may due to structural damage to the cell membrane or increased ion release from the AgNPs due to changes in surface area[8]. Previous works have suggested the antibacterial activities may be facet specific *via* benchtop methods, but have not provided direct visualization of this effect[8].

6.1.2 Objectives

Here, this future work aims to visualize AgNP and bacteria interactions *via* in situ TEM (fig. 6.1). Multiple AgNP morphologies will be examined. Chemical mapping will provide insight into ion release from the AgNPs. AgNPs of distinct morphologies will be compared to provide insight into the fundamental antibacterial mechanism of metal AgNPs. The *in situ* TEM aims to observe mechanical damage to bacteria induced by silver morphology *via* encapsulation of AgNPs and bacteria in GLC. First, smooth spherical, rough spherical, rod-shaped, and triangular AgNPs will be synthesized *via* previously described protocols. Conventional benchtop antibacterial testing will quantify the efficacy of the antibacterial AgNPs. Then, conventional TEM techniques will provide static imaging. Chemical mapping *via* EDS and EELS will show whether the silver leeches from the AgNPs into the bacteria cytosol. GLC will then be used to visualize the real-time antibacterial mechanism of AgNPs. The distinct morphology and distinct facets may provide optimal membrane disruption, provide increased surface area for silver ion leeching, or stretch the bacterial cell envelope as previously described for rough antibacterial polymers. These insights will allow

optimal synthesis of antibacterial AgNPs and provide insight into designing next-generation antibacterial treatments.

6.1.3 Literature Review

Bacteria can be classified as gram negative or gram positive based upon the properties of their cell envelope[9]. These different cell envelope structures exhibit different properties, which necessitates studies of both gram negative and gram positive bacteria[9] Molecular mechanisms of membrane targeting antibiotics. Several previous works have compared the effect of triangular, cubic, spherical, rough spherical, rod shaped, cuboctahedral, twinned icosahedral, and decahedral morphologies AgNP morphologies against multiple species of both gram positive and gram-negative bacteria[3,4,8,10,11]. Morones et al. compared the antibacterial effects of silver nanoparticles against the gram-negative *E. coli, P. aeruginosa, V. cholera*, and *S. typhus*[8]. The authors utilized AgNPs with cuboctahedral, twinned icosahedral, and decahedral morphologies[8]. The silver nanoparticles attached to the surface of the cell membrane preferentially along the {111} facets[8]. This attachment disturbed the permeability of the cell envelope and respiration[8]. The AgNPs also crossed the cell envelope and may have interacted with thiol or phosphate within the cytosol[8]. The AgNPs released silver ions, which may also induce diffuse cell damage[8].

Pal et al. examined the antimicrobial activity of spherical AgNPs, rod shaped AgNPs, triangular AgNPs, and ionic $AgNO_3$ on *E. coli*[4]. The authors observed that triangular AgNPs exhibited the highest antibacterial effect, followed in order by spherical AgNPs, rod shaped AgNPs, and ionic $AgNO_3$[4]. Triangular AgNPs showed highly effective antibacterial activity at 1 ug, spherical nanoparticles required 50 µg to 100 µg, whereas rod shaped and $AgNO_3$ showed only moderate

antibacterial activity at 100 ug[4]. Thus, controlling the morphology of AgNPs can increase the antibacterial activity of silver by several magnitudes[4]. Pal et al. suggested the increased antibacterial effect may be due to the prominent {111} facets in triangular AgNPs, similar to Morones et al[4,8]. In contrast, the spherical AgNPs contained predominant {100} facets, while the rod-shaped AgNPs had {100} facets on the elongated sides with {111} facets on the ends[4]. Actis et al. did not observe differences in the antimicrobial properties of spherical, cuboidal, or triangular shaped silver nanoparticle against *S. aureus*.[3]

Acharya et al. showed that spherical silver nanoparticles had increased antibacterial properties as compared to rod shaped silver nanoparticles[10]. The authors examined the effect of these AgNPs on gram-negative *E. coli, P. aeruginosa,* and *K. pneumoniae,* as well as on gram-positive *S. aureus* and B. subtilis[10]. For all bacterial strains tested, the mean inhibitor concentration (MIC) of spherical AgNPs was between 184 µg/ml to 190 µg/ml. For rod-shaped nanoparticles the MIC was between 320 µg/ml to 358 µg/ml[10].

Cheon et al. investigated the antibacterial effect spherical, disk shaped, and triangular AgNPs against *E. coli, S. aureus,* and *P. aeruginosa*[11]. The spherical AgNPs were most effective, followed by disk-shaped AgNPs, while the triangular AgNPs exhibited the least antibacterial efficacy[11]. The authors observed that the antimicrobial activity is positively associated with increased surface area[11]. Cheon et al. suggest that the increased surface area may increase silver ion release, which then induces bacterial death[11].

6.1.4 Technical Approach

Task 1: Sliver Nanoparticle Synthesis: Numerous approaches to synthesizing AgNPs with distinct shapes have been previously described. A benchtop chemical approach using silver nitrate ($AgNO_3$) as a silver source and poly(vinyl pyrrolidone) (PVP) as a capping agent has been described by multiple researchers[12–15]. Altering the chemical reagent ratios, pH, temperature, and additives can precisely produce AgNPs with distinct morphologies[12–15]. This chemical benchtop approach will not require purchasing specialized equipment or multistep complex approaches[12–15].

Liang et al. described a method for synthesizing smooth spherical AgNPs using $AgNO_3$ in the presence of polyethylene glycol (PEG) and PVP[12]. The authors mixed PVP and $AgNO_3$ at a precise molar ratio of 8:1 at a temperature of 260C[12]. In contrast, Laing et al. described a method to synthesize rough spherical AgNPs[13]. The authors used PVP and $AgNO_3$ solution at room temperature[13]. Ascorbic acid was then added to the solution during vigorous mixing[13]. The authors were further able to control the AgNP diameter by adjusting the $AgNO_3$ to PVP ratio[13]. Sun et al. described a method for synthesizing cubic AgNPs[14]. The authors reduced $AgNO_3$ with PEG and PVP by at 160 C with a molar ratio of 1.5:1 PVP:$AgNO_3$[14].

Dong et al. described a similar chemical method for synthesis of triangular AgNPs[15]. The authors first synthesized spherical AgNPs by reduction of silver nitrate with sodium borohydride at 0C using an icebath[15]. The authors then heated to solution to 70 C which caused additional reaction with the remaining $AgNO_3$ and formation of triangular AgNPs *via* Oswald ripening[15].

Task 2: Benchtop Antibacterial Testing: E. coli LB solutions will be synthesized using the procedure described in appendix B1. Separately, cuboidal AgNPs, rod-shaped AgNPs, smooth

spherical AgNPs, and rough spherical AgNPs will be synthesized as previously described. The AgNPs will then be added to separate LB cultures (Appendix B1, B4). The cultures will then be incubated at 37.5C as described in appendix B2. The bacteria concentration will be analyzed *via* CFU counting prior to addition of the AgNPs, after four hours, and again after eight hours using the same CFU procedure (appendix B7, B8).

Task 3: Ex Situ TEM: Ex situ TEM as described in appendix B5 will be used to validate the *in situ* TEM. Briefly, *E. coli* LB cultures will be synthesized using the procedure described in appendix B2. Cuboidal AgNPs, rod-shaped AgNPs, smooth spherical AgNPs, and rough spherical AgNPs will be added to separate cultures. The cultures will be incubated at 37.5C as described in appendix B2. After 4 hours of incubation, the *E. coli* and AgNP solutions will be preserved in glutaraldehyde as described in Appendix B5. The preserved samples will then be ultramicrotomed to produce 100 nm thick cross sections and imaged *via* TEM and chemically analyzed *via* EDS and EELS mapping. This approach will show observed facet dependent and morphological dependent interactions between the bacteria and the AgNP. EDS and EELS will determine of silver ions or AgNPs were able to cross the bacterial envelope and damage the internal structure of *E. coli.*

Task 4: Graphene Liquid Cell: E. coli solutions will be synthesized as described in appendix B2. Cuboidal AgNPs, rod-shaped AgNPs, smooth spherical AgNPs, and rough AgNPs will be added to separate LB cultures and placed into a 37.5C incubator as described in appendix B4. After 20 minutes incubation, the sample will be centrifuged, the LB removed, and the pellet rehydrated in PBS. The AgNP and *E. coli* solutions will then be imaged in GLC as described in appendix A.

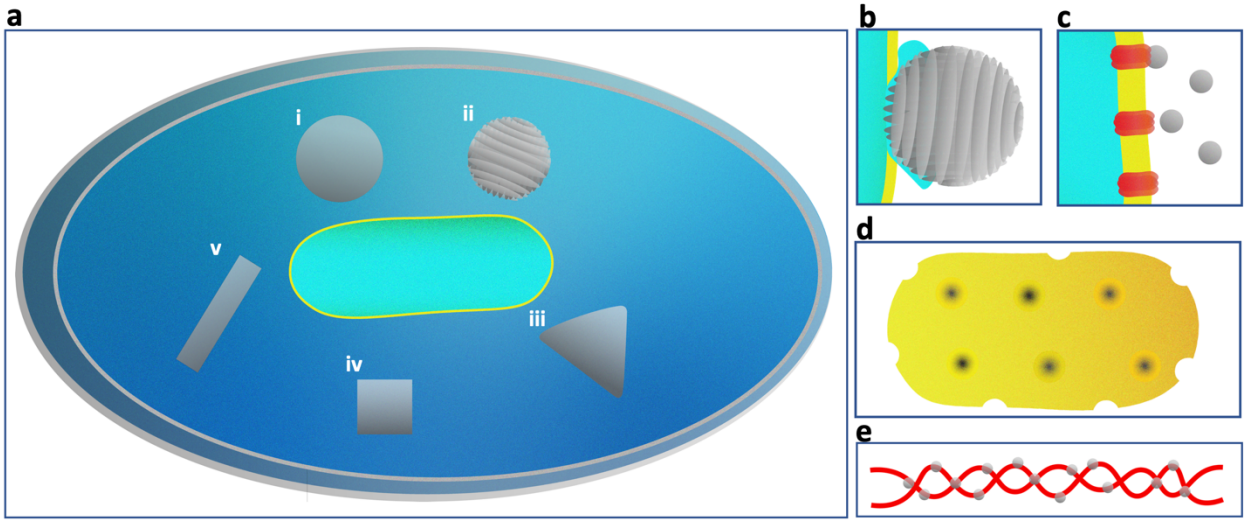

Figure 6.1. In **a**, a graphene liquid cell bubble contains an *E. coli* bacterium. The bacterium is surrounded by smooth silver nanoparticles (**i**), rough spherical (**ii**), triangular nanoparticles (**iii**), cuboidal (**iv**), and rod shaped (**v**) AgNPs. In **b**, a rough nanoparticle damages the cell envelope, allowing leakage of the cytosol. In **c**, AgNPs interactant with membrane bound proteins, which alters cell physiology. In **d**, damage to the surface of the *E. coli* is illustrated, resulting in visible dips in the surface. In **e**, silver ions bind to nucleic acid, preventing protein production and bacterial reproduction.

6.2 Project 2: TEM Studies of Antiviral Metallic Nanoparticles with Controlled Rough Surface for Antiviral Studies

6.2.1 Introduction

Modern vaccinations have eliminated or drastically reduced the incidence of many viral diseases, including smallpox, polio, and the measles[16]. However, vaccinations are highly specific to the viral strain and take time to develop and produce at mass scale before the population can be effectively treated[17]. The recent outbreak of coronavirus disease 2019 (COVID 19) is an excellent example, where it is quite possible that an effective vaccine will be developed[18]. Unfortunately, the time

and effort required to develop vaccines against emergent pathogenic viruses means that many people will contract and die from COVID 19 before a vaccine will be developed[19]. Previous research suggested that future outbreaks from wet markets were inevitable, but it was not possible to design a vaccine prior to the emergence and characterization of COVID 19[20].

Due to the inherent limitations of vaccinations, broad preventative approaches are required to stop or slow the spread of other pathogenic viruses in the future. However, the relative simplicity of viruses limits possible broad-spectrum antiviral strategies[21]. Viruses do not even fully meet the classical definition of life, which is defined as: 1) homeostasis, 2) organization, 3) metabolism, 4) growth, 5) adaptation, 6) response to stimuli, and 7) reproduction[21]. Viruses lack an independent metabolism, cannot reproduce apart from a host cell, do not grow, and do not actively maintain a homeostatic environment[21]. This renders many conventional antimicrobial approaches ineffective: it is not possible to interfere with non-existent enzymes or non-existent metabolism[21]. Thus, antiviral treatments most often focus on the host organism, either by preventing replication of the virus within the host cell or utilizing the host's immune system[22].

One potential antiviral approach is development of surfaces that quickly destroy the virus[1]. Since viral transmission may occur through surface contact, antiviral surfaces would mitigate or slow the spread of the viral disease[1]. Viruses may live on surfaces such as plastics or steel for hours or days[1]. In contrast, surfaces such as copper exhibit antiviral properties and degrade viruses in less than four hours[1]. Previous works have proposed that the antiviral mechanism is occurs *via* copper oxidization, which produces reactive oxygen species (ROS)[1]. These ROS first degrade the outer viral protein layer and then inactivate the nucleic acid[1]. This would explain why surfaces with low

oxidation rates such as stainless steel do not exhibit the same antiviral properties[23]. Ionic metal solutions and metal nanoparticles also induce antiviral effects[2,24]. These effects may also be due the release of ROS from the metal ions or nanoparticles[1].

Other microbes, such as bacteria, have shown the same sensitivity to ROS from metal ions, surfaces, and nanoparticles[6]. In addition to the ROS effects, the morphology of metal nanoparticles has been shown to drastically alter the antibacterial activity of metals[3,4,8,10,11]. These differences may be due to other mechanisms, such as structural damage to the cell membrane or changes in the available surface area for ion leeching[3,4,8,10,11]. Here, this future direction aims to characterize the antiviral properties of copper nanoparticles with distinct morphologies. Benchtop testing will show the *ex situ* effectiveness of ionic copper and CuNPs of varying morphology. *In situ* TEM will describe the antiviral mechanism of copper nanoparticles. The unique CuNP morphologies may exert shape-dependent and facet-dependent interactions between the CuNPs and the viruses. This approach will both provide insight into the optimal shape and structure of antiviral nanoparticles and insight in the antiviral mechanism.

6.2.2 Objectives

CuNPs will be synthesized with varying morphologies: smooth spherical, rough spherical, triangular, and bud-shaped nanoparticles using previously described protocols[25–27]. Human coronavirus 229E will be commercially purchased. While genetically and structurally similar to COVID-19, human coronavirus 229E is far less pathogenic than COVID 19[28]. Human coronavirus 229E and CuNPs will be mixed in the same solution and incubated to allow CuNPs to degrade the virus. *Ex situ* TEM imaging will then describe the static damage to the protein shell. EDS and

EELS chemical mapping will describe the location of the copper ions. The virus and CuNP solutions will also be visualized *in situ via* GLC (fig. 6.2). This approach will allow real-time observation of morphologically induced damage to the coronavirus protein shell by the CuNP. CuNPs may induce stretching of the protein membrane, penetrate the membrane, or induce surface-area dependent oxidative stress. This GLC approach will also include EDS and EELS chemical analyses. EDS and EELS analyses will indicate if copper ions are able to cross the protein shell and inactivate the nucleic acid prior to protein degradation, or if prior destruction of the protein shell is essential for nucleic acid damage.

6.2.3 Literature Review

Coronaviruses, including COVID-19, consist of (1) a phosphate lipid bilayer membrane derived from the host organism, (2) structural proteins embedded in the membrane, including membrane protein (M), envelope small membrane protein (E), glycoprotein spikes (S), and (3) RNA and nucleoprotein (N) within the outer membrane and protein shell[29]. This structure is highly conserved among coronaviruses[30]. The M protein is a glycoprotein which plays the primary structural role of the virus[30]. The M protein has three domains: the N terminal domain is on the outside of the membrane, with a triple spanning transmembrane domain, and C terminal domain within the membrane[30]. E protein is essential in infection and assembly of the virion during reproduction[31]. E protein is a small integral protein embedded in the membrane. It contains a single hydrophobic domain. E protein may adopt different three morphologies: (1) an external N terminal, with an embedded transmembrane region, and an internal N terminal, (2) an external C terminal, with an embedded transmembrane region, or (3) internal N and C terminals, with an membrane imbedded region[31]. Multiple chemical modifications may alter E protein function, including

ubiquitination, glycosylation, myristylation, and palmitoylation[32]. The S protein appears as spikes on the surface of the coronavirus[33]. It contains both S1 and S2 subunits[33]. The S1 subunit binds to host cell receptors[33]. The S2 subunit then fuses the viral and host membranes[33]. The N protein is essential in packing the viral nucleic acid into nucleocapsids within the viral shell[34].

Previous works by Broglie et al. and Tavakoli et al., among others, showed that copper nanoparticles exhibit antiviral properties[24,35]. The antiviral mechanism of copper was suggested to occur through production of hydroxyl radicals and hydrogen peroxide *via* the following oxidation/reduction reactions:

$$2Cu^{+} + 2O_2 \longrightarrow 2Cu^{2+} + 2O_2^{-}$$

$$2O_2^{-} + 2H^{+} \longrightarrow H_2O_2 + O_2$$

$$Cu^{+} + H_2O_2 \longrightarrow Cu^{2+} + H^{-} + H^{\cdot}$$

The reactive oxygen species may then attack and degrade the viral protein coating[1]. Following the degradation of the protein coating the copper can also bind to the nucleic acid to fully inactivate the virus[1]. This prevents transcription of the viral RNA or DNA and reproduction of the virus[1]. The simplicity of this approach suggests that copper may be effective against a broad variety of viruses.

The surface morphology of nanoparticles can also impact the degradation of viral protein coating. While research into antiviral metal nanoparticle treatments has been limited, extensive works have shown that the surface morphology of nanoparticles may influence antibacterial effects. Antibacterial metals include silver, copper, titanium, zinc, and magnesium, along with metal

alloys[1–4]. These metals have been synthesized as spherical, rough spherical, triangular, cubic, rod shaped, cuboctahedral, twinned icosahedral, decahedral, and bud-shaped morphologies[3,4,8,10,11]. Synthesis of nanoparticles with optimal morphologies was shown to increase the antibacterial effect be several orders of magnitude[3,4,8,10,11]. For example, Pal et al. showed that the prominent {111} facet of triangular AgNPs drastically increased the antibacterial efficacy of silver over spherical, rod shaped, or silver nitrate[4]. Other studies suggested that changes in the surface area of the metal nanoparticles may increase ion leeching, which then directly damages the bacteria[11]. Here, this future direction will examine if CuNP morphology exhibits the same shape dependent effect in viruses as nanoparticles do against bacteria[3,4,8,10,11]. The antiviral properties may occur through facet-dependent interactions, structural damage due to CuNP and protein interactions, or by changes in the surface area available for ion leeching.

6.2.4 Technical Approach

Task 1: Copper nanoparticle synthesis: Previous works described synthesis of copper nanoparticles with distinct morphologies using variations of a simple benchtop copper reduction approach[25]. Liu et al. described a chemical benchtop method for synthesis of spherical CuNPs[25]. Briefly, the authors prepared a solution containing copper (II) sulfate pentahydrate and PVP[25]. A separate solution of ascorbic acid was heated to 60C and added the copper sulfate solution during stirring[25]. The authors used hydrogen sulfate or sodium hydroxide to adjust the pH of the solution[25]. Under pH 5, the nanoparticles formed uniform spheres. However, under pH 11 rough spherical CuNPs[25].

Sampath et al. described a chemical benchtop method for synthesizing bud-shaped copper nanoparticles[26]. The authors used a chemical reduction method similar to Liu et al[25,26]. The authors increased the concentration of ascorbic acid to 3.4 mol/L at neutral pH from the 1.0 mmol/L to 2.5 mmol/L described by Liu et al[25,26]. This simple change was sufficient to produce elongated bud-shaped copper nanoparticles[26]. Wozniak-Budych et al. used a method similar to Sampath et al. and Lie et al. but utilized 340 mmol/L of ascorbic acid to produce triangular CuNPs[25–27].

Task 2: In Situ Electron Microscopy: Commercially purchased human coronavirus 229E will be hydrated in phosphate buffered saline (PBS). In separate solutions, smooth spherical, rough spherical, triangular, or bud-shaped CuNPs will be added to the human coronavirus 229E. The sample will be encapsulated in GLC as described in appendix A. EDS and EELS mapping will be used to map the chemical contents of the solution. CuNPs may leech copper ions into the solution producing reactive oxygen species and damaging the RNA within the virus.

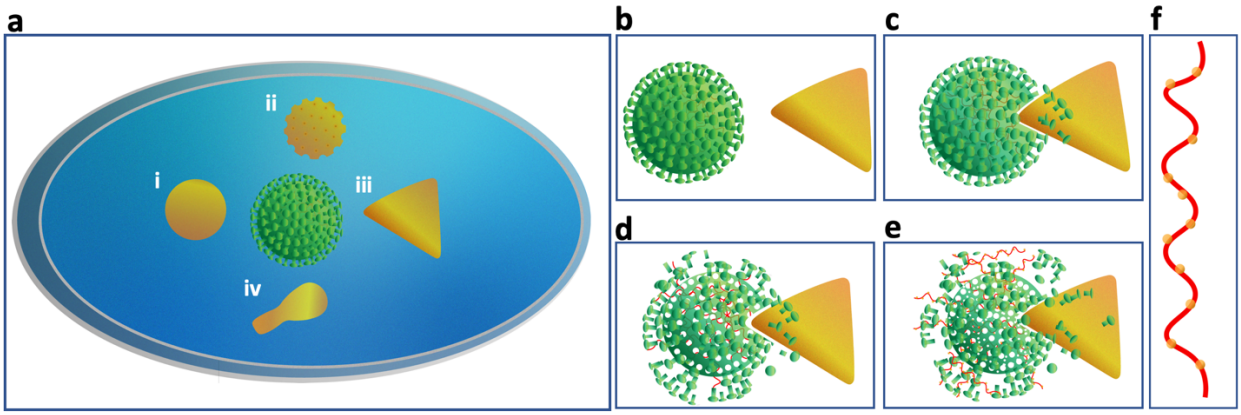

Figure 6.2. A coronavirus (center) is encapsulated in GLC **(a)**. The coronavirus is surrounded by smooth spherical (**i**), rough spherical (**ii**), triangular (**iii**), and bud-shaped (**iv**) CuNPs. In **b-e**, a triangular CuNP damages the coronavirus. First, the structure breaks down the protein shell (**b-c**), causing diffuse damage (**d**). This allows the RNA within the coronavirus to leak out of the virus,

where the RNA can be degraded or damaged by copper ions (**e**). In (**f**), copper ions bind a single stranded RNA, which damages the RNA or binds to the RNA to prevent replication of the virus.

6.3 Project 3: Effect of Trace Metals on Calcium Oxalate Formation

6.3.1 Introduction

CaOx formation is essential in plant biology but may also cause kidney stones in humans and may cause scaling in industrial water treatment[36,37]. CaOx may be monohydrate, dihydrate, or trihydrate[38]. Amorphous CaOx has been synthesized in the laboratory setting but is unstable[38]. The hydration state and crystal structure influence the morphology and mechanical properties of the material[39,40]. Further, the hydration state and crystal structure may alter cell wall adhesion, which may influence the formation of kidney stones[41]. Previous research has explored the influence of trace metals on CaOx[42–45]. These metals influence the crystal structure[42–45]. Thus, the presence of trace metals may prevent, cause, or alter the formation of kidney stones and have implications for plant science and agriculture.

6.3.2 Objective

The nanoscale formation of CaOx and the influence of an organic molecule, citrate, was explored *via* GLC in Chapter 4. In this future direction, the GLC technique will also be used to examine the effect of Cd and Zn on CaOx formation (fig. 6.3). In addition to imaging and electron diffraction, metals are ideal for chemical mapping. Techniques such as EDS and EELS mapping could measure the distribution of the metals within the GLC. Thus, here real-time imaging, diffraction, EDS and EELS will thoroughly characterize the influence of heavy metals on CaOx. Cd and Zn may be

bound within the material to induce lattice strain, alter the crystal formation pathway, or coat the surface of the CaOx crystals to prevent crystal growth. Cd and Zn may promote or inhibit the formation of COM, COD, COT, or ACO.

6.3.3 Literature Review

Multiple studies have examined the effect of trace metals on CaOx formation due to the high rate of kidney stones, which causes significant human suffering and high financial costs[42–45]. These metals include Zn, Mn, Cu, Al, Fe, Mg, and Se[44–47]. Many of these studies have produced conflicting results, which may be due to differences in the experimental approach (Table VI.III)[48–52]. For example, some studies may focus on a simplified chemical model, on the effect of dietary consumption of metals on clinical kidney stone formation, measurement of metal concentrations in the blood, or measurement of the metal concentrations[43,48–53]. Additionally, experiments may be performed at different a pH, with different molar concentrations, or in the presence or absence of other ions and proteins.

Mazen et al. observed the incorporation of heavy metals, Cd, Pd, and Sr, in CaOx crystals in plants grown in metal contaminated soils[54]. The authors suggested that this incorporation into CaOx crystals, which play a structural role, may mitigate the toxic effects of the heavy metals. McBride et al. previously observed the formation of CaOx in the presence of Cd and, separately, in the presence of Zn using benchtop chemical approaches[42]. Cd substituted within the CaOx crystal and formed COM[42]. Zn did not substitute into the CaOx crystal, but caused the formation of COD, which is typically less stable than COM. McBride et al. however relied on SEM and XRD characterization techniques without real-time observation of the crystal formation[42]. In subsequent

publication, McBride et al. showed that trace amounts of Pb substituted into CaOx crystals *via* similar methodology[55]. Pb also caused formation of COD rather than COM[55].

Table 6.1. Summary of metal induced changes in CaOx formation.

Element	Dietary	Urine concentration	Blood Serum Concentration	Chemical, structural effect	Notes
Zn	Higher in stone formers.[48] Lower in stone formers.[49] No effect.[50]	Higher in stone formers.[44,45,49]	No difference.[44] Lower in stone formers.[49]	No effect.[56] Inhibits.[50,51,57,58]	Forms separate ZnOx.[42] Favors COD.[42]
Mn	Lower in stone formers.[50,59]	Lower in stone formers.[44,59]	No difference.[44]	Inhibition.[60]	
Cu	Higher in stone formers.[43]	Higher in stone formers.[49] Lower in stone formers.[44] No effect.[43]	No difference.[44,49]	Inhibits.[51]	
Al				Inhibits.[51,52]	
Fe	No effect.[50]	Higher in stone formers.[49]	Lower in stone formers.[49]	Inhibits.[57]	
Mg	No effect.[53]	Lower in stone formers.[32] Higher in stone formers.[49]	No effect.[49] Inhibits.[53]	Inhibition.[46,53,61]	Forms COD rather than COM.[62]
Se	Inhibits.[63]			Inhibition.[47,64]	COM, but BSA causes COD and COT formation.[64]

6.3.4 Technical Approach

Previous works have shown that Cd can substitute within a CaOx crystal. However, Cd causes formation of COD rather than the more stable COM. In contrast, Zn does not substitute within CaOx but preferentially forms ZnOx. Here, the formation of CaOx in the presence of Cd and Zn will be compared *via* GLC. This effect may occur through several nanoscale mechanisms: (1) Cd or Zn may cause instability within the crystal structure through lattice strain, causing dissolution of the crystal, (2) Cd or Zn may cause instability within the crystal structure through lattice strain, which causes expulsion of the Cd or Zn from within the crystal, (3) Cd or Zn may alter the water content within the early-stage formation of the nanoparticle, increased the hydration state, (4) Cd or Zn may coat the surface of the nanoparticle, preventing nanoparticle growth, (5) Cd or Zn may offer alternative interactions for the oxalate anion.

CaOx will be formed by mixing 0.1M CaCl2 and 0.1M NaOx (appendix C). In separate solutions, 0.1M Zn chloride will be added to the CaOx solution or 0.1M $CdCl_2$ will be added to the CaOx solution. The CaOx solutions will then be encapsulated in GLC (appendix A). The CaOx particles may form COM crystals, COD, COT, or ACO. Each of these hydration states present with distinct morphologies. SAED will provide additional confirmation of the crystallinity of the particles. EDS and EELS mapping will show the chemical content of Cd and Zn within the forming particles.

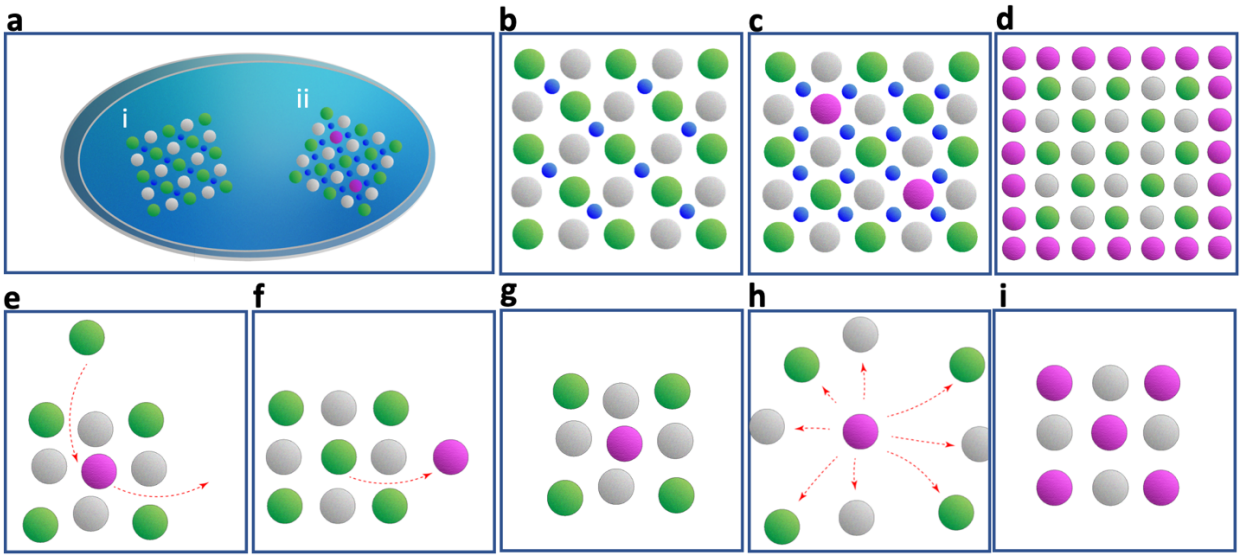

Figure 6.3. In **a**, a GLC encases a COM nanoparticle (**i**) and a COD nanoparticle (**ii**). In **b** a CaOx crystal contains calcium (green), oxalate (grey), and water (blue). In **c**, a CaOx crystal contains additional water from the COD structure and Cd as well as calcium. In **d**, CaOx is coated with a Cd layer, preventing crystal growth. In **e** and **f**, a Cd ion distorts the crystal. The Cd ion exits the particle, and is replaced by a calcium ion. In **g** and **h**, the calcium crystal is distorted by a Cd ion, which then causes dissolution of the particle. In **i**, the Cd and oxalate form a Cd oxalate nanoparticle rather than a CaOx nanoparticle.

CITED LITERATURE

[1] S. M. Kelleher, O. Habimana, J. Lawler, B. O'reilly, S. Daniels, E. Casey, A. Cowley, *ACS Appl. Mater. Interfaces* **2016**, *8*, 14966.

[2] J. Hasan, H. K. Webb, V. K. Truong, S. Pogodin, V. A. Baulin, G. S. Watson, J. A. Watson, R. J. Crawford, E. P. Ivanova, *Appl. Microbiol. Biotechnol.* **2013**, *97*, 9257.

[3] S. Pogodin, J. Hasan, V. A. Baulin, H. K. Webb, V. K. Truong, T. H. Phong Nguyen, V. Boshkovikj, C. J. Fluke, G. S. Watson, J. A. Watson, R. J. Crawford, E. P. Ivanova, *Biophys. J.* **2013**, *104*, 835.

[4] C. D. Bandara, S. Singh, I. O. Afara, A. Wolff, T. Tesfamichael, K. Ostrikov, A. Oloyede, *ACS Appl. Mater. Interfaces* **2017**, *9*, 6746.

[5] C. Serrano, L. García-Fernández, J. P. Fernández-Blázquez, M. Barbeck, S. Ghanaati, R. Unger, J. Kirkpatrick, E. Arzt, L. Funk, P. Turón, A. del Campo, *Biomaterials* **2015**, *52*, 291.

[6] D. P. Linklater, M. De Volder, V. A. Baulin, M. Werner, S. Jessl, M. Golozar, L. Maggini, S. Rubanov, E. Hanssen, S. Juodkazis, E. P. Ivanova, *ACS Nano* **2018**, *12*, 6657.

[7] O. Mohamed, M. Monga, J. C. Calle, *J. Nephrol. Ther.* **2015**, *5*, 1000198.

[8] P. McColgan, S. J. Tabrizi, *Eur. J. Neurol.* **2018**.

[9] V. Cabra, M. Samsó, *J. Vis. Exp.* **2015**.

[10] B. Michen, C. Geers, D. Vanhecke, C. Endes, B. Rothen-Rutishauser, S. Balog, A. Petri-Fink, *Sci. Rep.* **2015**.

[11] E. Firlar, M. Ouy, L. Covnot, Y. Xing, D. Lee, A. Chan, Y. He, B. Song, S. Afelik, Y. Wang, R. Shahbazian-Yassar, J. Oberholzer, T. Shokuhfar, *Int. J. Nanomedicine* **2019**, *Volume 14*, 371.

[12] S. Narayanan, E. Firlar, M. G. Rasul, T. Foroozan, N. Farajpour, L. Covnot, R. Shahbazian-Yassar, T. Shokuhfar, *Nanoscale* **2019**, *11*, 16868.

[13] M. H. Nielsen, S. Aloni, J. J. De Yoreo, *Science (80-.).* **2013**, *218*, 213.

[14] S. Narayanan, E. Firlar, R. Shahbazian-Yassar, T. Shokuhfar, *Microsc. Microanal.* **n.d.**

[15] Q. Chen, J. M. Smith, J. Park, K. Kim, D. Ho, H. I. Rasool, A. Zettl, A. P. Alivisatos, *Nano Lett.* **2013**, *13*, 4556.

[16] K. He, A. Nie, Y. Yuan, S. M. Ghodsi, B. Song, E. Firlar, J. Lu, Y. Lu, T. Shokuhfar, C. M. Megaridis, R. Shahbazian-Yassar, *ACS Appl. Nano Mater.* **2018**.

[17] E. Kennedy, E. M. Nelson, T. Tanaka, J. Damiano, G. Timp, *ACS Nano* **2016**, *10*, 2669.

[18] L. Morton, *Bull. Cl. Sci. Acad R. Belg* **1935**, *21*.

[19] D. F. Parsons, *Science (80-.).* **1974**.

[20] J. Dubochet, A. W. McDowall, *J. Microsc.* **1981**.

[21] M. A. Herzik, M. Wu, G. C. Lander, *Nat. Commun.* **2019**.

[22] K. L. Liu, C. C. Wu, Y. J. Huang, H. L. Peng, H. Y. Chang, P. Chang, L. Hsu, T. R. Yew, *Lab Chip* **2008**.

[23] N. De Jonge, D. B. Peckys, G. J. Kremers, D. W. Piston, *Proc. Natl. Acad. Sci. U. S. A.* **2009**.

[24] T. J. Woehl, S. Kashyap, E. Firlar, T. Perez-Gonzalez, D. Faivre, D. Trubitsyn, D. A. Bazylinski, T. Prozorov, *Sci. Rep.* **2014**, *4*, 6854.

[25] M. J. Williamson, R. M. Tromp, P. M. Vereecken, R. Hull, F. M. Ross, *Nat. Mater.* **2003**.

[26] E. Firlar, M. Ouy, A. Bogdanowicz, L. Covnot, B. Song, Y. Nadkarni, R. Shahbazian-Yassar, T. Shokuhfar, *Nanoscale* **2019**, *11*, 698.

[27] E. Kennedy, E. M. Nelson, J. Damiano, G. Timp, *ACS Nano* **2017**, *11*, 3.
[28] N. M. Schneider, M. M. Norton, B. J. Mendel, J. M. Grogan, F. M. Ross, H. H. Bau, *J. Phys. Chem. C* **2014**, *118*, 22373.
[29] M. E. Holtz, Y. Yu, J. Gao, H. D. Abruña, D. A. Muller, in *Microsc. Microanal.*, **2013**.
[30] R. F. Egerton, *Microsc. Res. Tech.* **2012**, *75*, 1550.
[31] J. M. Yuk, J. Park, P. Ercius, K. Kim, D. J. Hellebusch, M. F. Crommie, J. Y. Lee, A. Zettl, A. P. Alivisatos, J. C. Meyer, C. O. Girit, M. F. Crommie, A. Zettl, C.-Y. Wen, V. Radmilovic, A. H. Zewail, N. de Jonge, F. M. Ross, M. J. Williamson, R. M. Tromp, P. M. Vereecken, R. Hull, F. M. Ross, H. Zheng, J. E. Evans, K. L. Jungjohann, N. D. Browning, I. Arslan, K. S. Novoselov, X. Li, J. N. Coleman, Z. Lee, A. Kolmakov, Y. A. Wu, J. C. Meyer, C. O. Girit, M. F. Crommie, A. Zettl, R. Erni, R. R. Nair, J. M. Yuk, K. Xu, P. Cao, J. R. Heath, X. Li, W. Regan, X. Xie, S. P. Koenig, N. G. Boddeti, M. L. Dunn, J. S. Bunch, J. C. Meyer, E. A. Stach, H. Zheng, S. A. Claridge, A. M. Minor, A. P. Alivisatos, U. Dahmen, X. Lu, M. Rycenga, S. E. Skrabalak, B. Wiley, Y. Xia, K. J. M. Bishop, C. E. Wilmer, S. Soh, B. A. Grzybowski, X. Lu, M. S. Yavuz, H.-Y. Tuan, B. A. Korgel, Y. Xia, P. Schapotschnikow, R. Pool, T. J. H. Vlugt, Z. Z. Fang, H. Wang, *Science* **2012**, *336*, 61.
[32] E. Khestanova, F. Guinea, L. Fumagalli, A. K. Geim, I. V. Grigorieva, *Nat. Commun.* **2016**, *7*, 12587.
[33] K. S. Vasu, E. Prestat, J. Abraham, J. DIx, R. J. Kashtiban, J. Beheshtian, J. Sloan, P. Carbone, M. Neek-Amal, S. J. Haigh, A. K. Geim, R. R. Nair, *Nat. Commun.* **2016**.
[34] M. Textor, N. De Jonge, *Nano Lett.* **2018**, *18*, 3313.
[35] V. Berry, *Carbon N. Y.* **2013**, *62*, 1.
[36] C. Wang, Q. Qiao, T. Shokuhfar, R. F. Klie, *Adv. Mater.* **2014**, *26*, 3410.
[37] H. Cho, M. R. Jones, S. C. Nguyen, M. R. Hauwiller, A. Zettl, A. P. Alivisatos, *Nano Lett.* **2017**, *17*, 414.
[38] J. M. Grogan, N. M. Schneider, F. M. Ross, H. H. Bau, *Nano Lett.* **2014**, *14*, 359.
[39] K. Kovářová, A. J. B. Zehnder, T. Egli, *J. Bacteriol.* **1996**.
[40] S. M. Ghodsi, C. M. Megaridis, R. Shahbazian-Yassar, T. Shokuhfar, *Small Methods* **2019**, *3*, 453001.
[41] D. Su, *Green Energy Environ.* **2017**.
[42] E. A. Lewis, H. Downie, R. F. Collins, E. Prestat, J. R. Lloyd, S. J. Haigh, *Part. Part. Syst. Charact.* **2016**.
[43] N. Mohanty, M. Fahrenholtz, A. Nagaraja, D. Boyle, V. Berry, *Nano Lett.* **2011**, *11*, 1270.
[44] P. Stiefel, S. Schmidt-Emrich, K. Maniura-Weber, Q. Ren, *BMC Microbiol.* **2015**, *15*.
[45] M. A. Kohanski, D. J. Dwyer, J. J. Collins, *Nat. Rev. Microbiol.* **2010**, *8*, 423.
[46] T. W. Huang, S. Y. Liu, Y. J. Chuang, H. Y. Hsieh, C. Y. Tsai, Y. T. Huang, U. Mirsaidov, P. Matsudaira, F. G. Tseng, C. S. Chang, F. R. Chen, *Lab Chip* **2012**.
[47] D. B. Peckys, G. M. Veith, D. C. Joy, N. de Jonge, *PLoS One* **2009**.
[48] E. Bi, J. Lutkenhaus, *Nature* **1991**.
[49] Y.-L. Shih, L. Rothfield, *Microbiol. Mol. Biol. Rev.* **2006**, *70*, 729.
[50] S. Wang, H. Arellano-Santoyo, P. A. Combs, J. W. Shaevitz, *Proc. Natl. Acad. Sci.* **2010**, *107*, 9182.
[51] S. Povea-Cabello, M. Oropesa-Ávila, P. de la Cruz-Ojeda, M. Villanueva-Paz, M. De La Mata, J. M. Suárez-Rivero, M. Álvarez-Córdoba, I. Villalón-García, D. Cotán, P. Ybot-González, J. A. Sánchez-Alcázar, *Int. J. Mol. Sci.* **2017**.

[52] Y. Wang, X. Chen, H. Cao, C. Deng, X. Cao, P. Wang, *J. Anal. Methods Chem.* **2015**, *2015*, 829302.
[53] T. H. Moser, H. Mehta, C. Park, R. T. Kelly, T. Shokuhfar, J. E. Evans, *Sci. Adv.* **2018**.
[54] T. H. Moser, T. Shokuhfar, J. E. Evans, *Micron* **2019**.
[55] E. Firlar, T. Perez-Gonzalez, A. Olszewska, D. Faivre, T. Prozorov, *J. Mater. Res.* **2016**.
[56] W. J. Dearnaley, B. Schleupner, A. C. Varano, N. A. Alden, F. Gonzalez, M. A. Casasanta, B. E. Scharf, M. J. Dukes, D. F. Kelly, *Nano Lett.* **2019**, *19*, 6734.
[57] T. Prozorov, T. P. Almeida, A. Kovács, R. E. Dunin-Borkowski, *J. R. Soc. Interface* **2017**.
[58] M. Lehmann, H. Lichte, *Microsc. Microanal.* **2002**.
[59] E. Firlar, M. Ouy, A. Bogdanowicz, L. Covnot, B. Song, Y. Nadkarni, R. Shahbazian-Yassar, T. Shokuhfar, *Nanoscale* **2019**, *11*, 698.
[60] W. H. Massover, J. M. Cowley, *Proc. Natl. Acad. Sci. U. S. A.* **1973**.
[61] J. E. Evans, K. L. Jungjohann, P. C. K. Wong, P. L. Chiu, G. H. Dutrow, I. Arslan, N. D. Browning, *Micron* **2012**.
[62] S. Kashyap, T. J. Woehl, X. Liu, S. K. Mallapragada, T. Prozorov, *ACS Nano* **2014**.
[63] V. Tullio, S. Roberta, P. Manuela, in *Hum. Mosq. Lysozymes Old Mol. New Approaches Against Malar.*, **2015**.
[64] T. Yamazaki, Y. Kimura, P. G. Vekilov, E. Furukawa, M. Shirai, H. Matsumoto, A. E. S. Van Driessche, K. Tsukamoto, *Proc. Natl. Acad. Sci. U. S. A.* **2017**.
[65] M. De Andrea, R. Ravera, D. Gioia, M. Gariglio, S. Landolfo, *Eur. J. Paediatr. Neurol.* **2002**.
[66] L. M. DiMemmo, A. Cameron Varano, J. Haulenbeek, Y. Liang, K. Patel, M. J. Dukes, S. Zheng, M. Hubert, S. P. Piccoli, D. F. Kelly, *Lab Chip* **2017**.
[67] S. Keskin, N. De Jonge, *Nano Lett.* **2018**.
[68] R. E. Stephens, K. T. Edds, *Physiol. Rev.* **1976**.
[69] J. Cope, S. Gilbert, I. Rayment, D. Mastronarde, A. Hoenger, *J. Struct. Biol.* **2010**.
[70] A. Teimoori, H. Soleimanjahi, M. Makvandi, *Jundishapur J. Microbiol.* **2014**.
[71] A. Cameron Varano, A. Rahimi, M. J. Dukes, S. Poelzing, S. M. McDonald, D. F. Kelly, *Chem. Commun.* **2015**.
[72] N. De Jonge, D. B. Peckys, *ACS Nano* **2016**, *10*, 9061.
[73] D. B. Peckys, N. De Jonge, *Nano Lett.* **2011**.
[74] D. B. Peckys, P. Mazur, K. L. Gould, N. De Jonge, *Biophys. J.* **2011**.
[75] E. S. Pohlmann, K. Patel, S. Guo, M. J. Dukes, Z. Sheng, D. F. Kelly, *Nano Lett.* **2015**.
[76] I. N. Dahmke, A. Verch, J. Hermannsdörfer, D. B. Peckys, R. S. Weatherup, S. Hofmann, N. De Jonge, *ACS Nano* **2017**.
[77] D. B. Peckys, U. Korf, S. Wiemann, N. De Jonge, *Mol. Biol. Cell* **2017**.
[78] D. B. Peckys, D. Hirsch, T. Gaiser, N. De Jonge, *Mol. Med.* **2019**, *25*.
[79] D. Stoyan, H. Stoyan, *Biometrical J.* **1996**.
[80] S. Feske, Y. Gwack, M. Prakriya, S. Srikanth, S. H. Puppel, B. Tanasa, P. G. Hogan, R. S. Lewis, M. Daly, A. Rao, *Nature* **2006**.
[81] P. Li, Y. Miao, A. Dani, M. Vig, *Mol. Biol. Cell* **2016**.
[82] X. Hou, S. R. Burstein, S. B. Long, *Elife* **2018**.
[83] D. Alansary, D. B. Peckys, B. A. Niemeyer, N. de Jonge, *J. Cell Sci.* **2020**, *133*.
[84] S. Keskin, S. Besztejan, G. Kassier, S. Manz, R. Bücker, S. Riekeberg, H. K. Trieu, A. Rentmeister, R. J. D. Miller, *J. Phys. Chem. Lett.* **2015**.
[85] J. J. De Yoreo, P. U. P. A. Gilbert, N. A. J. M. Sommerdijk, R. L. Penn, S. Whitelam, D.

Joester, H. Zhang, J. D. Rimer, A. Navrotsky, J. F. Banfield, A. F. Wallace, F. M. Michel, F. C. Meldrum, H. Cölfen, P. M. Dove, *Science (80-.).* **2015**, *349*, 498.
[86] N. K. Dhami, M. S. Reddy, M. S. Mukherjee, *Front. Microbiol.* **2013**.
[87] F. S. Murakami, P. O. Rodrigues, C. M. T. De Campos, M. A. S. Silva, *Cienc. e Tecnol. Aliment.* **2007**.
[88] U. Ripamonti, *J. Bone Jt. Surg. - Ser. A* **1991**.
[89] T. H. J. Florin, G. Neale, S. Goretski, J. H. Cummings, *J. Food Compos. Anal.* **1993**.
[90] R. Wu, C. E. Boyd, *Progress. Fish-Culturist* **1990**.
[91] J. B. Thompson, F. G. Ferris, *Geology* **1990**.
[92] C. Wang, T. Shokuhfar, R. F. Klie, *Adv. Mater.* **2016**, *28*, 7716.
[93] M. Maestri, E. Iglesia, *Phys. Chem. Chem. Phys.* **2018**, *20*, 15725.
[94] N. Artioli, R. F. Lobo, E. Iglesia, *J. Phys. Chem. C* **2013**, *117*, 20666.
[95] R. Kröger, A. Verch, R. Kröger, A. Verch, *Minerals* **2018**, *8*, 21.
[96] J. V. McArthur, R. C. Tuckfield, C. Baker-Austin, Springer, Berlin, Heidelberg, **2012**, pp. 135–152.
[97] W. Witte, *Science (80-.).* **1998**, *379*, 996.
[98] D. M. Livermore, D. F. Brown, *J. Antimicrob. Chemother.* **2001**, *48*, 59.
[99] J. Davies, *Microbiologia* **1996**, *74*, 417.
[100] W. C Reygaert, *AIMS Microbiol.* **2018**, *4*, 482.
[101] B. Kepplinger, S. Morton-Laing, K. H. Seistrup, E. C. L. Marrs, A. P. Hopkins, J. D. Perry, H. Strahl, M. J. Hall, J. Errington, N. E. Ellis Allenby, *ACS Chem. Biol.* **2018**, *13*, 207.
[102] M. M. Cadelis, E. I. W. Pike, W. Kang, Z. Wu, M. L. Bourguet-Kondracki, M. Blanchet, N. Vidal, J. M. Brunel, B. R. Copp, *Eur. J. Med. Chem.* **2019**, *183*, 111708.
[103] G. Cox, G. D. Wright, *Int. J. Med. Microbiol.* **2013**, *303*, 287.
[104] S. T. Chancey, D. Zähner, D. S. Stephens, *Future Microbiol.* **2012**, *7*, 959.
[105] R. M. Epand, C. Walker, R. F. Epand, N. A. Magarvey, *Biochim. Biophys. Acta - Biomembr.* **2016**, *1858*, 980.
[106] J. M. Pagès, C. E. James, M. Winterhalter, *Nat. Rev. Microbiol.* **2008**, *6*, 893.
[107] P. A. Lambert, *J. Appl. Microbiol. Symp. Suppl.* **2002**, *92*, 46S.
[108] N. Q. Balaban, J. Liu, in *Persister Cells Infect. Dis.*, Springer International Publishing, Cham, **2019**, pp. 1–17.
[109] P. Durão, R. Balbontín, I. Gordo, *Trends Microbiol.* **2018**, *26*, 677.
[110] M. Silindir, A. Y. Özer, *Fabad J. Pharm. Sci.* **2009**, *34*, 43.
[111] M. Alavi, M. Rai, *Expert Rev. Anti. Infect. Ther.* **2019**, *17*, 419.
[112] M. Alavi, N. Karimi, T. Valadbeigi, *ACS Biomater. Sci. Eng.* **2019**, *5*, 4228.
[113] M. Alavi, M. Rai, *Appl. Microbiol. Biotechnol.* **2019**, *103*, 8669.
[114] M. Alavi, A. Nokhodchi, *Carbohydr. Polym.* **2020**, *227*, 115349.
[115] A. Panáček, L. Kvítek, M. Smékalová, R. Večeřová, M. Kolář, M. Röderová, F. Dyčka, M. Šebela, R. Prucek, O. Tomanec, R. Zbořil, *Nat. Nanotechnol.* **2018**, *13*, 65.
[116] C. P. Randall, A. Gupta, N. Jackson, D. Busse, A. J. O'Neill, *J. Antimicrob. Chemother.* **2015**, *70*, 1073.
[117] N. R. Panyala, E. M. Peña-Méndez, J. Havel, *J. Appl. Biomed.* **2008**, *6*, 117.
[118] S. Kim, J. E. Choi, J. Choi, K. H. Chung, K. Park, J. Yi, D. Y. Ryu, *Toxicol. Vitr.* **2009**, *23*, 1076.
[119] T. J. Silhavy, D. Kahne, S. Walker, *Cold Spring Harb. Perspect. Biol.* **2010**, *2*, a000414.

[120] M. Michalska, F. Gambacorta, R. Divan, I. S. Aranson, A. Sokolov, P. Noirot, P. D. Laible, *Nanoscale* **2018**, *10*, 6639.
[121] F. Xue, J. Liu, L. Guo, L. Zhang, Q. Li, *J. Theor. Biol.* **2015**, *385*, 1.
[122] M. Ayazi, N. Golshan Ebrahimi, E. Jafari Nodoushan, *Int. J. Adhes. Adhes.* **2019**, *88*, 66.
[123] X. Li, *Phys. Chem. Chem. Phys.* **2015**, *18*, 1311.
[124] Y. H. An, R. J. Friedman, *J. Biomed. Mater. Res.* **1998**, *43*, 338.
[125] T. J. Foster, J. A. Geoghegan, V. K. Ganesh, M. Höök, *Nat. Rev. Microbiol.* **2014**, *12*, 49.
[126] A. Elbourne, J. Chapman, A. Gelmi, D. Cozzolino, R. J. Crawford, V. K. Truong, *J. Colloid Interface Sci.* **2019**, *546*, 192.
[127] R. M. Goulter, I. R. Gentle, G. A. Dykes, *Lett. Appl. Microbiol.* **2009**, *49*, 1.
[128] H. H. Tuson, D. B. Weibel, *Soft Matter* **2013**, *9*, 4368.
[129] M. Köller, N. Ziegler, C. Sengstock, T. A. Schildhauer, A. Ludwig, *Biomed. Phys. Eng. Express* **2018**, *4*, 055002.
[130] M. S. Son, R. K. Taylor, *Curr. Protoc. Microbiol.* **2012**, *Chapter 5*.
[131] G. Sezonov, D. Joseleau-Petit, R. D'Ari, *J. Bacteriol.* **2007**, *189*, 8746.
[132] J. Monod, *Annu. Rev. Microbiol.* **1949**, *3*, 371.
[133] Q. L. Feng, J. Wu, G. Q. Chen, F. Z. Cui, T. N. Kim, J. O. Kim, *J. Biomed. Mater. Res.* **2000**, *52*, 662.
[134] M. Winey, J. B. Meehl, E. T. O'Toole, T. H. Giddings, *Mol. Biol. Cell* **2014**, *25*, 319.
[135] L. Zhang, Y. Jiang, Y. Ding, N. Daskalakis, L. Jeuken, M. Povey, A. J. O'Neill, D. W. York, *J. Nanoparticle Res.* **2010**.
[136] S. Prabhu, E. K. Poulose, *Int. Nano Lett.* **2012**, DOI 10.1186/2228-5326-2-32.
[137] G. K. Auer, D. B. Weibel, *Biochemistry* **2017**, *56*, 3710.
[138] Z. D. Blount, *Elife* **2015**, *4*, e05826.
[139] I. M. Keseler, J. Collado-Vides, S. Gama-Castro, J. Ingraham, S. Paley, I. T. Paulsen, M. Peralta-Gil, P. D. Karp, *Nucleic Acids Res.* **2005**, *33*, D334.
[140] H. K. Makadia, S. J. Siegel, *Polymers (Basel).* **2011**, *3*, 1377.
[141] J. M. Anderson, M. S. Shive, *Adv. Drug Deliv. Rev.* **1997**, *28*, 5.
[142] R. S. Breed, W. D. Dotterrer, *J. Bacteriol.* **1916**, *1*, 321.
[143] J. C. F. de Winter, *Pract. Assessment, Res. Eval.* **2013**, *18*, 1.
[144] C. N. Lok, C. M. Ho, R. Chen, Q. Y. He, W. Y. Yu, H. Sun, P. K. H. Tam, J. F. Chiu, C. M. Che, *J. Biol. Inorg. Chem.* **2007**, *12*, 527.
[145] M. S. Islam, A. Aryasomayajula, P. R. Selvaganapathy, *Micromachines* **2017**, *8*, 83.
[146] M. Beeby, J. C. Gumbart, B. Roux, G. J. Jensen, *Mol. Microbiol.* **2013**, *88*, 664.
[147] L. Gan, S. Chen, G. J. Jensen, *Proc. Natl. Acad. Sci.* **2008**, *105*, 18953.
[148] H. H. Tuson, G. K. Auer, L. D. Renner, M. Hasebe, C. Tropini, M. Salick, W. C. Crone, A. Gopinathan, K. C. Huang, D. B. Weibel, *Mol. Microbiol.* **2012**, *84*, 874.
[149] P. Loskill, P. M. Pereira, P. Jung, M. Bischoff, M. Herrmann, M. G. Pinho, K. Jacobs, *Biophys. J.* **2014**, *107*, 1082.
[150] W. Vollmer, in *The Periplasm*, **2007**, pp. 198–213.
[151] J. van Heijenoort, *Glycobiology* **2001**, *11*, 25R.
[152] W. Vollmer, U. Bertsche, *Biochim. Biophys. Acta - Biomembr.* **2008**, *1778*, 1714.
[153] B. Glauner, J. V. Holtje, U. Schwarz, *J. Biol. Chem.* **1988**, *263*, 10088.
[154] M. A. Snowden, H. R. Perkins, *Eur. J. Biochem.* **1990**, *191*, 373.
[155] S. Magnet, L. Dubost, A. Marie, M. Arthur, L. Gutmann, *J. Bacteriol.* **2008**, *190*, 4782.
[156] F. Si, B. Li, W. Margolin, S. X. Sun, *Sci. Rep.* **2015**, *5*, 11377.

[157] W. P. Hartl, H. Klapper, B. Barbier, H. J. Ensikat, R. Dronskowski, P. Müller, G. Ostendorp, A. Tye, R. Bauer, W. Barthlott, *Can. J. Bot.* **2007**, *85*, 501.
[158] J. A. Raven, H. Griffiths, S. M. Glidewell, T. Preston, *Proc. R. Soc. London. Ser. B. Biol. Sci.* **1982**, *216*, 87.
[159] P. J. White, M. R. Broadley, *Ann. Bot.* **2003**, *92*, 487.
[160] M. A. Webb, *Plant Cell* **1999**, *11*, 751.
[161] V. R. Franceschi, P. A. Nakata, *Annu. Rev. Plant Biol.* **2005**, *56*, 47.
[162] L. A. J. Garvie, *Naturwissenschaften* **2006**, *93*, 114.
[163] A. Morita, O. Yanagisawa, S. Takatsu, S. Maeda, S. Hiradate, *Phytochemistry* **2008**, *69*, 147.
[164] G. Martin, M. Guggiari, D. Bravo, J. Zopfi, G. Cailleau, M. Aragno, D. Job, E. Verrecchia, P. Junier, *Environ. Microbiol.* **2012**, *14*, 2960.
[165] P. R. Ryan, E. Delhaize, D. L. Jones, *Annu. Rev. Physiol. Plant Mol. Biol.* **2001**, *52*, 527.
[166] A. A. . Gorbushina, W. E. . Krumbein, M. . Volkmann, *Astrobiology* **2002**, *2*, 203.
[167] F. L. Coe, A. Evan, E. Worcester, *J. Clin. Invest.* **2005**, *115*, 2598.
[168] T. Umekawa, Y. Hatanaka, T. Kurita, S. R. Khan, *J. Am. Soc. Nephrol.* **2004**, *15*, 635.
[169] F. Grases, A. Costa-Bauzá, M. Ramis, V. Montesinos, A. Conte, *Scand. J. Urol. Nephrol.* **2003**, *37*, 482.
[170] A. Trinchieri, F. Ostini, R. Nespoli, F. Rovera, E. Montanari, G. Zanetti, *J. Urol.* **1999**, *162*, 27.
[171] J. M. Soucie, M. J. Thun, R. J. Coates, W. McClellan, H. Austin, *Kidney Int.* **1994**, *46*, 893.
[172] F. Grases, A. Millan, A. Conte, *Urol. Res.* **1990**, *18*, 17.
[173] X. Sheng, *J. Am. Soc. Nephrol.* **2005**, *16*, 1904.
[174] W. Heijnen, W. Jellinghaus, W. E. Klee, *Urol. Res.* **1985**, *13*, 281.
[175] J. Ihli, Y.-W. Wang, B. Cantaert, Y.-Y. Kim, D. C. Green, P. H. H. Bomans, N. A. J. M. Sommerdijk, F. C. Meldrum, *Chem. Mater.* **2015**, *27*, 3999.
[176] A. Gehl, M. Dietzsch, M. Mondeshki, S. Bach, T. Häger, M. Panthöfer, B. Barton, U. Kolb, W. Tremel, *Chem. - Eur. J.* **2015**, *21*, 18192.
[177] M. Hajir, R. Graf, W. Tremel, *Chem. Commun.* **2014**, *50*, 6534.
[178] J. P. Kavanagh, L. Jones, P. N. Rao, *Clin. Sci. (Lond).* **2000**, *98*, 151.
[179] J. P. Kavanagh, L. Jones, P. N. Rao, *Urol. Res.* **1999**, *27*, 231.
[180] J. P. Kavanagh, in *Urol. Res.*, **2006**, pp. 139–145.
[181] E. Weber, A. Verch, D. Levy, A. N. Fitch, B. Pokroy, *ChemistrySelect* **2016**, *2*, 132.
[182] A. Shebanova, T. Ismagulova, A. Solovchenko, O. Baulina, E. Lobakova, A. Ivanova, A. Moiseenko, K. Shaitan, V. Polshakov, L. Nedbal, O. Gorelova, *Protoplasma* **2017**, *254*, 1323.
[183] J. C. Lieske, H. Swift, T. Martin, B. Patterson, F. G. Toback, *Proc. Natl. Acad. Sci. U. S. A.* **1994**, *91*, 6987.
[184] E. Ruiz-Agudo, A. Burgos-Cara, C. Ruiz-Agudo, A. Ibañez-Velasco, H. Cölfen, C. Rodriguez-Navarro, *Nat. Commun.* **2017**, *8*, 1.
[185] E. Weber, D. Levy, M. Ben Sasson, A. N. Fitch, B. Pokroy, *RSC Adv.* **2015**, *5*, 98626.
[186] D. J. Kok, S. E. Papapoulos, L. J. M. Blomen, O. L. M. Bijvoet, *Kidney Int.* **1988**, *34*, 346.
[187] M. L. Weaver, S. R. Qiu, J. R. Hoyer, W. H. Casey, G. H. Nancollas, J. J. De Yoreo, *J. Cryst. Growth* **2007**, *306*, 135.
[188] L. Wang, J. J. De Yoreo, X. Guan, S. R. Qiu, J. R. Hoyer, G. H. Nancollas, *Cryst. Growth*

Des. **2006**, *6*, 1769.
[189] J. Chung, I. Granja, M. G. Taylor, G. Mpourmpakis, J. R. Asplin, J. D. Rimer, *Nature* **2016**, *536*, 446.
[190] J. D. Rimer, Z. An, Z. Zhu, M. H. Lee, D. S. Goldfarb, J. A. Wesson, M. D. Ward, *Science (80-.).* **2010**, *330*, 337.
[191] J. Tersoff, R. M. Tromp, *Phys. Rev. Lett.* **1993**, *70*, 2782.
[192] S. R. Qiu, A. Wierzbicki, E. A. Salter, S. Zepeda, C. A. Orme, J. R. Hoyer, G. H. Nancollas, A. M. Cody, J. J. De Yoreo, *J. Am. Chem. Soc.* **2005**, *127*, 9036.
[193] R. W. Friddle, M. L. Weaver, S. R. Qiu, A. Wierzbicki, W. H. Casey, J. J. De Yoreo, *Proc. Natl. Acad. Sci. U. S. A.* **2010**, *107*, 11.
[194] K. R. Cho, E. A. Salter, J. J. De Yoreo, A. Wierzbicki, S. Elhadj, Y. Huang, S. R. Qiu, *CrystEngComm* **2013**, *15*, 54.
[195] T. Jung, X. Sheng, C. K. Choi, W. S. Kim, J. A. Wesson, M. D. Ward, *Langmuir* **2004**, *20*, 8587.
[196] S. Guo, M. D. Ward, J. A. Wesson, *Langmuir* **2002**, *18*, 4284.
[197] C. Wang, T. Shokuhfar, R. F. Klie, *Adv. Mater.* **2016**, *28*, 7716.
[198] D. J. Kelly, M. Zhou, N. Clark, M. J. Hamer, E. A. Lewis, A. M. Rakowski, S. J. Haigh, R. V. Gorbachev, *Nano Lett.* **2018**, *18*, 1168.
[199] T. Solomon, *J. Chem. Educ.* **2001**, *78*, 1691.
[200] J. C. Phillips, R. Braun, W. Wang, J. Gumbart, E. Tajkhorshid, E. Villa, C. Chipot, R. D. Skeel, L. Kale, K. Schulten, *J. Comput. Chem.* **2005**, *26*, 1781.
[201] W. L. Jorgensen, J. Chandrasekhar, J. D. Madura, R. W. Impey, M. L. Klein, *J. Chem. Phys.* **1983**, *79*, 926.
[202] D. Beglov, B. Roux, *J. Chem. Phys.* **1994**, *100*, 9050.
[203] D. J. Drisch, M. J.; Trucks, G. W.; Schlegel, H. B.; Scuseria, G. E.; Robb, M. A.; Cheeseman, J. R.; Scalmani, G.; Barone, V.; Mennucci, B.; Petersson, G. A.; Nakatsuji, H.; Caricato, M.; Li, X.; Hratchian, H. P.; Izmaylov, A. F.; Bloino, J.; Zheng, G.; Sonnenb, **2013**.
[204] C. G. Mayne, J. Saam, K. Schulten, E. Tajkhorshid, J. C. Gumbart, *J. Comput. Chem.* **2013**, *34*, 2757.
[205] T. Darden, D. York, L. Pedersen, *J. Chem. Phys.* **1993**, *98*, 10089.
[206] D. N. Petsev, K. Chen, O. Gliko, P. G. Vekilov, *Proc. Nat. Acad. Sci. USA* **2003**, *100*, 792.
[207] R. Demichelis, P. Raiteri, J. D. Gale, D. Quigley, D. Gebauer, *Nat. Commun.* **2011**, *2*.
[208] J. L. Zryd, W. R. Burghardt, *J. Appl. Polym. Sci.* **1995**, *57*, 1525.
[209] Q. Hu, M. H. Nielsen, C. L. Freeman, L. M. Hamm, J. Tao, J. R. I. Lee, T. Y. J. Han, U. Becker, J. H. Harding, P. M. Dove, J. J. De Yoreo, *Faraday Discuss.* **2012**, *159*, 509.
[210] A. Navrotsky, *Proc. Natl. Acad. Sci.* **2004**, *101*, 12096.
[211] X. Sheng, T. Jung, J. a Wesson, M. D. Ward, *Proc. Natl. Acad. Sci. U. S. A.* **2005**, *102*, 267.
[212] W. P. Hartl, H. Klapper, B. Barbier, H. J. Ensikat, R. Dronskowski, P. Müller, G. Ostendorp, A. Tye, R. Bauer, W. Barthlott, *Can. J. Bot.* **2007**, *85*, 501.
[213] J. W. Mullin, in *Crystallization*, **2001**.
[214] T. Sugimoto, *Monodispersed Particles*, Elsevier, **2001**.
[215] J. Chung, I. Granja, M. G. Taylor, G. Mpourmpakis, J. R. Asplin, J. D. Rimer, *Nature* **2016**, *536*, 446.

[216] D. J. Kok, S. E. Papapoulos, L. J. M. J. Blomen, O. L. M. Bijvoet, *Kidney Int.* **1988**, *34*, 346.
[217] E. Lopez-Fontal, A. Grochmal, T. Foran, L. Milanesi, S. Tomas, *Chem. Sci.* **2018**, *9*, 1705.
[218] W. Zhao, B. Xia, L. Lin, X. Xiao, P. Liu, X. Lin, H. Peng, Y. Zhu, R. Yu, P. Lei, J. Wang, L. Zhang, Y. Xu, M. Zhao, L. Peng, Q. Li, W. Duan, Z. Liu, S. Fan, K. Jiang, *Sci. Adv.* **2017**, *3*, e1603231.
[219] J. Li, X. Y. Wang, X. R. Liu, Z. Jin, D. Wang, L. J. Wan, *J. Mater. Chem. C* **2015**, *3*, 3503.
[220] V. Tszzorl, C. Dotvtbnecgbrrt, *Am. Mineral.* **1980**, *65*, 27.
[221] V. Tszzorl, C. Dotvtbnecgbrrt, *Am. Mineral.* **1980**.
[222] G. Grass, C. Rensing, M. Solioz, *Appl. Environ. Microbiol.* **2011**, DOI 10.1128/AEM.02766-10.
[223] B. A. Camacho-Flores, O. Martínez-Álvarez, M. C. Arenas-Arrocena, R. Garcia-Contreras, L. Argueta-Figueroa, J. De La Fuente-Hernández, L. S. Acosta-Torres, *J. Nanomater.* **2015**, DOI 10.1155/2015/415238.
[224] L. Actis, A. Srinivasan, J. L. Lopez-Ribot, A. K. Ramasubramanian, J. L. Ong, *J. Mater. Sci. Mater. Med.* **2015**, DOI 10.1007/s10856-015-5538-8.
[225] S. Pal, Y. K. Tak, J. M. Song, *Appl. Environ. Microbiol.* **2007**, DOI 10.1128/AEM.02218-06.
[226] Y. N. Slavin, J. Asnis, U. O. Häfeli, H. Bach, *J. Nanobiotechnology* **2017**, DOI 10.1186/s12951-017-0308-z.
[227] A. Różżańska, A. Chmielarczyk, D. Romaniszyn, A. Sroka-Oleksiak, M. Bulanda, M. Walkowicz, P. Osuch, T. Knych, *Int. J. Environ. Res. Public Health* **2017**, DOI 10.3390/ijerph14070813.
[228] J. R. Morones, J. L. Elechiguerra, A. Camacho, K. Holt, J. B. Kouri, J. T. Ramírez, M. J. Yacaman, *Nanotechnology* **2005**, DOI 10.1088/0957-4484/16/10/059.
[229] D. Acharya, K. M. Singha, P. Pandey, B. Mohanta, J. Rajkumari, L. P. Singha, *Sci. Rep.* **2018**, DOI 10.1038/s41598-017-18590-6.
[230] J. Y. Cheon, S. J. Kim, Y. H. Rhee, O. H. Kwon, W. H. Park, *Int. J. Nanomedicine* **2019**, DOI 10.2147/IJN.S196472.
[231] H. Liang, W. Wang, Y. Huang, S. Zhang, H. Wei, H. Xu, *J. Phys. Chem. C* **2010**, DOI 10.1021/jp9105713.
[232] H. Liang, Z. P. Li, W. Wang, Y. Wu, H. Xu, *Adv. Mater.* **2009**, DOI 10.1002/adma.200901139.
[233] Y. Sun, Y. Xia, *Science (80-.).* **2002**, DOI 10.1126/science.1077229.
[234] X. Dong, X. Ji, J. Jing, M. Li, J. Li, W. Yang, *J. Phys. Chem. C* **2010**, DOI 10.1021/jp909964k.
[235] J. Ehreth, in *Vaccine*, **2003**.
[236] P. A. Lachenbruch, *Control. Clin. Trials* **1998**, DOI 10.1016/S0197-2456(98)00042-7.
[237] S. F. Ahmed, A. A. Quadeer, M. R. McKay, *Viruses* **2020**, DOI 10.1101/2020.02.03.933226.
[238] Novel Coronavirus Pneumonia Emergency Response Epidemiology Team, *Zhonghua Liu Xing Bing Xue Za Zhi* **2020**, DOI 10.3760/cma.j.issn.0254-6450.2020.02.003.
[239] R. G. Webster, *Lancet* **2004**, DOI 10.1016/S0140-6736(03)15329-9.
[240] M. H. V. Van Regenmortel, B. W. J. Mahy, *Emerg. Infect. Dis.* **2004**, DOI

10.3201/eid1001.030279.
[241] E. De Clercq, G. Li, *Clin. Microbiol. Rev.* **2016**, DOI 10.1128/CMR.00102-15.
[242] S. L. Warnes, Z. R. Little, C. W. Keevil, *MBio* **2015**, DOI 10.1128/mBio.01697-15.
[243] J. J. Broglie, B. Alston, C. Yang, L. Ma, A. F. Adcock, W. Chen, L. Yang, *PLoS One* **2015**, DOI 10.1371/journal.pone.0141050.
[244] Q. M. Liu, T. Yasunami, K. Kuruda, M. Okido, *Trans. Nonferrous Met. Soc. China (English Ed.* **2012**, DOI 10.1016/S1003-6326(11)61449-0.
[245] M. Sampath, R. Vijayan, E. Tamilarasu, A. Tamilselvan, B. Sengottuvelan, *J. Nanotechnol.* **2014**, DOI 10.1155/2014/626523.
[246] M. J. Woźniak-Budych, K. Langer, B. Peplińska, Ł. Przysiecka, M. Jarek, M. Jarzębski, S. Jurga, *Mater. Chem. Phys.* **2016**, DOI 10.1016/j.matchemphys.2016.05.036.
[247] L. Van Der Hoek, *Antivir. Ther.* **2007**.
[248] G. Li, Y. Fan, Y. Lai, T. Han, Z. Li, P. Zhou, P. Pan, W. Wang, D. Hu, X. Liu, Q. Zhang, J. Wu, *J. Med. Virol.* **2020**, DOI 10.1002/jmv.25685.
[249] K. Narayanan, A. Maeda, J. Maeda, S. Makino, *J. Virol.* **2000**, DOI 10.1128/jvi.74.17.8127-8134.2000.
[250] T. R. Ruch, C. E. Machamer, *Viruses* **2012**, DOI 10.3390/v4030363.
[251] D. Schoeman, B. C. Fielding, *Virol. J.* **2019**, DOI 10.1186/s12985-019-1182-0.
[252] F. Li, *Annu. Rev. Virol.* **2016**, DOI 10.1146/annurev-virology-110615-042301.
[253] R. McBride, M. van Zyl, B. C. Fielding, *Viruses* **2014**, DOI 10.3390/v6082991.
[254] A. Tavakoli, M. S. Hashemzadeh, *J. Virol. Methods* **2020**, DOI 10.1016/j.jviromet.2019.113688.
[255] Q. Z. Gan, X. Y. Sun, P. Bhadja, X. Q. Yao, J. M. Ouyang, *Int. J. Nanomedicine* **2016**, *11*, 2839.
[256] M. B. McBride, M. Frenchmeyer, S. E. Kelch, L. Aristilde, *J. Colloid Interface Sci.* **2017**, DOI 10.1016/j.jcis.2016.09.079.
[257] P. M. Ferraro, G. Gambaro, G. C. Curhan, E. N. Taylor, *J. Urol.* **2018**, DOI 10.1016/j.juro.2018.01.077.
[258] K. Komleh, P. Hada, A. K. Pendse, P. P. Singh, *Int. Urol. Nephrol.* **1990**, DOI 10.1007/BF02549826.
[259] T. Ozgurtas, G. Yakut, M. Gulec, M. Serdar, T. Kutluay, *Urol. Int.* **2004**, DOI 10.1159/000077122.
[260] J. F. Desmars, R. Tawashi, *Biochim. Biophys. Acta - Gen. Subj.* **1973**, *313*, 256.
[261] M. Liang, Y. Bai, L. Huang, W. Zheng, J. Liu, *Colloids Surfaces B Biointerfaces* **2009**, DOI 10.1016/j.colsurfb.2009.07.038.
[262] J. Tang, K. McFann, M. Chonchol, *Am. J. Nephrol.* **2012**, DOI 10.1159/000345550.
[263] I. H. Atakan, M. Kaplan, G. Seren, T. Aktoz, H. Gul, O. Inci, *Int. Urol. Nephrol.* **2007**, DOI 10.1007/s11255-006-9050-4.
[264] P. M. Ferraro, G. Gambaro, G. C. Curhan, E. N. Taylor, *J. Urol.* **2018**, *199*, 1534.
[265] H. Park, C. Lee, *Effect of Trace Metals on In Vitro Crystallization of Calcium Oxalate in Agarose Gel Media*, **1989**.
[266] C. Guo, K. E. McMartin, *Toxicology* **2007**, DOI 10.1016/j.tox.2006.11.046.
[267] L. Massey, *Magnes. Res.* **2005**.
[268] A. M. A. Mazen, O. M. O. El Maghraby, *Biol. Plant.* **1997**, DOI 10.1023/A:1001174132428.
[269] M. B. McBride, S. Kelch, M. Schmidt, Y. Zhou, L. Aristilde, C. E. Martinez, *Environ. Sci.*

Technol. **2019**, DOI 10.1021/acs.est.9b05638.
[270] J. A. Muñoz, M. Valiente, *Urol. Res.* **2005**, DOI 10.1007/s00240-005-0468-4.
[271] F. Grases, C. Genestar, A. Millán, *J. Cryst. Growth* **1989**, *94*, 507.
[272] G. E. Tasian, M. E. Ross, L. Song, R. W. Grundmeier, J. Massey, M. R. Denburg, L. Copelovitch, S. Warner, T. Chi, D. W. Killilea, M. L. Stoller, S. L. Furth, *J. Urol.* **2017**, DOI 10.1016/j.juro.2016.11.096.
[273] J. Hofbauer, I. Steffan, K. Hobarth, G. Vujicic, H. Schwetz, G. Reich, O. Zechner, *J. Urol.* **1991**, DOI 10.1016/S0022-5347(17)38256-3.
[274] L. Saso, G. Valentini, M. G. Leone, E. Grippa, B. Silvestrini, *Urol. Int.* **1998**, DOI 10.1159/000030331.
[275] M. K. Li, N. J. Blacklock, J. Garside, *J. Urol.* **1985**, *133*, 123.
[276] A. Hesse, W. Berg, H.-J. Schneider, E. Hienzsch, *Urol. Res.* **1976**, *4*, 157.
[277] M. Santhosh Kumar, R. Selvam, *J. Nutr. Biochem.* **2003**, DOI 10.1016/S0955-2863(03)00033-0.
[278] C. Zhong, Z. Deng, R. Wang, Y. Bai, *Cryst. Growth Des.* **2015**, DOI 10.1021/cg500880m.
[279] V. Georgakilas, M. Otyepka, A. B. Bourlinos, V. Chandra, N. Kim, K. C. Kemp, P. Hobza, R. Zboril, K. S. Kim, *Chem. Rev.* **2012**, *112*, 6156.
[280] T. Yoshino, K. Maruyama, H. Kagi, M. Nara, J. C. Kim, *Cryst. Growth Des.* **2012**, *12*, 3357.

APPENDICES

APPPENDIX A: GRAPHENE LIQUID CELL SYNTHESIS

A1. Graphene Synthesis

Graphene was synthesized *via* the below protocol

Materials

1. Copper foil
2. Ultrapure water
3. Acetone
4. IPA
5. Nitrogen flow
6. CVD, with hydrogen methane and argon attached

Methods

1. Cut copper foil to 2 cm by 3 cm. The copper must be flat, without wrinkles. Be careful not to wrinkle or bend the copper foil throughout the procedure.
2. Rinse the copper foil with ultrapure water.
3. Submerge the copper foil fully in acetone for two minutes (typically within a petri dish).
4. Remove the copper foil, rinse thoroughly with ultrapure water
5. Submerge the copper foil fully in isopropyl alcohol for 2 minutes (typically within a petri dish).
6. Remove the copper foil, rinse thoroughly with ultrapure ware
7. Submerge the copper foil fully in ultrapure water (typically within a petri dish).

8. Dry the copper foil with nitrogen flow.
9. Clean the CVD sample holder and chalice in the sample manner as the copper foil.
10. Rinse the chalice and sample holder with ultrapure water.
11. Submerge the chalice and sample holder fully in acetone for two minutes (typically within a petri dish).
12. Remove the chalice and sample holder, rinse thoroughly with ultrapure water
13. Submerge the chalice and sample holder fully in isopropyl alcohol for 2 minutes (typically within a petri dish).
14. Remove the chalice and sample holder, rinse thoroughly with ultrapure ware
15. Submerge the chalice and sample holder fully in ultrapure water (typically within a petri dish).
16. Dry the chalice and sample holder with nitrogen flow.
17. Place the dried copper sheet or sheets (the chalice may hold up to two 2 cm by 3 cm copper foil sheets).
18. Place the chalice and sample holder into the CVD.
19. Close the CVD, tighten screws to hold vacuum.
20. Slowly bring the CVD to vacuum.
21. Heat the sample at 1000°C for 60 minutes
22. Anneal the sample with 7 SCCM hydrogen at 1000°C for 30 minutes
23. Flow 7 SCCM hydrogen and 5 SCCM methane for 40 minutes
24. Turn off the methane, and cool the sample as quickly as possible while maintaining a flow of 7 SCCM hydrogen

A2 Graphene Coating of TEM Grids

TEM grids were coated with graphene *via* the below protocol.

Materials

1. Graphene coated copper foil, synthesized as described in A.2
2. IPA
3. Ultrapure water
4. Copper etchant
5. Plastic inoculation loops
6. Inverted tweezers
7. Glass slides
8. Glassware: petri dishes, 50 ml beaker

Methods

1. Cut the 2 cm by 3 cm graphene coated copper foil into 1 cm by 1 cm pieces, being careful not to bend the graphene.
2. Mix 1:3 copper etchant to picopure water to create a dilute etchant solution. Typically, add 45 ml picopure water to a petri dish, then add 15 ml etchant. Swirl the mixture.
3. Gently place three 1 cm by 1 cm graphene coated copper pieces onto the etchant
4. Wait for the copper to vanish (about 30 minutes). Then allow an additional 30 minutes for non-visible copper nanoparticles to fully dissolve.
5. Separately, fill a sterile 50ml picopure water
6. Bend a plastic bacteria inoculation loop to an approximately 60° angle
7. Use the loop to lift a piece of graphene using the surface tension of the water within the loop

8. Gently touch the loop, graphene side up, to the surface of the water. Repeat this step twice
9. Place a copper lacey carbon coated grid, carbon side down, directly onto the graphene.
10. Using inverted tweezers, reach through the bottom of the loop to grab the grid, drawing the graphene onto the TEM grid.
11. Place the inverted tweezers on a sterile benchtop, graphene side up
12. Place 0.1 µl IPA on the top of the graphene
13. Place the grid underneat a heat lamp for two hours to fully adhere the graphene to the TEM grid.

APPENDIX B: BACTERIAL CULTURING, PARTICLE SUSPENSION PREPERATION, AND ANTIBACTERIAL TESTING

B1. Sterile LB Broth Synthesis

LB broth is purchased as a powder containing vital nutrients, salts, and minerals essential to bacterial growth. Without the LB medium, bacteria will 1) lyse, due to the hypotonicity of water. The influx of the water then increases the osmotic pressure of the bacteria. 2) without the nutrients and minerals, the few bacteria that are added to the solution to divide and population the culture do not undergo binary fission, age, and die. Here, the LB broth synthesis procedure and antiseptic techniques are described below.

Materials

1. LB broth powder
2. Ultrapure or DI water
3. Stir Bar
4. 125 ml bottles with cap
5. Autoclave
6. Autoclave tape

Procedure

1. Add 25 g LB powder to a 125 ml bottle with a cap. Label with sharpie at this step, not after autoclaving.
2. Fill to 100 ml with ultrapure water
3. Add clean stir bar

4. Place on hot plate, spin at 200 rpm until powder is dissolved. A few specks 0.1 cm in diameter are acceptable. Some LB may attached to the sides of the bottle. Move the bottle around the hot plate to break up the LB powder chunks.
5. Remove the stir bar with a magnet or tongs.
6. Loosely cover the bottle with the cap such that air can easily escape. If this step is forgotten the bottle will explode during autoclaving.
7. Place a small piece of autoclave tape on each bottle.
8. Place the bottle or bottles of LB broth in the autoclave such that the bottles do not touch the sides or top of the autoclave, and do not touch each other.
9. Add water to the autoclave as necessary.
10. Autoclave for 40 minutes at 120°C.
11. Allow to cool in the autoclave till warm but not hot to the touch.
12. Tighten caps immediately upon removal from the autoclave.

B2. Liquid LB Broth *E. coli* Culture Synthesis

Liquid *E. coli* cultures are essential in antibacterial testing. Substances such as the PLGA MPs and AgNPs utilized here can be added to the *E. coli* cultures. Over time, the antibacterial agent lowers the population of bacteria or retards the solution growth rate. The precise liquid LB broth *E. coli* culture synthesis technique is detailed below.

Materials

1. Ethanol (optional)
2. Bleach

3. Biosafety cabinet with UV
4. LB broth powder
5. Ultrapure or DI water
6. Stir bar
7. Magnet or tongs
8. Hot plate
9. Autoclave
10. Autoclave tape
11. Aluminum foil
12. Burner
13. Lighter
14. Disposable inoculation loops
15. 500 ml beaker
16. Frozen, preserved *E. coli* culture
17. Incubator with shaker

Procedure

1. Sterilize a biosafety cabinet
    a. Clean with ethanol or bleach
    b. Turn UV light on for at least 20 minutes, leave on throughout experiment when not actively working in the cabinet.
2. Add 1 gram LB broth powder to 125 ml flask
3. Fill to 25 ml with ultrapure or DI water

4. Add clean stir bar
5. Place on hot plate, spin at 200 rpm until powder is dissolved. A few specks 0.1 cm in diameter are acceptable. Some LB may attached to the sides of the flask. Move the flask around the hot plate to break up the LB powder chunks.
6. Remove the stir bar with a magnet or tongs.
7. Loosely cover the flask with aluminum foil, such that air can escape during autoclaving.
8. Add a small piece of autoclave tape to the side of each flask
9. Label each flask.
10. Place the flask or flasks of LB broth in the autoclave such that the flasks do not touch the sides or top of the autoclave, and do not touch each other.
11. Add water to the autoclave as necessary.
12. Autoclave for 40 minutes at 120°C.
13. Allow to cool in the autoclave till no longer hot to the touch, about 20 minutes.
14. Place in biosafety cabinet. Tighten aluminum foil. Turn on UV.
15. Place sterile inoculation loops in the biosafety cabinet
16. Fill a 500 ml beaker to 100 ml with 20% bleach and 80% water, place under UV in biosafety cabinet.
17. Place flame and lighter under UV
18. Place one disposable inoculation loop per flask under UV in biosafety cabinet
19. Allow the LB to reach room temperature, about one hour.
    a. Flip lighter and loops after 30 minutes to thoroughly sterilize all components of the experiment.
20. Retrieve frozen *E. coli* stock from -80ºC

21. Open the end of an inoculation loop at the opposite end from the loop itself. Never touch the inoculation loop itself, only the attached distal handle
22. Remove the foil from one flask without setting it down.
23. Open the *E. coli* stock without setting the lid down or touching the inside of the lid. Grip the lid between your pinkie finger and palm.
24. Scrape the surface of the *E. coli* stock with the inoculation loop.
25. Place the inoculation loop into the LB flask.
26. Close the frozen *E. coli* stock.
27. Gently swirl the inoculation loop within the LB broth.
28. Remove the inoculation loop, place in 20% bleach beaker.
29. Flame the foil.
30. Cover flask with foil
31. Flame the top of the flask without heating LB broth.
32. Repeat steps 21-31 for each flask.
33. Place flasks in bacteria incubator at 37.5C on shaker at 100 rpm.
34. Culture for 12 hours to reach the stationary phase of bacterial growth. The stationary phase is the point at which the *E. coli* concentration is constant, such that the death rate is equal to the rate of binary fission.

B3. Fluorescent Live/Dead Testing

The morphology of the *E. coli* and the live/dead ratio were determined by fluorescent staining. Here, a fluorescent protein binds to all bacteria and fluoresces green, indicating all bacteria. Another protein fluoresces red only when bound to dead bacteria. The total live/dead ratio can be

determined by collecting images from the same area and observing the red/green ratio through different fluorescent filters. In Figure 3 A and B, *E. coli* was exposed to bleach to create a positive control with expected low viability. The results showed 3% viability. A separate culture was created and untreated with bactericidal agents to create a negative control with an expected high viability of 90% as shown in Figure 3 C and D. Control culturing consistently showed viability rates of approximately 85% in untreated samples. The precise fluorescent live/dead testing procedure is detailed below.

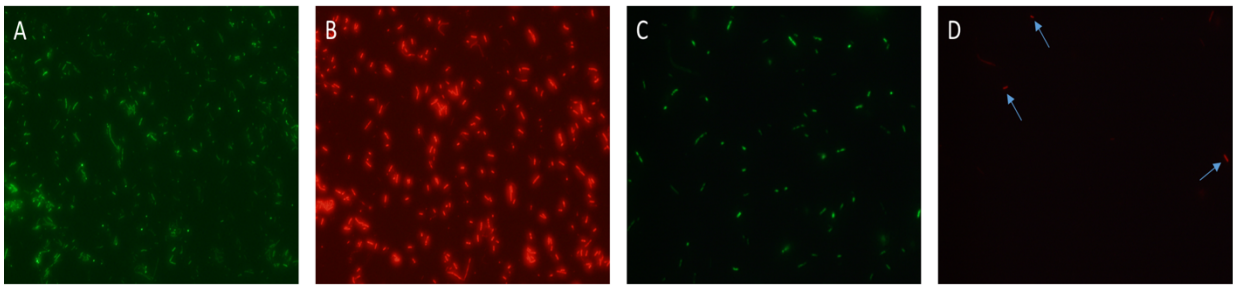

Figure B1. Live/dead staining of *E. coli* with a positive control culture (with bleach) show a low viability rate (**a**, **b**) and a negative control culture (with no bactericidal agent) show a high viability rate (**c**, **d**). In A, all bacteria present are stained green. In **b**, dead bacteria appear red, imaged from the same are shown in **a**. Unstained, live bacteria are not visible in **b** but are visible in **a**. In **c**, green stained bacteria are visible. In **d**, much fewer bacteria from the same area shown in **c** are visible, indicating the high viability rate of the sample.

Materials

1. Frozen live/dead fluorescent stain
2. Sterile PBS
3. Liquid LB *E. coli* cultures as synthesized in Appendix B.3

4. Glass slides
5. Slide covers
6. Clear nail polish
7. Ethanol
8. Kim wipes
9. Burner
10. Lighter
11. Microcentrifuge tubes
12. 10 µl pipette
13. 10 µl pipette tips
14. 1 ml pipette
15. 1 ml pipette tips
16. Electric pipette
17. 25 ml pipettes
18. Aluminum foil
19. 500 ml beaker
20. Bleach

Methods

1. Sterilize slide with ethanol and a kim wipe. Let ethanol fully evaporate.
2. Light burner and pass the slide through the flame several times (approximately 3).
3. Wrap a microcentrifuge tube with aluminum foil
4. Remove the frozen live/dead fluorescent stain and place under aluminum foil to prevent light exposure. Partially that for 5 minutes.

5. Extract 5 µl of stain A and add it to the microcentrifuge tube.
6. Extract 5 µl of stain B and add it to the microcentrifuge tube.
7. Pick the liquid up with the pipette three times to mix the solution.
8. Return the live/dead fluorescent stain to the freezer immediately.
9. Add 20 ml of bleach to a 500 ml beaker
10. Remove the LB broth *E. coli* culture from the incubator.
11. Pour the *E. coli* culture into a 50 ml centrifuge tube
12. Centrifuge for 10 minutes at 3000 RPM to form an *E. coli* pellet
13. Using a 25 ml pipette, remove the LB broth without disturbing the pellet. Put the LB broth in the beaker containing bleach.
14. Add 50 ml sterile PBS to the centrifuge containing the *E. coli* pellet
15. Vortex the *E. coli* pellet to suspend the *E. coli* in the PBS solution.
16. Extract 1 ml of the *E. coli* PBS suspension and add to a 2 ml microcentrifuge tube.
17. Add 0.5 µl of the florescent stain to the 1 ml *E. coli* PBS suspension
18. Place the florescent stain in the freezer. It may be reused.
19. Pick the 1 ml *E. coli* PBS suspension up twice to mix the solution.
20. Place 0.5 µl of the *E. coli* PBS suspension on the sterile glass slide
21. Cover with a slide cover
22. Gently cover the edges of the slide cover with clear nail polish, applying only a thin layer.
23. Place aluminum foil over the slide without touching the slide to block the light
24. Wait approximately 10 to 20 minutes for the nail polish to dry
25. Collect red and green images under a fluorescent microscope.

B4. Silver Nanoparticle Suspension Preparation

Materials

1. PBS
2. Microcentrifuge tubes
3. Silver Nanoparticles
4. Sonicator
5. UV light

Methods

1. Sterilize PBS
    a. Add 100 ml PBS to 125 ml bottle.
    b. Place a small piece of autoclave tape on each bottle.
    c. Cover the bottles with the caps loosely, so that air can escape during autoclaving
    d. Place the bottle or bottles of PBS in the autoclave such that the bottles do not touch the sides or top of the autoclave, and do not touch each other.
    e. Add water to the autoclave as necessary.
    f. Autoclave for 40 minutes at 120°C.
    g. Allow to cool in the autoclave till warm but not hot to the touch.
    h. Tighten the cap and allow the bottle to reach room temperature.
    i. At the end of each experiment, the PBS may be autoclaved (steps c-g) and reused several times. It is also advisable to autoclave the PBS prior to the next experiment.
2. Add 1 ml sterile PBS to a 2 ml microcentrifuge tube
3. Sonicate for 5 minutes
4. Place under UV to sterilize the AgNP suspension

B5. Conventional TEM Sample Preparation

Materials

1. Ethanol
2. 15 ml centrifuge tubes
3. LB broth *E. coli* culture as synthesized in Appendix B.2
4. Centrifugre
5. 25 ml pipette tips
6. Electric pipette
7. Sterile PBS
8. Gluteraldehyde
9. Osmium tetroxide
10. Embred 812
11. DDSA
12. NMA
13. DMP
14. PO
15. Ultramicrotome
16. Ultramicrotome bowl
17. 2% uranyl acetate
18. 1% lead citrate
19. Well plates.
20. 60°C oven
21. 4°C refrigerator

22. Inverted tweezers
23. Uncoated copper TEM grids.

Methods

1. Prepare the following stock ethanol dilutions
    a. 30% ethanol, 70% water
    b. 50% ethanol, 50% water
    c. 70% ethanol, 30% water
    d. 80% ethanol, 20% water
    e. 95% ethanol, 5% water
    f. 100% ethanol
2. Remove the previously prepared LB broth *E. coli* culture from the incubator
3. Fill a 15 ml centrifuge tube with the *E. coli* culture
4. Centrifuge for 10 minutes at 3000 RPM to form an *E. coli* pellet
5. Using a 25 ml pipette, remove the LB broth without disturbing the pellet. Put the LB broth in the beaker containing bleach.
6. Add 10 ml sterile PBS to the centrifuge containing the *E. coli* pellet
7. Vortex the *E. coli* pellet to suspend the *E. coli* in the PBS solution.
8. Centrifuge for 10 minutes at 3000 RPM to form an *E. coli* pellet
9. Add 2.5% glutaraldehyde to the centrifuge tube
10. Set the centrifuge tube in a 4°C refrigerator overnight (at least 8 hours)
11. Using a 25 ml pipette, remove the glutaraldehyde without disturbing the pellet
12. Add 10 ml sterile PBS to the centrifuge tube without disturbing the pellet

13. Using a 25 ml pipette remove the PBS without disturbing the pellet to rinse the sample
14. Add 5 ml 1% osmium tetroxide to the centrifuge tube without disturbing the pellet
15. Wait one hour.
16. Remove the osmium tetroxide with a 25 ml pipette
17. Add 10 ml sterile PBS to the centrifuge tube without disturbing the pellet
18. Using a 25 ml pipette remove the PBS without disturbing the pellet to rinse the sample
19. Add 5 ml of the 30% ethanol, 70% water solution to the centrifuge tube
20. Wait 30 minutes
21. Using a 25 ml pipette, remove the ethanol and water solution without disturbing the pellet
22. Repeat steps 19-21 for each ethanol dilution
    a. 50% ethanol, 50% water
    b. 70% ethanol, 30% water
    c. 80% ethanol, 20% water
    d. 95% ethanol, 5% water
    e. 100% ethanol
23. Repeat step 22e.
24. Separately prepare Embed 812 and PO solutions
    a. Prepare Embed 812 resin by combining 20 ml Embed 812, 16 ml DDSA, 8 ml NMA, and 0.77 ml DMP
    b. Stir Embed 812 resin thoroughly until homogenous
    c. Prepare PO and Embed 812 resin dilutions. Stir thoroughly
        i. 3:1 PO:Embed 812 resin

ii. 1:1 PO:Embed 812 resin

iii. 1:3 PO:Embed 812 resin

iv. 0:1 PO:Embed 812 resin

25. Add 3:1 PO:Embed 812 resin to the centrifuge containing the bacteria pellet
26. Wait 30 minutes
27. Repeat steps 25 and 26 for each 3:1 PO:Embed 812 resin dilution
28. Wait until the 100% Embed 812 resin solution is viscus but not set
29. Pour into resin block mold, making sure the bacteria pellet is in contact with the sharp tip and that there are no bubbles
30. Place the resin block mold in a 60°C oven for 48 hours
31. Remove the resin block from the oven and allow the resin to completely cool
32. Microtome into 100 nm thick slices, using a wet boat to capture the resin slices
33. Using inverted tweezers, pick up an uncoated copper TEM grid.
34. Use the copper TEM grid to lift a resin slize out of the wet boat
35. Allow to dry for 24 hours.
36. Add water to two plate wells, 2% uranyl acetate to a plate well, and 1% lead citrate to a plate well.
37. Put the TEM grid with the resin in the uranyl acetate for 12 minute
38. Rinse the TEM grid by placing it in the first water solution.
39. Put the TEM grid with the resin in the lead citrate for 1 minute
40. Rinse the TEM grid by placing it in the second water solution
41. Allow the grid to completely dry.

B6. PLGA Microparticle Etching

This procedure produces the rough MPs as implemented in this work. The etching process has been adapted from Serrano et al, who used a similar approach to etch microfibers. Here, microparticles are drop-cast on copper sheets to prevent movement of the sample during plasma etching. Unetched MPs were deposited on copper and were subjected to every step except plasma etching.

Methods

1. PLGA MPs
2. Ultrapure or DI water
3. 2ml Microcentrifuge tubes
4. Copper foil
5. IPA
6. Acetone
7. Nitrogen flow
8. Glass petri dishes
9. Plasma etcher with argon flow
10. PBS
11. Sonicator

Methods

1. Add the desired weight of PLGA MPs to a 2 ml microcentrifuge tube.
2. Fill to 1 ml with ultrapure or DI water
3. Sonicate the microcentrifuge tube for 5 minutes.

4. Separately, cut copper foil to 2 cm by 3 cm. The copper must be flat, without wrinkles. Be careful not to wrinkle or bend the copper foil throughout the procedure.
5. Rinse the copper foil with ultrapure water.
6. Submerge the copper foil fully in acetone for two minutes (typically within a petri dish).
7. Remove the copper foil, rinse thoroughly with ultrapure water
8. Submerge the copper foil fully in isopropyl alcohol for 2 minutes (typically within a petri dish).
9. Remove the copper foil, rinse thoroughly with ultrapure ware
10. Submerge the copper foil fully in ultrapure water (typically within a petri dish).
11. Dry the copper foil with nitrogen flow.
12. Add 10 ul droplets of the PLGA solution to copper sheets, with at least 0.25 cm between each drop, until the 1 ml solution is fully distributed.
13. Allow to dry for at least 12 hours.
14. Place copper sheets in glass petri dishes, MP side up.
15. Before etching the MP, calibrate the plasma etcher settings without the MPs
    a. Pump the plasma etcher to vacuum.
    b. Flow 10 ppm argon through the plasma etcher
    c. Set the watts to 100. Ensure there is a pink glow
    d. Turn off the etcher, bring to atmospheric pressure
16. Place petri dishes contain the MP in the plasma etcher.
17. Pump to vacuum, with 10 ppm argon flow.
18. Etch the nanoparticles by turning the etcher on for one minute, and then off for two minutes. Repeat the procedure to achieve a total etched time.

a. For 2 minutes, repeat step 18 twice

b. For 5 minutes, repeat step 18 five times

19. Bring the plasma etcher to atmospheric pressure

20. Repeat steps 16-19 for each condition.

21. Separately, sterilize PBS.

    a. Add 100 ml PBS to 125 ml bottle.

    b. Place a small piece of autoclave tape on each bottle.

    c. Cover the bottles with the caps loosely, so that air can escape during autoclaving

    d. Place the bottle or bottles of PBS in the autoclave such that the bottles do not touch the sides or top of the autoclave, and do not touch each other.

    e. Add water to the autoclave as necessary.

    f. Autoclave for 40 minutes at 120°C.

    g. Allow to cool in the autoclave till warm but not hot to the touch.

    h. Tighten the cap and allow the bottle to reach room temperature.

    i. At the end of each experiment, the PBS may be autoclaved (steps c-g) and reused several times. It is also advisable to autoclave the PBS prior to the next experiment.

22. Cut the copper strips with the MPs on them into 1 cm by 1 cm pieces.

23. Add 1.5 ml sterile PBS to a sterile microcentrifuge tube.

24. Add one 1 cm by 1 cm piece of copper foil to the microcentrifuge tube.

25. Sonicate for 5 minutes to remove the MPs.

26. Repeat 23-25 for each condition in separate microcentrifuge tubes containing PBS, with 0, 2, or 5 minutes.

B7. LB Agar Plate Synthesis

LB agar consists of LB nutrients contained in an agar gel. The agar gel is a protein matrix that provides a solid surface for the bacteria to grow. These plates are essential in selecting individual colonies for innoculation or for procedures such as colony counting. The precise agar plate synthesis protocol is detailed below.

Materials

1. Biosafety cabinet with UV light
2. Ethanol or bleach
3. LB Agar powder
4. Ultrapure or DI water
5. Hot Plate
6. Stir bar
7. Magnet or tongs
8. 125 ml bottle with cap
9. Autoclave tape
10. Autoclave
11. Petridishes
12. Plastic bag and tape for storage of the agar plates

Procedure

1. Sterilize a biosafety cabinet
    a. Clean with ethanol or bleach

b. Turn UV light on for at least 20 minutes, leave on throughout experiment when not actively working in the cabinet.

2. Add 4g LB Agar powder to a 125 ml bottle
3. Fill to 100 ml with ultrapure or DI water
4. Add clean stir bar
5. Place on hot plate, spin at 200 rpm until powder is dissolved. A few specks 0.1 cm in diameter are acceptable. Some LB may attached to the sides of the bottle. Move the bottle around the hot plate to break up the LB powder chunks.
6. Remove the stir bar with a magnet or tongs.
7. Loosely cover the bottle with the cap such that air can easily escape. If this step is forgotten the bottle will explode during autoclaving.
8. Place a small piece of autoclave tape on each bottle.
9. Place the bottle or bottles of LB broth in the autoclave such that the bottles do not touch the sides or top of the autoclave, and do not touch each other.
10. Add water to the autoclave as necessary.
11. Autoclave for 40 minutes at 120°C.
12. Allow to cool in the autoclave till hot to the touch, about 20 minutes.
13. Tighten caps immediately upon removal from the autoclave.
14. Place bottles in biosafety cabinet
15. Place plastic petri dishes in the biosafety cabinet, such that the petridishes are each exposed to the UV light
16. Label the petri dishes as necessary. Expose to UV for at least 10 minutes to sterilize them.

17. When the LB Agar is warm to the touch, but not hot, add one third of each bottle (approximately 30 ml) to each petri dish.
18. Partially cover the petri dishes with lids such that a small amount of air can flow.
19. Turn on UV
20. Allow petri dishes to fully set under UV for at least three hours.
21. The petri dishes may be directly used, or stored for future use.
    a. To store the petri dishes, place a plastic bag (typically included with pentri dish purchases) under UV for at least 10 minutes.
    b. Invert the petri dishes such that the agar is on the top
    c. Place petri dishes in the plastic bag
    d. Seal bag with tape, label. Petri dishes should be used within one week
    e. To use the petri dishes at a later date, sterilize a biosafety cabinet as described in step 1. Invert the petri dishes such that the agar is in the bottom if the dish. Turn on UV and allow the petri dishes to reach room temperature, approximately two hours.

B8. Antibacterial Testing *via* Colony Counting

Materials

1. Biosafety cabinet with UV
2. Incubator
3. Autoclave
4. 1 ml pipette
5. 10 µl pipette
6. 1 ml pipette tips

7. 10 µl pipette tips
8. Etched PLGA MP and unetched PLGA MP suspensions
9. Ethanol (optional)
10. Bleach
11. 48 inoculation loops
12. 48 LB gar plates
13. 12 LB *E. coli* culture flasks
14. Sterile PBS

Methods

1. Sterilize a biosafety cabinet.
    a. Clean with ethanol or bleach.
    b. Turn UV light on for at least 20 minutes, leave on throughout experiment when not actively working in the cabinet.
2. Place 48 agar plates under UV light. If previously prepared and stored, allow the plates to reach room temperature for 2 hours under UV light.
3. Autoclave 1 ml pipette tips. Allow to cool to room temperature.
4. Autoclave 10 µl pipette tips. Allow to cool to room temperature
5. Place PLGA suspensions etched for zero minutes, two minutes, and 5 minutes, AgMPs suspended in PBS, burner, lighter, and 1 ml pipette with stand under UV light for at least ten minutes.
6. Place 48 inoculation loops under UV light for at least ten minutes.
7. Remove 12 previously made *E. coli* in LB broth flasks from the incubator and place in biosafety cabinet with UV light off.

8. Create time 0 plates. This step should be performed quickly, within 30 minutes.
    a. Remove the foil from an *E. coli* flask without setting the foil down.
    b. Add 1 µl of the *E. coli* solution to a sterile microcentrifuge tube
    c. Add 99 µl of sterile PBS to create a 10^{-2} dilution
    d. Repeat a-c for each flask. Return the LB flasks to the incubator.
    e. From the 10^{-2} dilution, add 1 µl to a microcentrifuge tube
    f. Add 99 µl of sterile PBS to create a 10^{-4} dilution
    g. From the 10^{-4} dilution, add 1 µl to a microcentrifuge tube
    h. Add 99 µl of sterile PBS to create a 10^{-6} dilution
    i. Extract 10 µl from one dilution, add to the center of an agar plate
    j. Bend an inoculation loop to approximately a 60° angle without opening the loop package
    k. Open the inoculation loop at the end distal from the loop itself
    l. Touch the droplet of the *E. coli* solution, and spread it evenly across the agar plate
    m. Repeat this procedure for each dilution of each flask on separately agar plates. There should be a total of 48 plates.
9. Remove the flasks from the incubator
10. Without setting the foil down, remove the foil from a flask
11. Add 0.5 ml of the PLGA etched for zero minutes and PBS suspension to the *E. coli* flask.
12. Flame the foil
13. Cover the flask with the foil
14. Flame the top of the flask without heating the LB broth.

15. Repeat steps 10 through 14 to create a second, separate *E. coli* flask containing 0.5 ml of the PLGA etched for zero minutes and PBS suspension.
16. Repeat steps 10 though 15 for PLGA suspensions etched for two minutes, 5 minutes, and for the AgMPs suspended in PBS.
17. For the two control samples, repeat steps 10-15 use sterile PBS in place of PLGA or AgNPs
18. Return the flasks to the incubator
19. Four hours later, repeat step 8.
20. Four hours later, repeat step 8.
21. Dispose of the flasks
    a. Add bleach in a 20% volume (10 ml)
    b. Swirl solutions
    c. Let sit 20 minutes in the sink
    d. Slowly pour sterilized solutions down the drain, with plenty of water flowing
    e. Clean sink with bleach
    f. Clean flasks with bleach and soap solutions.
22. Extrapolate the concentration of *E. coli* at each time point from the agar plates *via* colony counting. 10 µl were added to each plate, so the number of observed colonies should be divided by their dilution factor (10^{-2}, 10^{-4}, 10^{-6}), which gives the concentration in 10 µl. The concentration is then converted to colony forming units per milliliter.

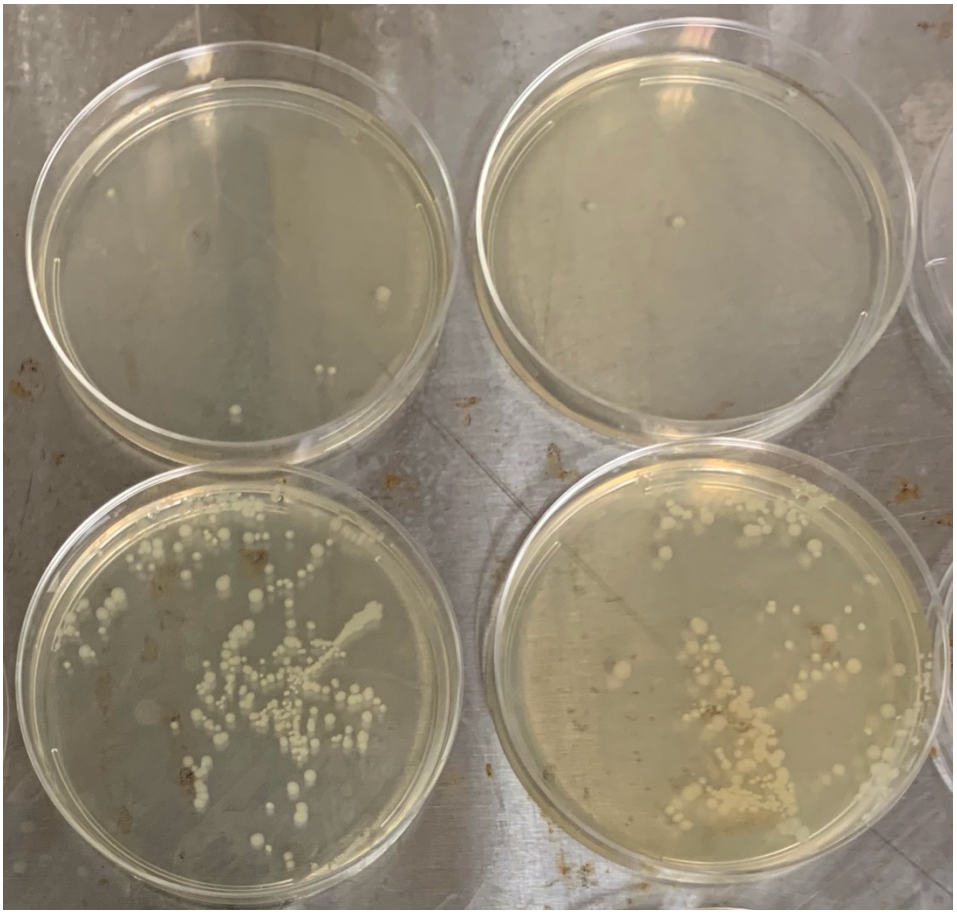

Figure B2. Shows example agar plates. Individual colonies are visible, which may be counted to extrapolate the concentration of bacteria in the LB culture flasks. In **(a)** through **(d)**, agar plates synthesized from LB broth cultures are displayed. In a and b, the sample was diluted to a 10^{-6} concentration, while in **(c)** and **(d)**, the sample was diluted to 10^{-4} concentration.

B9. False colorization of figures 3.6 and 3.7

TEM images were false colorized using ImageJ and GIMP. For each image, ImageJ split color channels into cyan, magenta, and yellow. GIMP was used to manually erase portions of the images. The images were then overlaid and exported to form a single image. The original, unaltered figure 2 and 3 are displayed below.

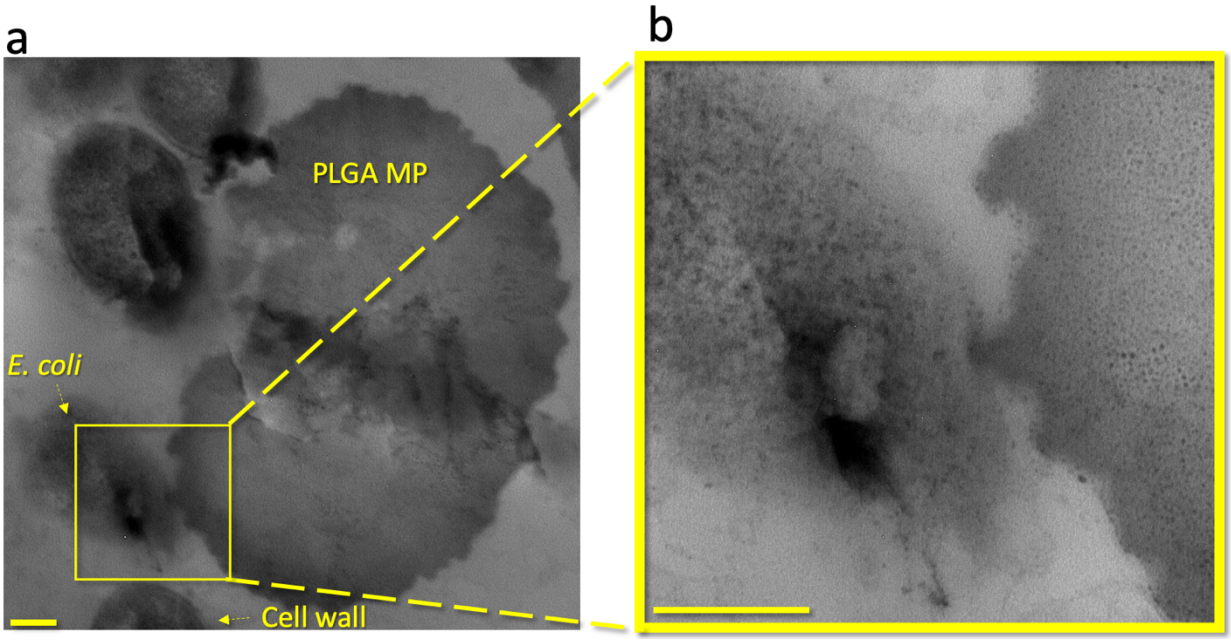

Figure B3. Unaltered (non-colorized) version of figure 3.6. Bacterial death is induced by rough MP topography. In **(a)** and **(b)**,low to high magnification images show the surface interaction between an *E. coli* bacterium and a rough PLGA particle etched for 2 minutes. A sharp protrusion on the PLGA particle appears to have penetrated the *E. coli* bacterium cell wall. The area bracketed in **(a)** is shown at higher magnification in **(b)**. The scale bars in **(a)** and **(b)** are 200 nm.

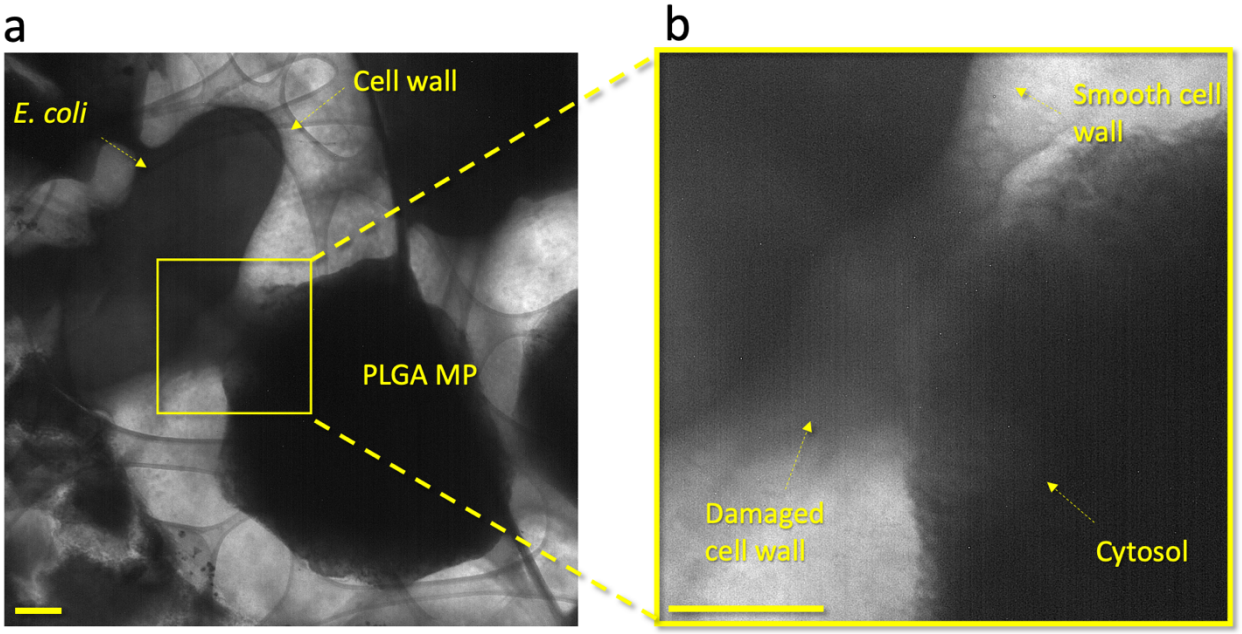

Figure B4. Unaltered version figure 3.7. GLC encapsulation of *E. coli* and PLGA MPs shows localized damage to the cell wall of a bacterium. In **(a)**, a lower magnification image shows the *E. coli* particle and the PLGA MP. In **(b)**, a higher magnification image shows the PLGA particle and bacterium in close proximity. The cell wall proximal to the PLGA particle shows damage with a shape similar to the adjacent wall. A high contrast liquid indicates the cytosol of the bacterium, which confirms its death. The cytosol has a higher contrast than the PBS medium due to the protein, glycans, and other bacterial components within the cytosol. Other areas of the *E. coli* cell wall are smooth and show no damage or degradation. The scale bars in **(a)** and **(b)** are 200 nm.

APPENDIX C: CALCIUM OXALATE SAMPLE PREPERATION

C1. Synthesis of 0.1 M Calcium Oxalate Solutions

Materials

1. $CaCl_2$ powder
2. Sodium Oxalate
3. Picopure Water
4. 10 ml Graduated Cylinder
5. 15 ml microcentrifuge tubes
6. Vortx
7. Sonicator

Procedure

1. Creation of 0.5 M $CaCl_2$ stock solutions
    a. Add 0.55 g $CaCl_2$ to a 15 ml centrifuge tube.
    b. Fill the centrifuge tube to 10 ml with picopure water.
    c. Inverted the $CaCl_2$ solution 10 times to mix the solution, vortex for 1 minute, and sonicate for 5 minutes to fully dissolve the $CaCl_2$.
2. Creation of 0.125 M NaOx stock solutions
    a. Add 0.167 g NaOx to a 15 ml centrifuge tube
    b. Fill the centrifuge tube to 10 ml with picopure water
    c. Invert the NaOx solution 10 times to mix the solution, vortex or 1 minute, and sonicate for 5 minutes to fully dissolve the NaOx.
3. Creation of 0.1 M CaOx solutions

a. Vortex the 0.5 M $CaCl_2$ stock solution and the 0.125 M NaOx and 0.125 sodium citrate stock solution for 1 minute, then sonicate the stock solutions for 10 minutes.
b. Add 100 µl of the 0.5 M $CaCl_2$ stock solution to a 1 ml microcentrifuge tube.
c. Add 400 µl of the 0.167 M NaOx to the same microcentrifuge tube.
d. Pick the solution up with the pipette several time to mix the solution.
e. Invert the microcentrifuge tube 10 times to mix the solution.

C2 Synthesis of 0.1 M Calcium Oxalate and 0.1M Citrate Solutions

Materials

1. $CaCl_2$ powder
2. Sodium Oxalate
3. Sodium Citrate
4. Picopure Water
5. 10 ml Graduated Cylinder
6. 15 ml microcentrifuge tubes
7. Vortx
8. Sonicator

Procedure

1. Creation of 0.5 M $CaCl_2$ stock solutions
    a. Add 0.55 g $CaCl_2$ to a 15 ml centrifuge tube
    b. Fill the centrifuge tube to 10 ml with picopure water
    c. Invert the $CaCl_2$ solution 10 times to mix the solution, vortex or 1 minute, and sonicate for 5 minutes to fully dissolve the $CaCl_2$.

2. Creation of 0.125 M NaOx and 0.125 M sodium citrate stock solutions
    a. Add 0.167 g NaOx to a 15 ml centrifuge tube
    b. Add 0.322 g sodium citrate to a 15 ml centrifuge tube
    c. Fill the centrifuge tube to 10 ml with picopure water
    d. Invert the NaOx solution 10 times to mix the solution, vortex or 1 minute, and sonicate for 5 minutes to fully dissolve the NaOx.
3. Creation of 0.1 M CaOx and 0.1 M sodium citrate solutions
    a. Vortex the 0.5 M $CaCl_2$ stock solution and the 0.125 M NaOx and 0.125 sodium citrate stock solution for 1 minute, then sonicate the stock solutions for 10 minutes.
    b. Add 100 µl of the 0.5 M $CaCl_2$ stock solution to a 1 ml microcentrifuge tube.
    c. Add 400 µl of the 0.125 M NaOx and 0.125 sodium citrate stock solution to the same microcentrifuge tube.
    d. Pick the solution up with the pipette several time to mix the solution.
    e. Invert the microcentrifuge tube 10 times to mix the solution.

APPENDIX D: FALSE COLORIZATION OF TEM IMAGES, ELECTRON BEAM EFFECTS, AND THE EFFECTS OF PRESSURE

D.1 False Colorization of Figures 4.2, 4.3, and 4.4.

Figures were false colorized using ImageJ and GIMP. In ImageJ, each image was converted to an 8-bit image. Each image was then filtered with a Lookup Table filter, which made the images blue, green, and yellow. GIMP was used to manually erase portions of the images. The images were then overlayed and exported to form a single image. The original, unaltered figure 2 and 3 are displayed below.

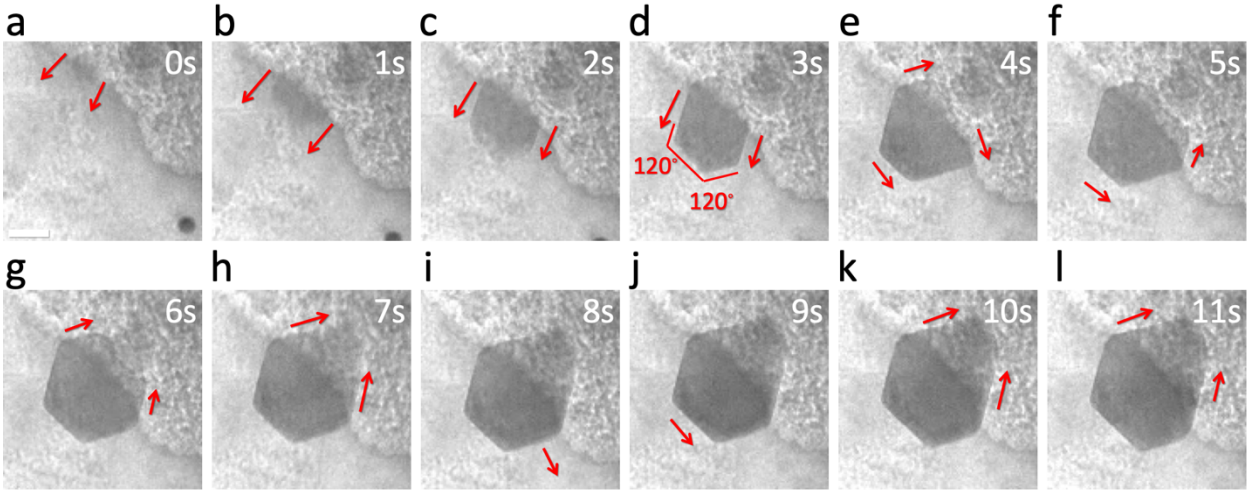

Figure D1. Unaltered version of the false colorized GLC TEM images in figure 4.2. The classical nucleation pathway of CaOx crystal formation within GLC-TEM. The process starts *via* formation of a stable nucleus followed by monomer addition to the growing crystal. The particle grows along specific facets as indicated by the red arrows. The time series from the beginning of particle formation is included in the upper right corner of each image. All images were collected from the same magnification. The scale bar in **(a)** is 50 nm.

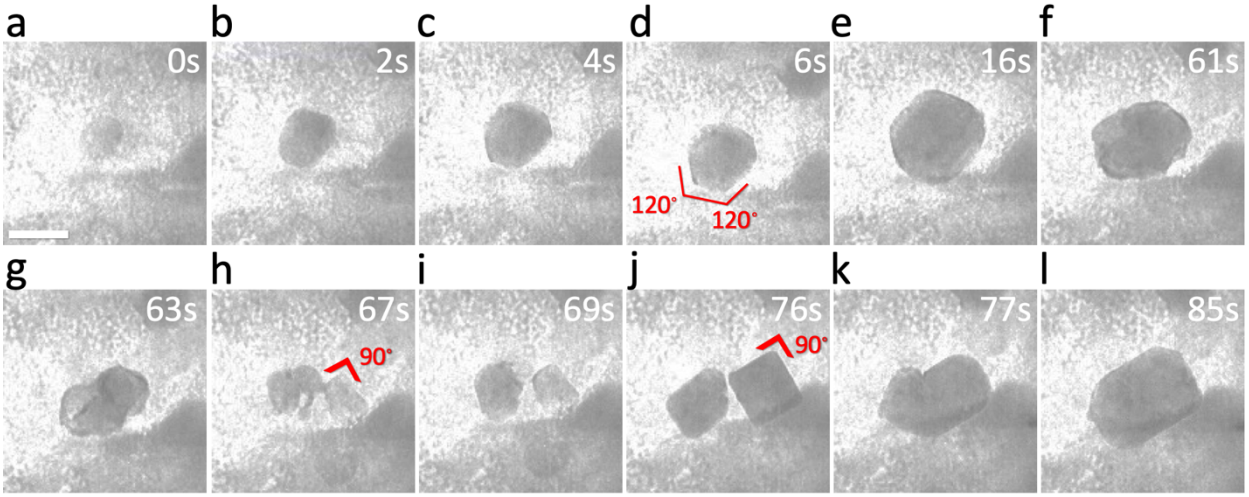

Figure D2. Unaltered version of the false colorized GLC TEM images in figure 4.3. The non-classical formation pathway of CaOx within GLC in the absence of citrate. The particle shows initial classical formation *via* formation of a central nanoscale nucleus followed by ionic addition to the growing crystal (**a** through **e**). However, throughout the video the 120° corners are not as sharp as in figure 4.2, indicating the particle is not fully crystalline. Eventually, the sharpness of the corners decreases in **(f)** until the particles nearly, but not entirely, dissolve (**f** through **i**). The particle leaves behind two apparently amorphous particles, which then begin displaying 90° corners (**j**). The particle corners continue to sharpen throughout growth, until the two particles coalescence. The scale bar in **(a)** is 50 nm.

Figure was false colorized using ImageJ. Each image was converted to an 8-bit image. A lookup table mask was then used to colorize the Image. The Lookup mask Phase was selected. The image contrast was then inverted. The original, unedited image figures are included below.

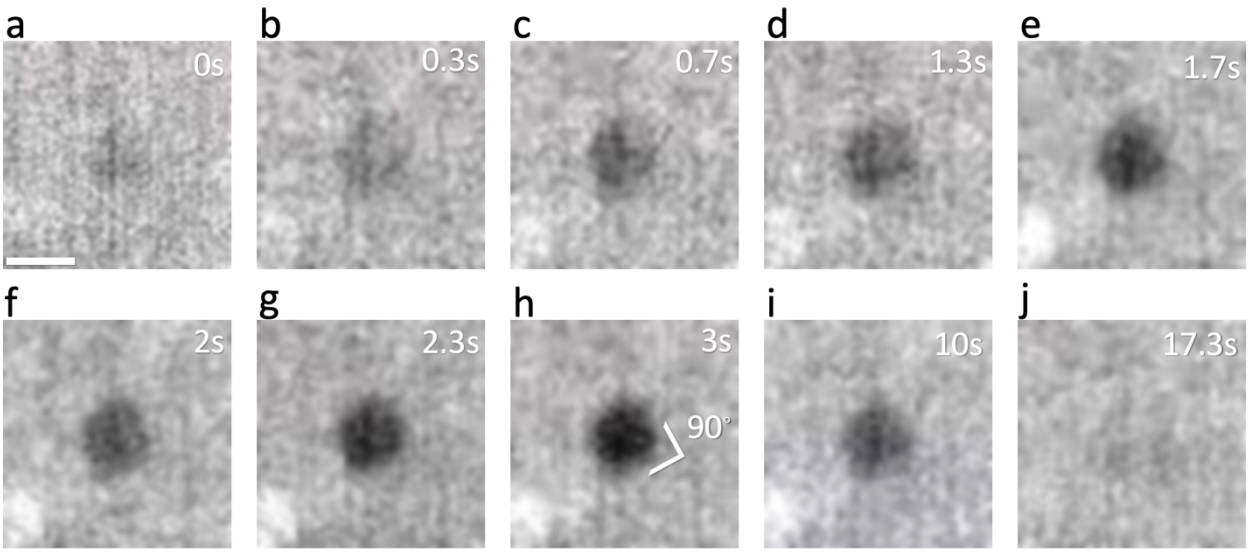

Figure D3. Unaltered version of the GLC TEM images in figure 3. Repeated CaOx formation and dissolution in the presence of citrate. The particle forms with a diameter of approximately 20 nm, and increases in contrast throughout **(a)** through **(h)**. In **(h)**, the particle develops 90° corners. This particle fluctuates in diameter, contrast, and corner sharpness before dissolving **(j)**. In **(k)**, MD simulations shows aggregation of calcium and oxalate ions during nucleation. In contrast, in **(l)** MD simulations show that calcium:citrate interactions prevent nucleation of CaOx. All TEM images were collected at the same magnification in the same area. The scale bar in **(a)** is 20 nm.

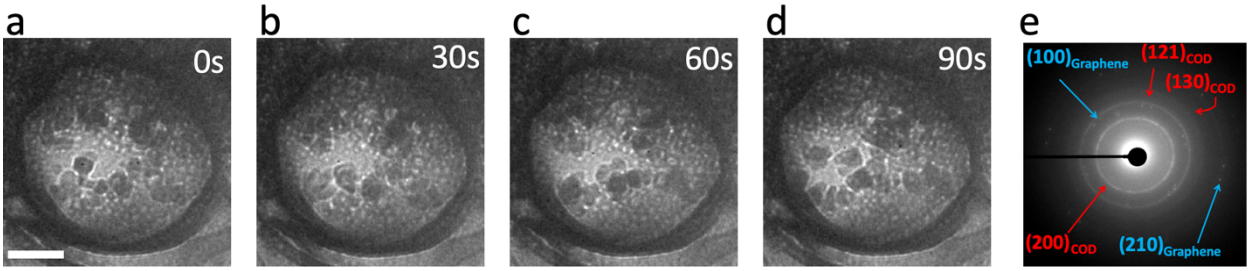

Figure D4. Unaltered version of the GLC TEM images in figure 4 **a-e**. In **(a)** through **(d)**, a time series shows motion of nanoparticles within GLC. In **(e)**, SAED shows the overlapped graphene and COD diffraction peaks as collected from a GLC sample. The scale bar in **(a)** is 100 nm.

D.2 Consideration of Electron Beam and Encapsulation Effects

As mentioned in section 1.7, CaOx formation is initiated by free radical production. The chemical species present may be modeled by equations 3 and 4 (page). Since the GLC is in equilibrium prior to imaging in TEM, the formation rate of the CaOx depends primarily on the production of CaOx (R_i) by the electron beam. As mentioned in section 1.7 the free radical concentration quickly reaches equilibrium during electron beam exposure[28]. Since the radiolysis species are in equilibrium within each experiment, differences in the electron beam radiation history do not alter the observed differences in the crystallization pathways shown in figures 4.2 through 4.5. The free radical concentrations generated by the electron beam were predicted to be 10^{-6}M to 10^{-3}M, depending on the free radical species, as predicted by Schneider *et al* [28].

CaOx samples were then imaged in separate GLCs at high electron dose rates and low extron dose rates. The electron dose rate was positively correlated with the growth rate of the CaOx particles but did not alter the formation pathway. In figure D5 **a-d**, the electron dose rate was $5.35*10^{10}$ Gy/s. Under this electron dose, it took 36 seconds to form the particle displayed in figure D5 **d**, with a total area of 16,090 nm^2. In figure D5 **e-h** the electron dose rate was instead $2.24*10^{12}$ Gy/s. Under this electron dose, it took only three seconds to form the particle displayed in D5**h**, with a total of 7,212 nm^2. The area of the particle in **d** reveals an average growth rate of approximately 446 nm^2/s under a low electron dose, while measurement of **h** reveals an average area growth rate of 2,404 nm^2/s under a high electron dose.

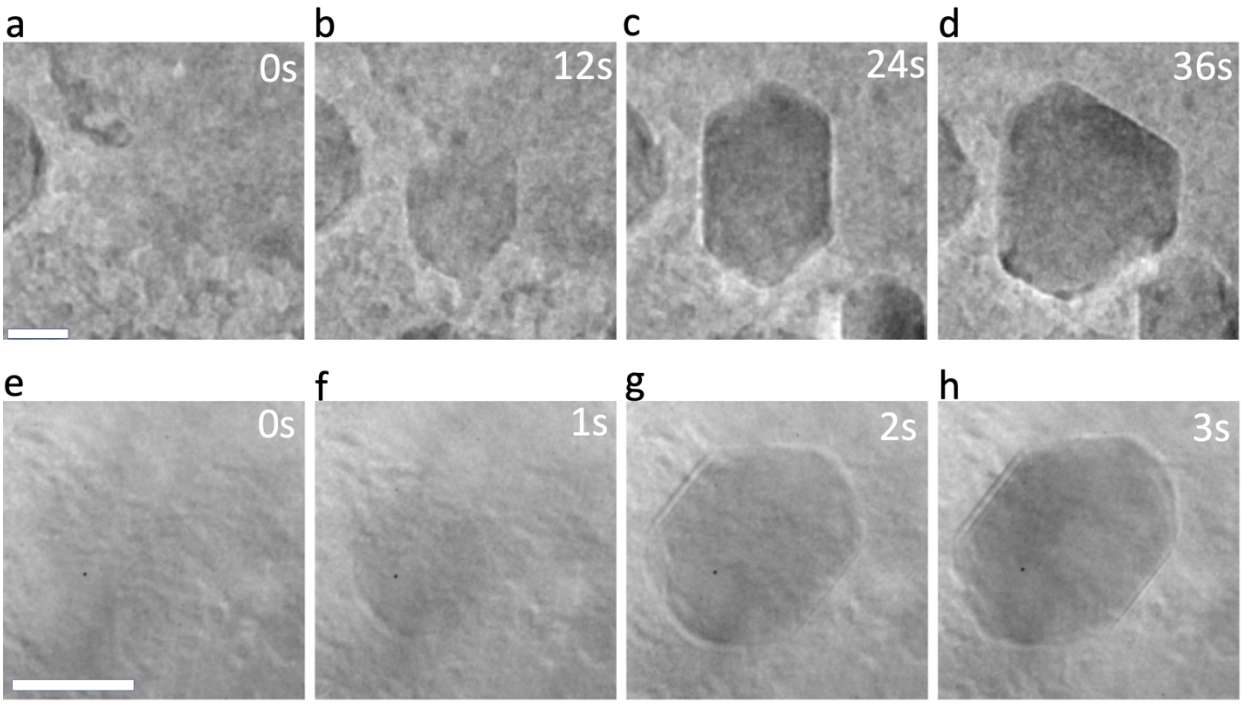

Figure D5. Classical formation of CaOx under a low electron dose rate (**a-d**) and under high electron dose rate (**e-h**). In **a-d**, it takes 36 seconds to form the particle shown in **d** under low electron dose, while under high electron dose the particle in h forms in only 3 seconds. The scale bars in **a** and **d** are both 100nm.

Additional factors such as the effect of the graphene surfaces on the crystallization of CaOx, the pressure within GLCs, and nanoscale confinement on the biomineralization process within GLCs should also be discussed. Graphene is a chemically inert material, which allows for chemical reactions to occur without the possible influence of chemically reactive surfaces [279]. Further, the picopure water used here allows analysis of the CaOx synthesis without the influence of chemical species other than the sodium and chloride byproducts, indicating the observed crystallization is not altered by the graphene or chemical agents. Additionally, the pressure within GLC increases due to Van der Waals forces, which adhere the graphene layers, and should be considered. Pressure

may in some circumstances induce crystallization, however, the pressure here is not sufficient to cause crystallization of CaOx since the CaOx only forms when exposed to the electron beam[280]. The Van der Waals forces dominate the pressure within the GLC[32]. As mentioned in section 1.7, the pressure is a function of equation 5:

Equation 5: $$P = \frac{4\pi\gamma}{5C_v h_{max}}$$

Where P is the pressure, γ the adhesion strength, C_v is a shape dependent constant, and h_{max} the maximum height[6]. The height may be estimated by equation 6:

Equation 6: h_{max}=0.11*R, where R is the radius[32].

Here, figures 3.1, 3.7, 4.2-4, and D1-D5 were collected from large GLCs with radii of approximately 700nm to 900nm. These values suggest pressures on the order of 10 atm to 15 atm[32]. MD simulations did not show any significant difference in the CaOx formation dynamics in the 1 atm simulations (fig. 4.4) as compared to simulations at 100 atm (fig. D6 and D7).

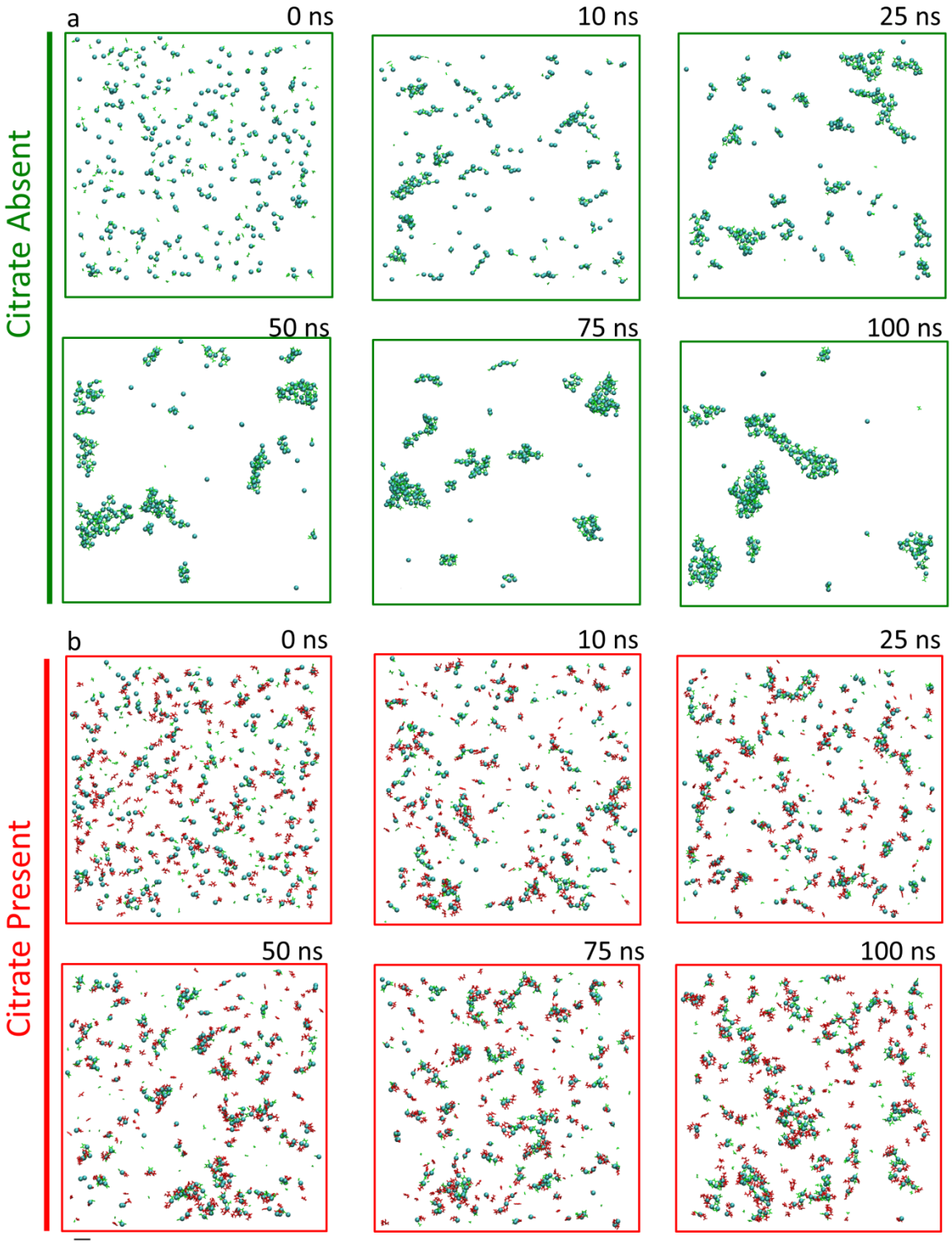

Figure D6. MD modelling of CaOx formation with and without citrate at 100 atm. In **(a)**, CaOx forms in the absence of citrate, showing aggregation of prenucleation ion clusters. In **(b)**, CaOx in

the presence of citrate forms metastable nucleation clusters. Pressure is not a factor for cluster formation.

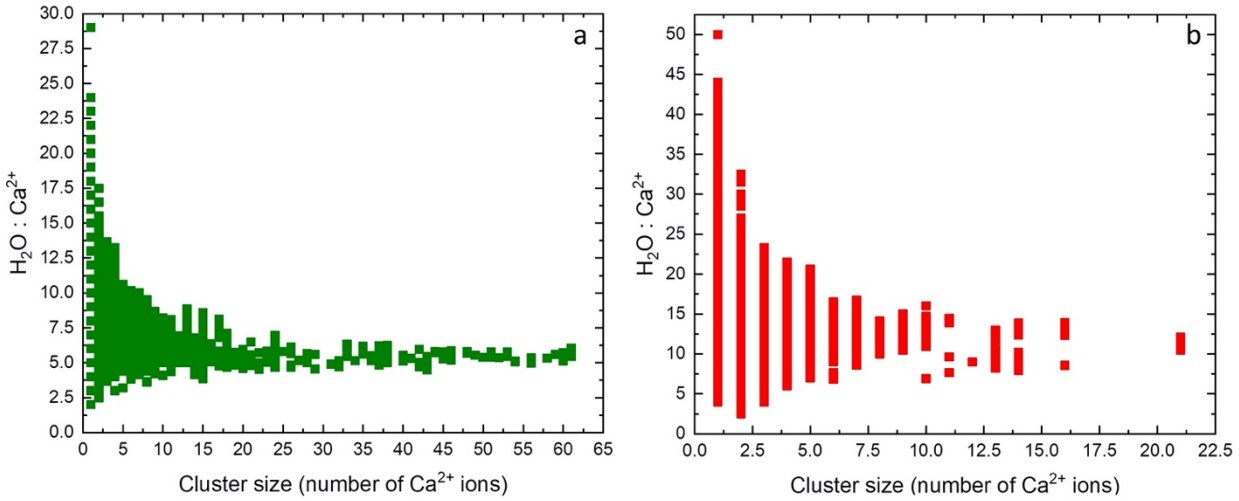

Figure D7. Correlation of ratio of water to cluster size (number of H2O molecules/ number of Ca2+ ions in a given cluster) versus size of cluster at 100 atm for **a)** system with citrate absent and **b)** system with citrate present. Once again, pressure is not a factor.

APPENDIX E: RIGHTS AND PERMISSIONS

Portions of chapter three have been reprinted with under a Creative Commons license with permission from Banner, D. Firlar, E. Jakobonis, J. Baggia, Y. Finlay, J. Shahbazian-Yassar, R. Megaridis, C. and Shokuhfar, T. Correlative ex situ and Liquid-Cell TEM Observation of Bacterial Cell Membrane Damage Induced by Rough Surface Topology. *Journal of International Medicine.* Originally published by Dove Medical Press Limited.

DOVE Medical Press

3rd April 2020

To Whom It May Concern

RE : ACI201266- PMN/Banner - Permission Letter

This permission letter confirms that permission is granted for use of some sections by Dove Medical Press Limited, as described in your request for your dissertation:

As a condition of permission being granted, we require that:

- The article is fully cited, as above
- Dove Medical Press Limited is clearly acknowledged as the original publisher.

Please note that this permission relates only to the use as described in your below email and any future use will require further permission to be granted.

For any further information please do not hesitate to contact me either at this office or by email *jan@dovepress.co.uk.*

Yours faithfully,

Jan Goodwin
Client Services Director
for Dove Medical Press Limited

Beechfield House, Winterton Way, Macclesfield SK11 0JL, Cheshire, United Kingdom
Tel: +44 (0) 1625 509131 Fax: +44 (0) 1625 617933
www.dovepress.com

Portions of chapter three have been reprinted with permission from Banner, DJ, Jakubonis, J. Firlar, E. Final, JK. Bogdanowicz, A. Shahbazian Yassar, R. Megaridis, C. Shokuhfar, T. (2018) In situ Encapsulation of E. coli in GLC and Prediction of Beam Induced Death. *Microscopy and Microanalysis*, 24 (S1). 312-313. Originally published by Cambridge University Press.

Issue	S1
Start page	312
End page	313
Type of Use	Dissertation/Thesis
Requestor type	Author
Portion	Full article
Author of this Cambridge University Press article	Yes
Author / editor of the new work	Yes
Title	TEM of Biologically Induced Reactions: Kidney Stone Mineralization and E. coli-Fiber Interactions
Institution name	University of Illinois at Chicago
Expected presentation date	Apr 2020
Territory for reuse	World
Requestor Location	Mr. David Banner 3208 Chatham Dr URBANA, IL 61802 United States

Attn: Mr. David Banner

Publisher Tax ID GB823847609

Total 0.00 USD

Terms and Conditions

TERMS & CONDITIONS

Cambridge University Press grants the Licensee permission on a non-exclusive non-transferable basis to reproduce, make available or otherwise use the Licensed content 'Content' in the named territory 'Territory' for the purpose listed 'the Use' on Page 1 of this Agreement subject to the following terms and conditions.

1. The License is limited to the permission granted and the Content detailed herein and does not extend to any other permission or content.
2. Cambridge gives no warranty or indemnity in respect of any third-party copyright material included in the Content, for which the Licensee should seek separate permission clearance.
3. The integrity of the Content must be ensured.
4. The License does extend to any edition published specifically for the use of handicapped or reading-impaired individuals.
5. The Licensee shall provide a prominent acknowledgement in the following format: author/s, title of article, name of journal, volume number, issue number, page references, , reproduced with permission.

Other terms and conditions:

v1.0

Questions? customercare@copyright.com or +1-855-239-3415 (toll free in the US) or +1-978-646-2777.

VITA

EDUCATION
PhD in Bioengineering, May 2020 (Expected)
University of Illinois at Chicago,
Chicago, IL, USA

B.A. in Psychology, May 2013
Southern Illinois University at Carbondale,
Carbondale, IL, USA

RESEARCH EXPERIENCE
University of Illinois at Chicago,
Graduate Research Assistant: Fall 2019-May 2020

Southern Illinois University at Carbondale
Undergraduate Laboratory Assistant: Fall 2011-Spring 2012

TEACHING EXPERIENCE
Teaching Assistant:

- BIOS 101: Biology of Populations and Communities, Spring 2014.
- BIOS 110: Biology of Cells and Organisms, Spring 2020.
- BIOS 223: Cellular Biology Laboratory, Fall 2014.
- BIOE 250: Clinical Problems in Bioengineering, Spring 2015, Spring 2016.
- BIOE 460: Biomaterials, Fall 2015, Fall 2019

SELECTED PUBLICATIONS

1. **David J. Banner**, Reza Shahbazian Yassar, Tolou Shokuhfar. Liquid Phase TEM of Biological Species and Relevant Materials. (In Preparation).
2. **David J. Banner**, Emre Firlar, Pavel Rehak, Tara Foroozon, Jodi K. Finlay, Surya Narayanan, Talia Tasheen, Yusuf Baggia, Peter Kral, Tolou Shokuhfar, Reza Shahbazian-Yassar. In Situ TEM of Classical and Nonclassical Multiphase Nucleation of Calcium Oxalate. (Submitted)
3. **David J. Banner**, Emre Firlar, Justas Jakobonis, Yusuf Baggia, Jodi Finlay, Reza Shahbazian-Yassar, Constantine Megaridis, and Tolou Shokuhfar. (2020). Correlative Ex Situ and Liquid-Cell TEM Observation of Bacterial Cell Membrane Damage Induced by Rough Surface Topology. *International Journal of Nanomedicine*. 15. 1929-1239.
4. Mi-li Qi, Zhennan Huang, Wentao Yao, Fei Long, Meng Cheng, Boao Song, **David Banner**, Reza Shahbazian-Yassar, Yu-peng Lu, Tolou Shokuhfar. (2018). In situ visualization of the superior nanomechanical flexibility of individual hydroxyapatite nanobelts. 20(8). 1031-1036.

SELECTED CONFERENCE PROCEEDINGS

1. **David J Banner**, Justas Jakubonis, Emre Firlar, Jodi K Finlay, Agata Bogdanowicz, Reza Shahbazian Yassar, Constantine Megaridis, Tolou Shokuhfar. (2018). *In situ* Encapsulation

of *E. coli* in GLC and Prediction of Beam Induced Death. *Microscopy and Microanalysis*. 24(S1) 312-313.

2. **David J Banner**, Emre Firlar, Kun He, Jodi Finlay, Reza Shahbazian Yassar, Tolou Shokuhfar. (2018). In Situ Investigation of Calcium Oxalate Mineralization. *Microscopy and Microanalysis*. 24(S1). 1320-1321.
3. **David J Banner**, Emre Firlar, Jodi K Finlay, Reza Shahbazian-Yassar, Tolou Shokuhfar (2017) Electron Microscopy and Spectroscopy of Citrate Induced Calcium Oxalate Crystal Structure and Hydration State Changes, and Implications for Kidney Stones. *Microscopy and Microanalysis.* 23 (S1) 1208-1209.
4. **David Banner**, Emre Firlar, Hasti Asayesh-Ardakani, Reza Shahbazian-Yassar, Tolou Shokuhfar (2016) Synthesis and Characterization of Paramagnetic Iron Nanoparticles with Minimal Gold Coating for Optimal Drug Delivery. *Microscopy and Microanalysis.* 22(S3) 1096-1097.

AWARD
Microscopy and Microanalysis Presidential Student Scholar, 2016